

JAERI-M
91-094

CONCEPTUAL DESIGN OF FUSION
EXPERIMENTAL REACTOR (FER/ITER)
—ION CYCLOTRON WAVE SYSTEM—

June 1991

Haruyuki KIMURA, Mikio SAIGUSA, Yasushi SAITOH^{*1}
Hiroyuki ARAI^{*2}, Takashi NAGASHIMA, Tsuneyuki FUJII
Tadao OHNO^{*1}, Keigo SANO^{*3}, Atsushi FUKUYAMA^{*4}
Mitsuru YAMAGIWA and Kiyotaka HAMAMATSU

JAERI-Mレポートは、日本原子力研究所が不定期に公刊している研究報告書です。

入手の問合わせは、日本原子力研究所技術情報部情報資料課（〒319-11茨城県那珂郡東海村）あて、お申しこしてください。なお、このほかに財団法人原子力弘済会資料センター（〒319-11茨城県那珂郡東海村日本原子力研究所内）で複写による実費頒布をおこなっております。

JAERI-M reports are issued irregularly.

Inquiries about availability of the reports should be addressed to Information Division, Department of Technical Information, Japan Atomic Energy Research Institute, Tokai-mura, Naka-gun, Ibaraki-ken 319-11, Japan.

© Japan Atomic Energy Research Institute, 1991

編集兼発行	日本原子力研究所
印刷	日立高速印刷株式会社

Conceptual Design of Fusion Experimental Reactor (FER/ITER)
- Ion Cyclotron Wave System -

Haruyuki KIMURA, Mikio SAIGUSA⁺¹, Yasushi SAITOH^{*1}
Hiroyuki ARAI^{*2}, Takashi NAGASHIMA⁺¹, Tsuneyuki FUJII⁺²
Tadao OHNO^{*1}, Keigo SANO^{*3}, Atsushi FUKUYAMA^{*4}
Mitsuru YAMAGIWA⁺³ and Kiyotaka HAMAMATSU⁺³

Fusion Experimental Reactor Team
Naka Fusion Research Establishment
Japan Atomic Energy Research Institute
Naka-machi, Naka-gun, Ibaraki-ken

(Received May 13, 1991)

Conceptual design of the Ion Cyclotron Wave (ICW) system for FER and Japanese contribution to the conceptual design of the ITER ICW system are presented. A frequency range of the FER ICW system is 50-85 MHz, which covers $2\omega_{cT}$ heating, current drive by TTMP and $2\omega_{cD}$ heating. Physics analyses show that the FER and the ITER ICW systems are suitable for the central ion heating and the burn control. The launching systems of the FER ICW system and the ITER high frequency ICW system are characterized by in-port plug and ridged-waveguide-fed 5x4 phased loop array. Merits of those systems are (1) a ceramic support is not necessary inside the cryostat and (2) remote maintenance of the front end part of the launcher

+1 Department of Fusion Engineering Research

+2 Department of Fusion Facility

+3 Department of Fusion Plasma Research

*1 Toshiba Corporation

*2 Yokohama National University

*3 NEC Corporation

*4 Okayama University

is relatively easy. Overall structure of the launching system is consistent with radiation shielding, cooling, pumping, tritium safety and remote maintenance. The launcher has injection capability of 20 MW in the frequency range of 50-85 MHz with the separatrix-antenna distance of 15cm and steep scrape-off density profile of H-mode. The shape of the ridged waveguide is optimized to provide desired frequency range and power handling capability with a finite element method. Matching between the current strap and the ridged waveguide is satisfactorily good. Thermal analysis of the Faraday shield shows that high electric conductivity low Z material such as beryllium should be chosen for a protection tile of the Faraday shield. Thick Faraday shield is necessary to tolerate electromagnetic force during disruptions. R&D needs for the ITER/FER ICW systems are identified and gain from JT-60/60U ICRF experiments and operations are indicated in connection with them.

Keywords: ICW System, FER, ITER, Second Harmonic Heating, Current Drive by TTMP, Burn Control, Launching System, Phased Loop Array, Ridged Waveguide, Faraday Shield, JT-60/60U ICRF Experiment

核融合実験炉 (FER / ITER) の概念設計

ーイオンサイクロトロン波システムー

日本原子力研究所那珂研究所核融合実験炉特別チーム

木村 晴行・三枝 幹雄⁺¹・斉藤 靖^{*1}
 新井 宏之^{*2}・永島 孝⁺¹・藤井 常幸⁺²
 大野 忠雄^{*1}・佐野 圭吾^{*3}・福山 淳^{*4}
 山極 満⁺³・浜松 清隆⁺³

(1991 年 5 月 13 日受理)

FER のためのイオンサイクロトロン波 (ICW) システムの概念設計と ITER の ICW システムの概念設計に対する日本の貢献についてまとめる。FER の ICW システムの周波数範囲は 50-85 MHz であり、これにより $2\omega_{CT}$ 加熱, TTMP による電流駆動及び $2\omega_{CD}$ 加熱が可能である。物理解析の結果, FER 及び ITER の ICW システムは中心イオン加熱及び燃焼制御に適していることが示される。FER の ICW システムと ITER の高周波数 ICW システムの結合系の特徴はポート内プラグイン方式リッジ導波管給電型 5×4 ループアレイを採用していることである。その長所は(1)セラミックス製の支持物がクライオスタットの内部に不要であること(2)ランチャー先端部の遠隔保守が比較的容易であること等である。結合系の全体構造は放射線シールド, 冷却, 真空排気, トリチウム安全性及び遠隔保守との整合が取れている。H モードの急峻なスクレープオフ密度分布を仮定して, セパトトリックスアンテナ間距離 15 cm に対して, ランチャーは周波数範囲 50-85 MHz に於いて 20 MW の電力入射性能を有する。リッジ導波管の形状は必要とする周波数特性と耐電力性能を満足するように有限要素法によって最適化されている。ループアンテナとリッジ導波管の整合性は申し分なく良い。ファラディシールドの熱解析によりその保護タイルの材料としてベリリウムのような導電性の良い低 Z 材が適しているこ

那珂研究所: 〒311-01 茨城県那珂郡那珂町大字向山 801-1

+ 1 核融合工学部

+ 2 核融合装置試験部

+ 3 炉心プラズマ研究部

* 1 東芝

* 2 横浜国立大学

* 3 日本電気

* 4 岡山大学

とが示される。ディスラプション時の電磁力に耐えるために厚いファラディシールドが必要となる。ITER/FERのICWシステムに対するR&D計画及びそれに関連してJT-60/60UのICRF実験・運転からの知見として期待されるものが示される。

Contents

1. Introduction	1
1.1 Concepts of FER and ITER	1
1.2 Heating and Current Drive Scenarios of FER and ITER	1
1.3 Ion Cyclotron Wave Systems for FER and ITER	3
2. Physics Basis	5
2.1 Heating and Current Drive Scenarios	5
2.2 Power Partition and Power Deposition Profile	5
2.3 Current Drive	7
2.4 Effects of Poloidal Phasing	8
3. System Design for FER	23
3.1 Outline of the FER Ion Cyclotron Wave System	23
3.1.1 Design Policy	23
3.1.2 Basic Specifications	24
3.2 Launching System	24
3.2.1 Overall Structure	24
3.2.2 Radiation Shielding	25
3.2.3 Cooling System	26
3.2.4 Vacuum Pumping System	27
3.2.5 Tritium Safety	27
3.2.6 Remote Maintenance	28
3.3 Transmission Line System	28
3.4 RF Power System	29
3.5 Total System Efficiency	30
4. Antenna Design and Analysis	43
4.1 Basic Structure	43
4.2 Antenna-plasma Coupling	44
4.2.1 Coupling Calculation	44
4.2.2 Coupling Properties	46
4.2.3 Power Injection Capability	47
4.3 Analysis of T-shaped Ridged Waveguide with Arms	48
4.3.1 Introductory Remarks	48
4.3.2 Cutoff Frequency	48
4.3.3 Waveguide Impedance	49
4.3.4 Electric Field Distribution	50
4.3.5 Transmission Loss	50

4.3.6 Concluding Remarks	51
4.4 Analysis of Faraday Shield	51
4.5 Analysis of Guard Limiter	51
4.6 Analysis of Electromagnetic Force during Disruption	52
5. Conclusions and R&D Needs	82
5.1 Conclusions	82
5.2 R&D Needs	83
5.2.1 R&D Programme	83
5.2.2 Gain from JT-60/60U ICRF Experiments and Operations	83
Acknowledgment	88
References	88

目 次

1. 序 論	1
1.1 FER及びITERの概念	1
1.2 FERとITERの加熱電流駆動のシナリオ	1
1.3 FERとITERのイオンサイクロトロン波システム	3
2. 物理の基礎	5
2.1 加熱電流駆動のシナリオ	5
2.2 パワーの配分及びパワー吸収分布	5
2.3 電流駆動	7
2.4 ポロイダル位相制御の効果	8
3. FERのためのシステム設計	23
3.1 イオンサイクロトロン波システムの概要	23
3.1.1 設計の考え方	23
3.1.2 基本仕様	24
3.2 結合系	24
3.2.1 全体構造	24
3.2.2 放射線シールド	25
3.2.3 冷却システム	26
3.2.4 真空排気システム	27
3.2.5 トリチウム安全性	27
3.2.6 遠隔保守	28
3.3 伝送系	28
3.4 高周波電力増幅系	29
3.5 システム総合効率	30
4. アンテナ設計と解析	43
4.1 基本構造	43
4.2 アンテナープラズマ結合	44
4.2.1 結合計算	44
4.2.2 結合特性	45
4.2.3 入射電力容量	47
4.3 アーム付きT型リッジ導波管の解析	48
4.3.1 はじめに	48
4.3.2 カットオフ周波数	48
4.3.3 導波管の特性インピーダンス	49
4.3.4 電界分布	50

4.3.5	伝送損失	50
4.3.6	結語	51
4.4	ファラディシールドの解析	51
4.5	ガードリミタの解析	51
4.6	ディスラプション時の電磁力解析	52
5.	結論と R & D の必要性	82
5.1	結論	82
5.2	R & D の必要性	83
5.2.1	R & D 計画	83
5.2.2	J T - 60 / 60 U I C R F 実験運転から得られるもの	83
謝 辞	88
参考文献	88

1. INTRODUCTION

1.1 Concepts of FER and ITER

JAERI has performed conceptual design of the fusion experimental reactor in both domestic programme and international cooperation programme in these three years. Fusion Experimental Reactor (FER)¹⁾ corresponds to the domestic programme. Basic objectives of FER are to explore a machine that solves reasonable minimum physics and technological issues necessary to proceed to a demonstration power reactor (DEMO) without any further intermediate steps. Achievements of Q (energy multiplication factor) ≈ 20 and steady state at least separately under well controlled condition are considered to be a reasonable minimum step to proceed to DEMO. International Thermonuclear Experimental Reactor (ITER)²⁾ corresponds to the international cooperation programme, where four parties (EURATOM, Japan, the Soviet Union and the United States) join under the auspices of IAEA. Major objectives of ITER are as follows: (1) to demonstrate controlled ignition and extended burn of D-T plasma, with steady state as an ultimate goal, (2) to demonstrate technologies essential to a reactor in an integrated system and (3) to perform integrated testing of the high-heat-flux and nuclear components required to utilize fusion power.

Major device and plasma parameters for FER and ITER are as follows:

	FER	ITER
Major radius (m)	4.7	6.0
Minor radius (m)	1.6	2.15
Elongation	2.0	2.0
Toroidal field (T)	5.25	4.85
Plasma current (MA)	15	22
Fusion power (GW)	0.6	1

1.2 Heating and Current Drive Scenarios of FER and ITER

Roles of heating and current drive system necessary for operations of FER/ITER are considered as follows:³⁾

- (1) Ionization, Preheating, and Current Initiation
- (2) Non-inductive Current Ramp-up Assist
- (3) Heating to Ignition
- (4) Steady-state Current Drive
- (5) Local Current Profile Control
- (6) Burn Control

As it is difficult to cover these functions by any single heating and current drive system, combination of plural systems is inevitable. Following four heating and current drive systems were thought as the candidate.

- (1) Neutral Beam (NB) System
- (2) Ion Cyclotron Wave (IC) System
- (3) Lower Hybrid Wave (LH) System
- (4) Electron Cyclotron Wave (EC) System

Selection was made from the database obtained before and during the conceptual design phase and the modelling calculations.

For FER, 50 MW, 0.5 - 1 MeV NB is selected as main current drive and heating system, since some database exists for the current drive^{4,6)} and a theoretical current drive efficiency shows the best value among all schemes. 30 MW, 5 GHz LH system is selected for current ramp-up assist and current drive in the outer region. A plenty of database on the current drive by LH waves have established in many tokamaks. A record value of the current drive figure of merit (γ) of $0.34 \times 10^{20} \text{ Am}^{-2} \text{ W}^{-1}$ was obtained on JT-60.⁷⁾ However, in the steady-state scenario of FER/ITER, a flow channel of the driven current will be limited in the outer region because of a high electron temperature (volume-averaged electron temperature $\langle T_e \rangle \sim 20 \text{ keV}$). Current profile control can be thus expected in combination with NB current drive in order to obtain stable plasmas at high- β and to avoid the sawtooth oscillation. In addition, Volt-sec saving by LHCD⁸⁾ in the current ramp-up phase is quite useful in order to get higher plasma current or longer pulse discharge in FER, whose magnetic flux of the ohmic coil is relatively small. Thus the combination of NB and LH with a total power of 80 MW is chosen for the heating and current drive system of FER.

In order to supplement a central heating capability, either 20 MW, 50-85 MHz IC system or 20 MW, 140 GHz EC system is added. With IC system, unique central ion heating can be expected. This capability is favourable for getting high Q and for burn control, even at high electron density, where penetration of NB tends to be difficult. With EC system, strong central heating based on the electron heating is possible. In addition, EC system is a powerful tool for the preionization and the current initiation. If IC system will be chosen for a central heating method, a short pulse ($\leq 1 \text{ sec}$), several MW EC system will be necessary for the preionization and the current initiation. Stabilization and control of the sawtooth oscillation can be expected with both IC and EC systems.

For ITER, following two options have been determined in the course of the Conceptual Design Activity (CDA).

Reference: 75 MW, 1.3 MeV NB System
 50 MW, 5 GHz LH System

20 MW, 120 GHz EC System

Alternate: 130 MW, 15-80 MHz IC System
 50 MW, 5 GHz LH System
 20 MW, 120 GHz EC System

A reason why the combination of NB and LH is adopted for the reference current drive and heating scenario is the same as in FER. EC system is included in the reference scenario. Role of EC system is partly different from the one of FER. Capability of local current profile control near $q=2$ surface for the purpose of avoidance of disruptions is included instead of the central heating as considered in FER. In the alternative scenario, IC system replaces NB system. A reason why IC system is not chosen as a reference system is its sparse database on the current drive and its lower theoretical current drive efficiency (about two thirds of NBCD efficiency). However, from considering merits of IC system (unrivaled central ion heating, unnecessary of a large scale engineering development and low cost), it is proposed that both NB and IC be part of the reference system. This point will be discussed in the coming Engineering Design Activity (EDA).

1.3 Ion Cyclotron Wave Systems for FER and ITER

As mentioned above, the role of the FER IC system is mainly central heating. Therefore, the FER IC system need not be optimized for the current drive. It means that a large number of current straps in the toroidal direction are not necessarily needed. One of the features of the FER IC system is a compact launching system, where a concept of a ridged waveguide-fed loop antenna array is introduced. On the other hand, the ITER IC reference system aims both the current drive and the heating. A large number of the current straps should be installed with an equal spacing in the toroidal direction. A concept of in-blanket antenna is employed for this reason. The concept of the FER IC antenna was also proposed for ITER as a back-up solution to the reference antenna system, since ceramic insulator needed in the vacuum coaxial transmission lines would be critical. Hereafter we call this as the high frequency ITER IC system. Conceptual design of the reference and high frequency ITER IC systems is reported in Ref. 9.

This report describes conceptual design of Ion Cyclotron Wave (IC) system for FER and Japanese contribution to ITER. Physics basis for the FER and high frequency ITER IC systems is presented in Sec. 2. Overall system description of the FER IC system is presented in Sec. 3, where basic specification, antenna concept, system layout, radiation shielding, tritium safety, remote maintenance, RF generator, power supply and total system efficiency are described. In Sec. 4, design and analysis of the antenna system, which are

common items both for FER and high frequency ITER IC systems, including antenna-plasma coupling, power handling capability, ridged waveguide, Faraday shield, antenna guard limiter and the electromagnetic force during disruption are presented. Conclusions, R&D programme and gain from the JT-60/60U ICRF experiments and operations are presented in Sec. 5.

2. PHYSICS BASIS

2.1 Heating and Current Drive Scenarios

A frequency range is chosen to be 50-85 MHz for the FER IC wave system. Following heating and current drive scenarios are possible with this frequency range. They are considered to be necessary and sufficient for the objectives of this system.

$2 \omega_{cT}, \omega_{cHe3};$	53 MHz	<ul style="list-style-type: none"> - Central heating - Burn control - Sawteeth stabilization - D-He³ burn
$> 2 \omega_{cT};$	60 MHz	<ul style="list-style-type: none"> - Current drive
$2 \omega_{cD}, \omega_{cH};$	80 MHz	<ul style="list-style-type: none"> - Central heating - Burn control - Sawteeth stabilization - Local current profile control in combination with NBCD - Heating of hydrogen plasma (He⁴ minority second harmonic heating)

2.2 Power Partition and Power Deposition Profile

Power partition among species and power deposition profiles are calculated for the second harmonic heating and are compared with those of the third harmonic heating by using a one-dimensional full-wave code and a two-dimensional bounce-averaged Fokker-Planck code. The former takes account of the antenna phasing and the slowing-down distribution of alpha particles.¹⁰⁾ The latter calculates power partition and power deposition profile assuming uniform electric field along the wave path and monochromatic wave number spectrum ($N_{||}=1$). These two codes are considered to be complementary each other. Global wave structure is calculated by the 1-D full-wave code assuming Maxwellian distribution of bulk ions. In turn, distortion of energy spectra of ions due to the ICRF heating and resulting collisional power transfer to bulk ions and electrons near the plasma center are evaluated with the 2-D Fokker-Planck code. Plasma parameters for ITER are

used in the present calculation. Profiles of the density and the temperature are assumed as follows.

$$n(r) = (n(0)-n(a))(1-r^2/a^2)^{1/2} + n(a)$$

$$T(r) = (T(0)-T(a))(1-r^2/a^2) + T(a)$$

where $n(0)=2.1 \times 10^{20} \text{ m}^{-3}$, $T(0)=16.7 \text{ keV}$ ($\langle n \rangle = 1.4 \times 10^{20} \text{ m}^{-3}$, $\langle T \rangle = 10 \text{ keV}$) for ignition and $n(0)=1.05 \times 10^{20} \text{ m}^{-3}$, $T(0)=33 \text{ keV}$ ($\langle n \rangle = 0.7 \times 10^{20} \text{ m}^{-3}$, $\langle T \rangle = 20 \text{ keV}$) for steady-state operation. Figure 2-1 shows power absorption ratio among species (electrons, deuterons, tritons and fusion alphas) against a parallel refractive index corresponding to a peak position of the antenna current spectrum, $N_{\parallel}(p)$, calculated from the 1-D full-wave code in the case of the deuteron second harmonic ($2 \omega_{cD}$) heating and the ignition parameters. A ratio of the power absorbed by alphas and deuterons in the central region to the total RF power is $\sim 70 \%$ with $N_{\parallel}(p)=1$. About 50 % is absorbed by alphas and 20 % by deuterons. We cannot get central ion heating with higher $N_{\parallel}(p)$, which results in strong electron heating in a middle part of the plasma cross-section. Power deposition profiles and distributions of the wave electric fields with $N_{\parallel}(p)=1$ are shown in Fig. 2-2. Central narrow power deposition to deuterons and alphas and strong single pass absorption are indicated in the figure.

From the 2-D Fokker-Planck code, we obtain different results on the power partitions between deuterons and alphas in the central region. We assume 20 MW of the total RF power. Figure 2-3 shows the power deposition profiles for deuterons and alphas. The power absorption by deuterons is found to be dominant ($\sim 80 \%$). The reason can be explained by a trapped particle effect. In the Fokker-Planck calculation, the wave electric field pattern is uniform in the x-direction and parabolic in the y-direction, $|E_+|^2 \propto (1-y^2/L_A^2)$ for $|y| < L_A$, where L_A is an effective antenna length. In this case, even for alpha particles, the wave absorption is determined mainly by trapped ions, whose turning points where parallel velocity is zero are located on the the cyclotron resonance layer. Profile broadening of wave deposition to alpha particles due to the large Doppler shift resonance velocity is not significant. The width of the deposition region is almost corresponding to L_A . Therefore, power absorption is dominated by deuterons of major concentration. Collisional power transfers are $\sim 86\%$ to ions and $\sim 14\%$ to electrons. Thus the bulk ion heating is dominant in the central region with $2 \omega_{cD}$ heating for ignition parameters. The collisional power transfer with $2 \omega_{cT}$ heating is almost the same as the one with $2 \omega_{cD}$ heating. Power deposition profiles for the $2 \omega_{cT}$ heating is shown in Fig. 2-4. Thus, the central ion heating is expected both with $2 \omega_{cD}$ and $2 \omega_{cT}$ heatings. The central power density is comparable to that of the alpha heating. Thereby efficient burn control can be expected.

For steady-state parameters ($\langle T \rangle = 20$ keV, $\langle n \rangle = 0.7 \times 10^{20} \text{ m}^{-3}$), the collisional power transfers are 44% to ions and 56% to electrons with $2 \omega_{cD}$ heating. The collisional power transfer to electrons is dominated in this case.

Finally, we compare the third harmonic ($3\omega_{cD}$) heating with the second harmonic heating. Figure 2-5 shows the power absorption ratio as a function of $N_{||}(p)$. Profiles of power deposition and the wave electric field are indicated in Fig. 2-6. About 30 % of the power goes into tritons, since fifth harmonic resonance layer of tritons is located at about one-third of the minor radius in the low field side. Percentage of the power which can be absorbed by deuterons and alphas in the central region is ~55 % with $N_{||}(p)=1$. Power partition between deuterons and alphas in the central region is almost the same as for the second harmonic heating (i.e. ~80 % to deuterons and ~20 % to alphas). Power deposition profiles on deuterons and alphas are shown in Fig. 2-7. Percentages of collisional power transfers are ~72 % to ions and ~28 % to electrons for ignition parameters, and ~34 % to ions and ~66 % to electrons for steady-state parameters.

Power partition among species and central deposition power densities are summarized in Table 2-1 (ignition parameters) and Table 2-2 (steady-state parameters).

2.3 Current Drive

The current drive efficiency as well as the driven current profile is calculated by using the 1-D full-wave code. \tilde{j}/\tilde{p} formula including trapped particle effects, proposed by Ehst,¹¹⁾ is incorporated in the code. As mentioned above, a frequency around 60 MHz is the most suitable for the current drive in the frequency range chosen for FER. Percentage of the power absorbed by electrons is 70 ~ 80 % with $N_{||} = 2 \sim 3$. The rest of the power is absorbed mainly by tritons via the second harmonic resonance. The current drive figure of merit γ is $(0.25 \sim 0.18) \times 10^{20} \text{ Am}^{-2} \text{ W}^{-1}$ with $N_{||} = 2 \sim 3$. However, γ is reduced further (~70 %) if the antenna spectra of the four current straps are taken into account. Profiles of the driven current are centrally peaked because of decreasing the current drive efficiency in the outer region due to the trapped particle effects.

Local current profile control is possible by accelerating deuterium beam ions with second or third harmonic ICRF waves in NBCD plasma. The cyclotron resonance layer is located slightly in the high field side in order to enhance absorption by passing particles and to increase the driven current by ICRF waves. Enhancement of the current density by ICRF waves is localized near the cyclotron resonance layer. The current drive figure of merit of ICRF is about 0.13, although optimization in calculation has not yet been done so much. This application will be useful to provide a method of local current profile control with ICRF waves and to compensate the current profile of NBCD when the penetration problem of the neutral beam occurs.

2.4 Effects of Poloidal Phasing

The IC antenna system for FER has a large number of current straps in the poloidal direction. Therefore, effects of the poloidal phasing on the wave propagation and damping have been studied by using a two-dimensional full-wave code.¹²⁾ We could not calculate with actual plasma and machine parameters of FER because of a memory limit of the computer. We use following parameters in calculation in order to reduce radial wavelength of the fast wave; $B_T=7.3$ T, $f=110$ MHz (second harmonic resonance frequency of deuterons), $n_{e0}=0.15 \times 10^{20} \text{ m}^{-3}$ and $T_0 = 100$ keV. However, essential characteristics of the poloidal phasing can be well understood with above procedure. We also assume eight-row antenna array in the poloidal direction because of higher frequency. Figures 2-8 (a) ~ (d) show examples of the calculation. Remarkable effects of the poloidal phasing are seen in the wave propagation. The reason is that the wave propagation is not symmetrical with respect to k_y (poloidal wave number). Total and individual absorbed powers are indicated as a function of the poloidal phase difference between adjacent current straps in Fig. 2-9. Optimum phase difference for good coupling is found to be about -45 degrees. The worst case is about +90 degrees. The antenna loading resistance of each current strap is shown in Fig. 2-10. It is found that the antenna radiation with optimum phasing is converged much better than with the worst phasing and even with zero phasing case. This fact is also confirmed from the plots of the poynting vectors and the power deposition profiles in Fig. 2-8. The power deposition profiles change significantly according to the change of the poloidal phase difference.

Thus, the power deposition profile can be controlled with poloidal phasing. However, the power partition between the electrons and alpha particles cannot be changed by changing the poloidal phase.

Table 2-1 Power partition among species and central power densities for ignition parameters

1D Full-Wave Calculation ($N_{\parallel}/p=1.0$)

	$P_{H\parallel}^{\alpha}/P_{H\parallel}^{\text{tot}}$	$P_{H\parallel}^D/P_{H\parallel}^{\text{tot}}$	$P_{H\parallel}^T/P_{H\parallel}^{\text{tot}}$	$P_{H\parallel}^e/P_{H\parallel}^{\text{tot}}$
2 ω_{cD}	0.50	0.21	0.01	0.27
3 ω_{cD}	0.26	0.30	0.28	0.10

2D Fokker-Planck Calculation ($N_{\parallel}=1.0$)

	$P_{H\parallel}^{\alpha}/P_{H\parallel}^{\text{tot}}$	$P_{H\parallel}^D/P_{H\parallel}^{\text{tot}}$	$p_H^e(0)$ (MW/m ³)	$p_H^i(0)$	$p_H^{\text{tot}}(0)$	$p_{\alpha}^e(0)$	$p_{\alpha}^i(0)$	$p_{\alpha}^{\text{tot}}(0)$
2 ω_{cD}	0.17	0.83	0.19	1.16	1.35			
3 ω_{cD}	0.18	0.82	0.46	1.16	1.63			
2 ω_{cT}			0.25	1.35	1.6			
Alpha						1.20	0.42	1.63

Table 2-2 Power partition among species and central power densities for steady-state parameters

1D Full-Wave Calculation ($N_{\parallel}/p=1.0$)

	$P_{H\parallel}^{\alpha}/P_{H\parallel}^{\text{tot}}$	$P_{H\parallel}^D/P_{H\parallel}^{\text{tot}}$	$P_{H\parallel}^T/P_{H\parallel}^{\text{tot}}$	$P_{H\parallel}^e/P_{H\parallel}^{\text{tot}}$
2 ω_{cD}	0.70	0.12	0.01	0.19
3 ω_{cD}	0.53	0.11	0.21	0.15

2D Fokker-Planck Calculation ($N_{\parallel}=1.0$)

	$P_{H\parallel}^{\alpha}/P_{H\parallel}^{\text{tot}}$	$P_{H\parallel}^D/P_{H\parallel}^{\text{tot}}$	$p_H^e(0)$ (MW/m ³)	$p_H^i(0)$	$p_H^{\text{tot}}(0)$	$p_{\alpha}^e(0)$	$p_{\alpha}^i(0)$	$p_{\alpha}^{\text{tot}}(0)$
2 ω_{cD}	0.23	0.77	0.77	0.61	1.40			
3 ω_{cD}	0.22	0.78	0.95	0.50	1.47			
Alpha						0.54	0.37	0.91
NB						1.02	0.86	1.89

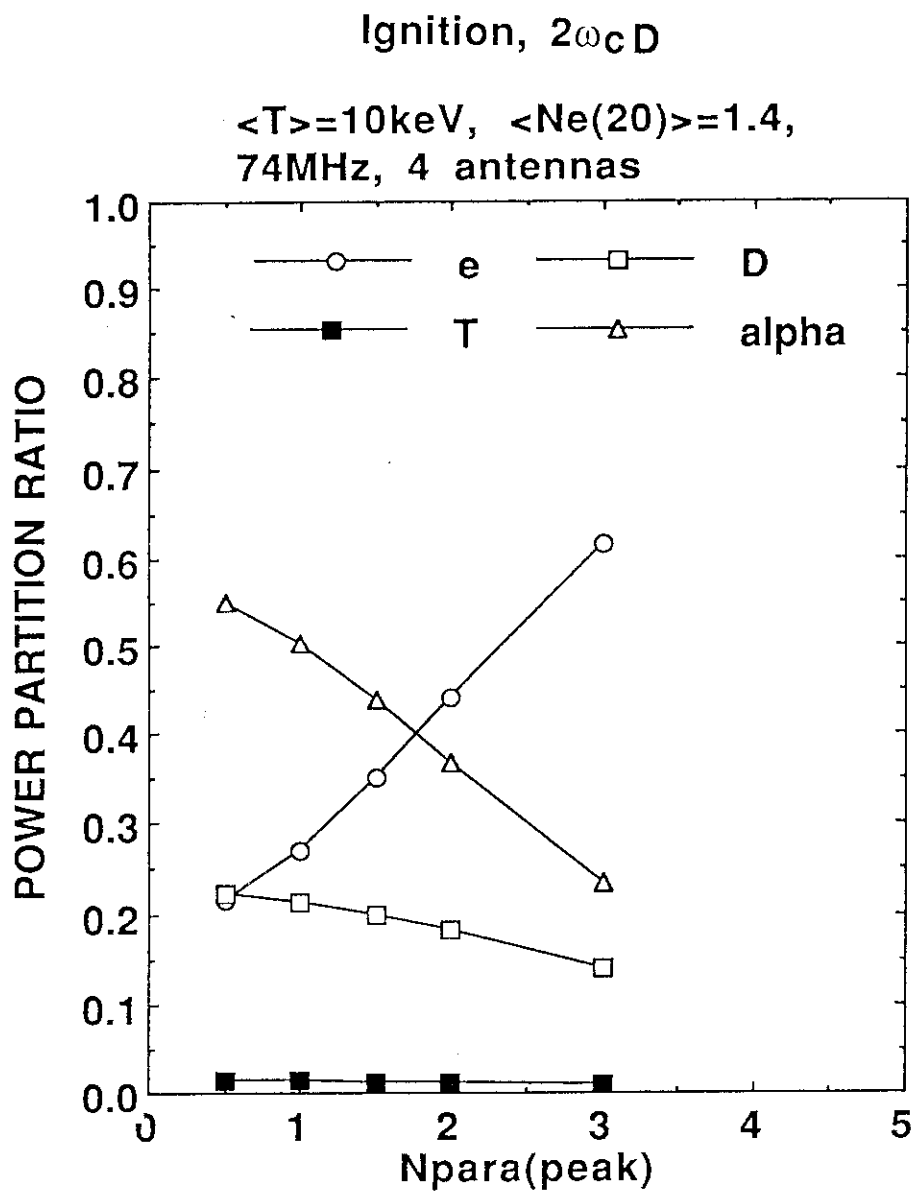


Fig. 2-1 Power partition ratio among species as a function of $N_l(p)$ in the case of the $2\omega_{cD}$ heating and the ignition parameters from the 1-D full-wave code.

Ignition, $2\omega_{cD}$, $N_{\parallel}(p)=1.0$

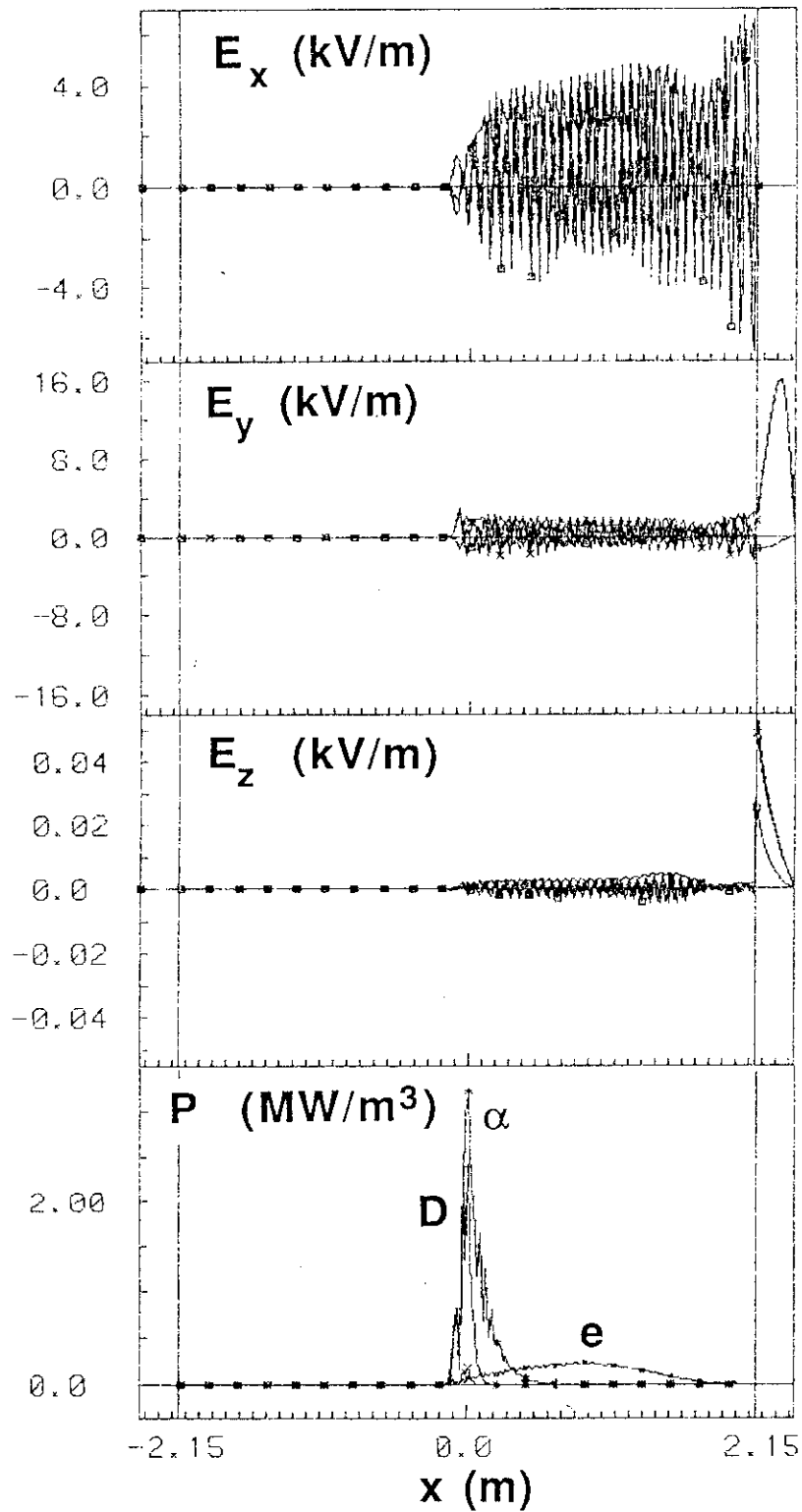


Fig. 2-2 Power deposition profiles and distributions of the wave electric fields in the case of the $2\omega_{cD}$ heating with $N_{\parallel}(p)=1$ and the ignition parameters from the 1-D full-wave code.

Ignition, $2\omega_{cD}$, $N_{||}=1.0$ **Deuteron**

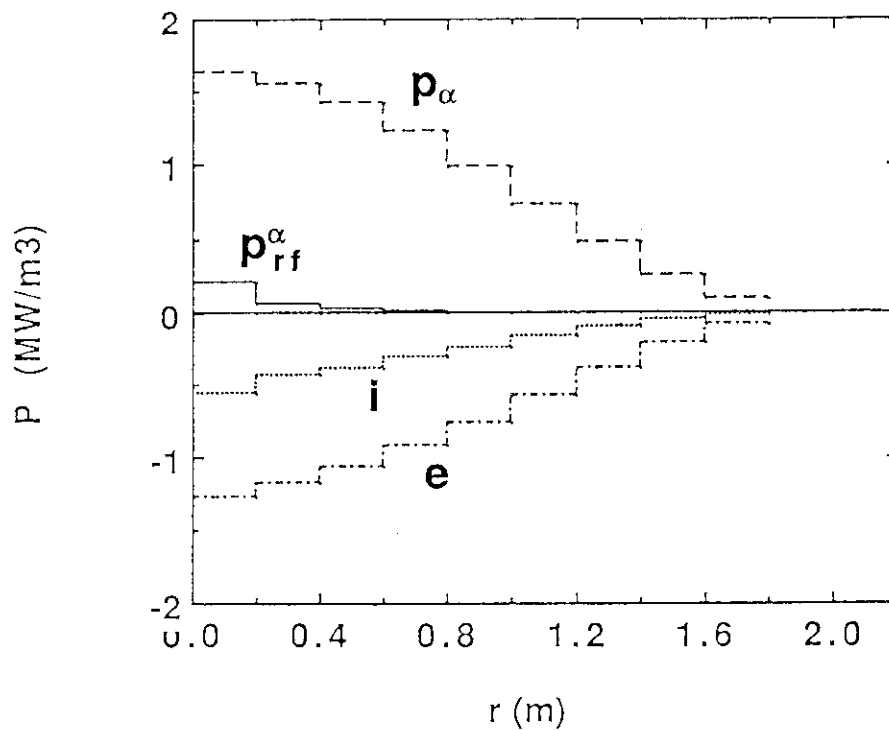
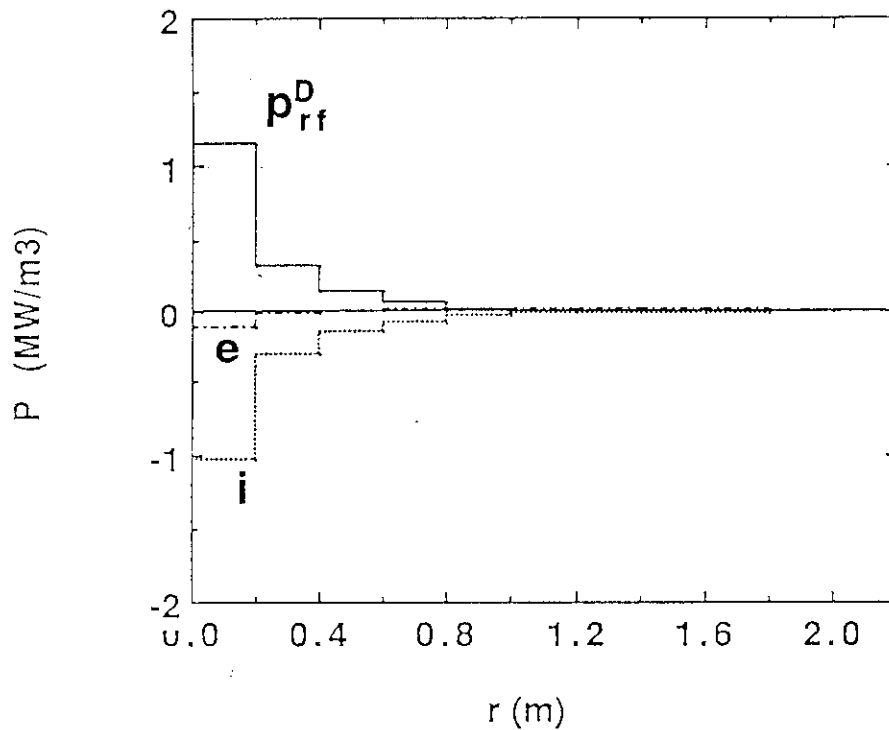


Fig. 2-3 Power deposition profiles for deuterons and alphas in the case of the $2\omega_{cD}$ heating with $N_{||}=1$ and the ignition parameters from the 2-D Fokker-Planck code. Fusion alpha heating power profile and collisional power transfer to electrons and ions (minus sign) are also indicated.

Ignition, $2\omega_{cT}$, $N_{||}=1.0$

Triton

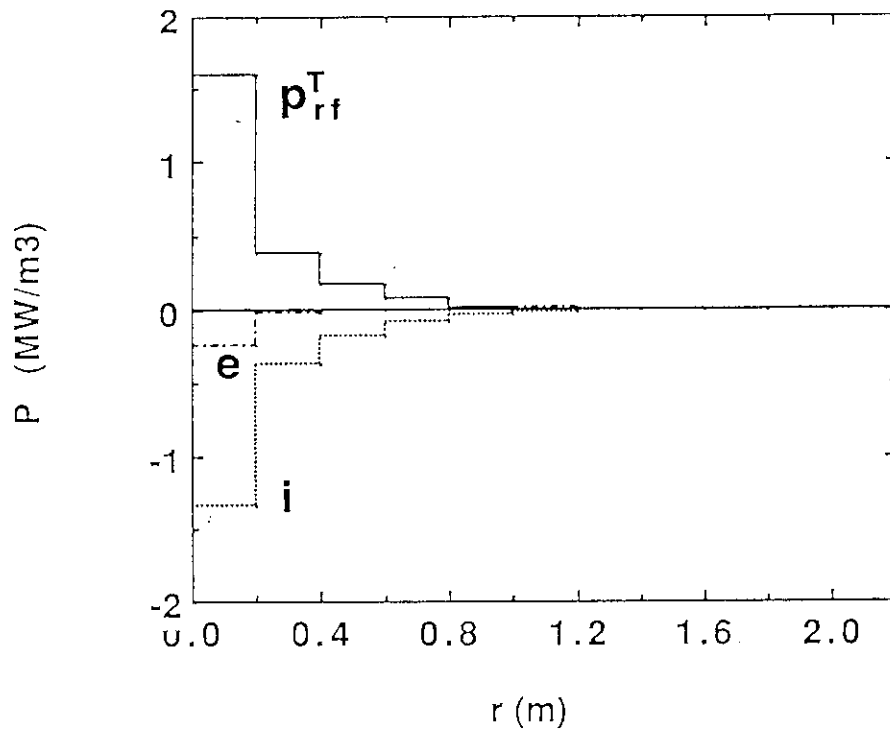


Fig. 2-4 Power deposition profiles for tritons in the case of the $2\omega_{cT}$ heating with $N_{||}=1$ and the ignition parameters from the 2-D Fokker-Planck code.

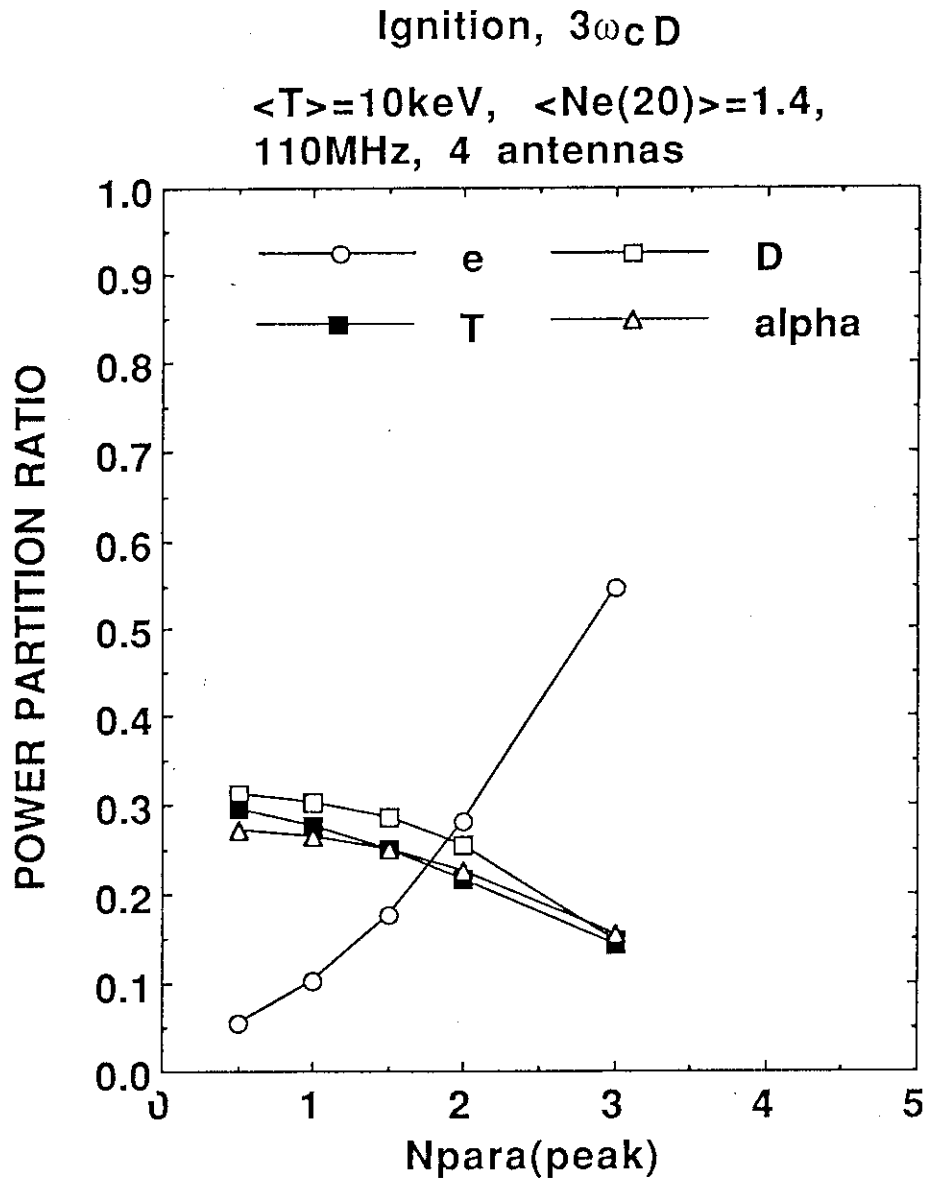


Fig. 2-5 Power partition ratio among species as a function of $N_{\text{I}}(p)$ in the case of the $3\omega_{cD}$ heating and the ignition parameters from the 1-D full-wave code.

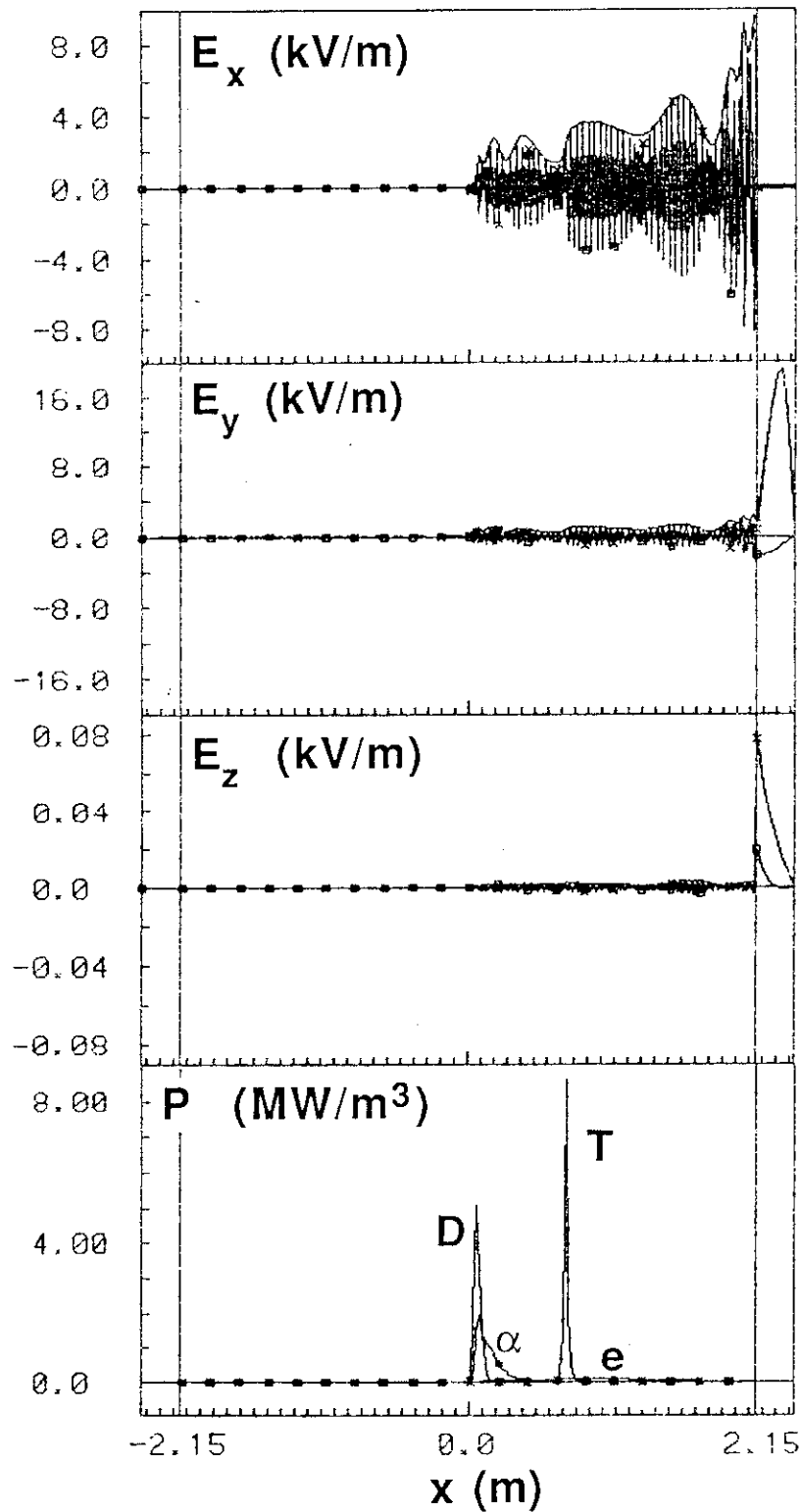
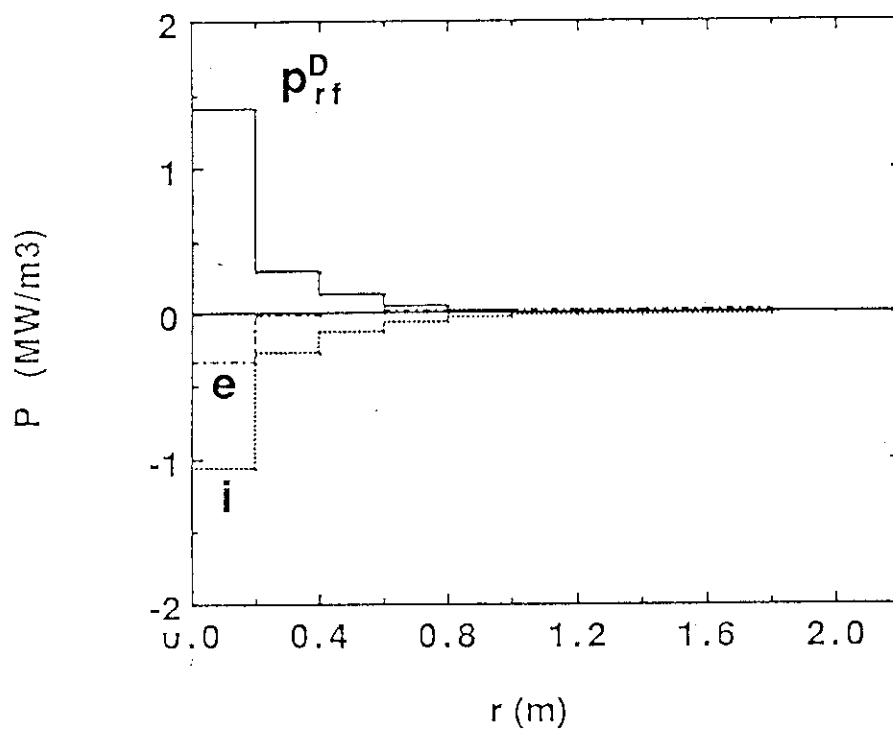
Ignition, $3\omega_{cD}$, $N_{\parallel}(p)=1.0$ 

Fig. 2-6 Power deposition profiles and distributions of the wave electric fields in the case of the $3\omega_{cD}$ heating with $N_{\parallel}(p)=1$ and the ignition parameters from the 1-D full-wave code.

Ignition, $3\omega_{cD}$, $N_{||}=1.0$ Deuteron



Alpha

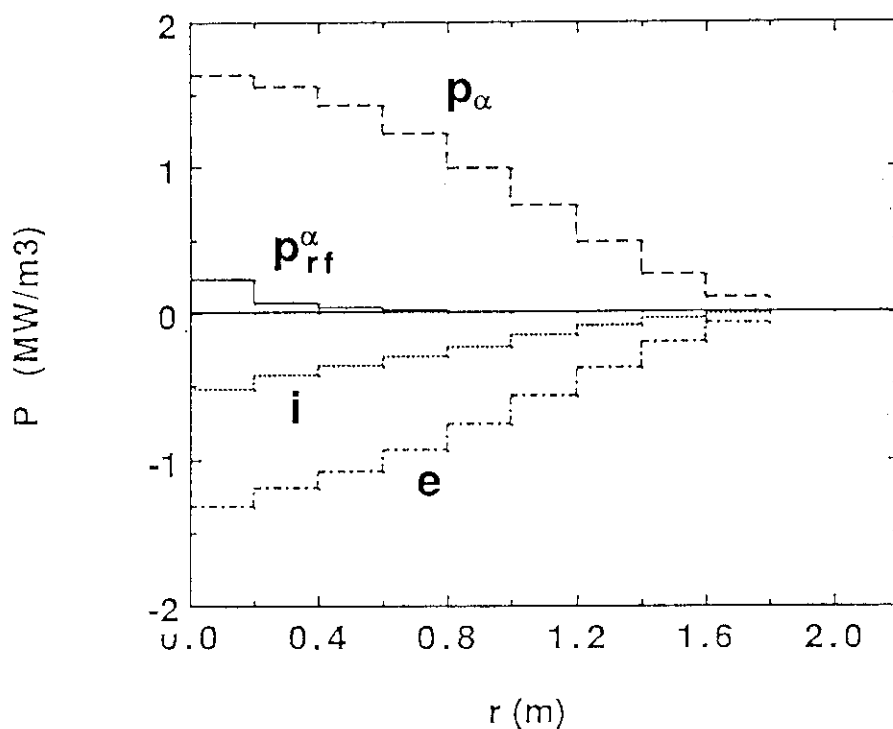


Fig. 2-7 Power deposition profiles for deuterons and alphas in the case of the $3\omega_{cD}$ heating with $N_{||}(p)=1$ and the ignition parameters from the 2-D Fokker-Planck code. Fusion alpha heating power profile and collisional power transfer to electrons and ions (minus sign) are also indicated.

(a) Poloidal phase difference = -135°

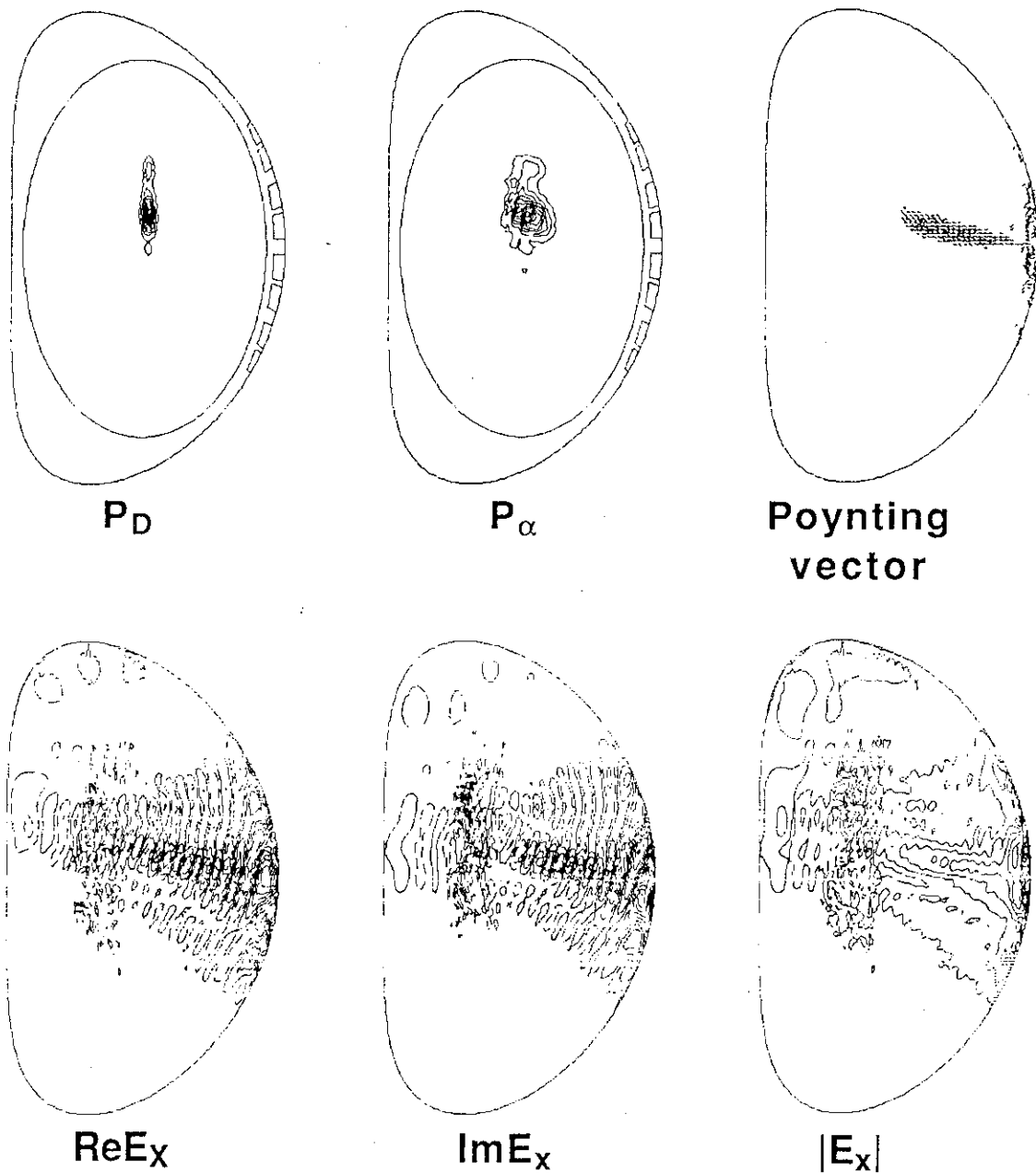


Fig. 2-8 Power deposition profile, Poynting vector and wave form on a poloidal cross-section for various poloidal phase differences with $N_{||}=1$ from the 2-D full-wave code. Contour lines are shown for P_D , P_α , $\text{Re}E_x$, $\text{Im}E_x$, and $|E_x|$. Solid lines for positive value and dashed lines for negative values.

(b) Poloidal phase difference = -45°

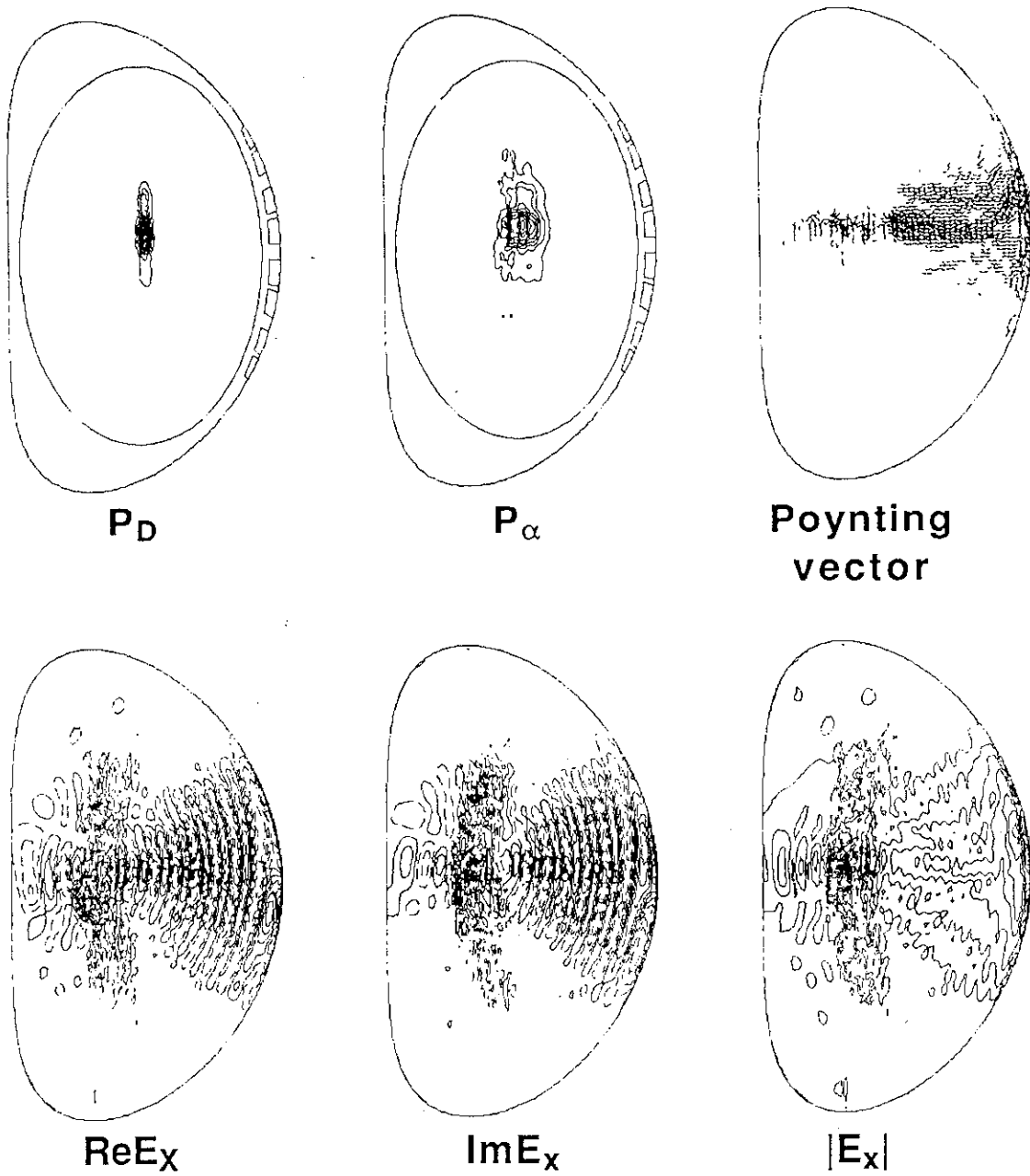


Fig. 2-8 (Continued)

(c) Poloidal phase difference = 0°

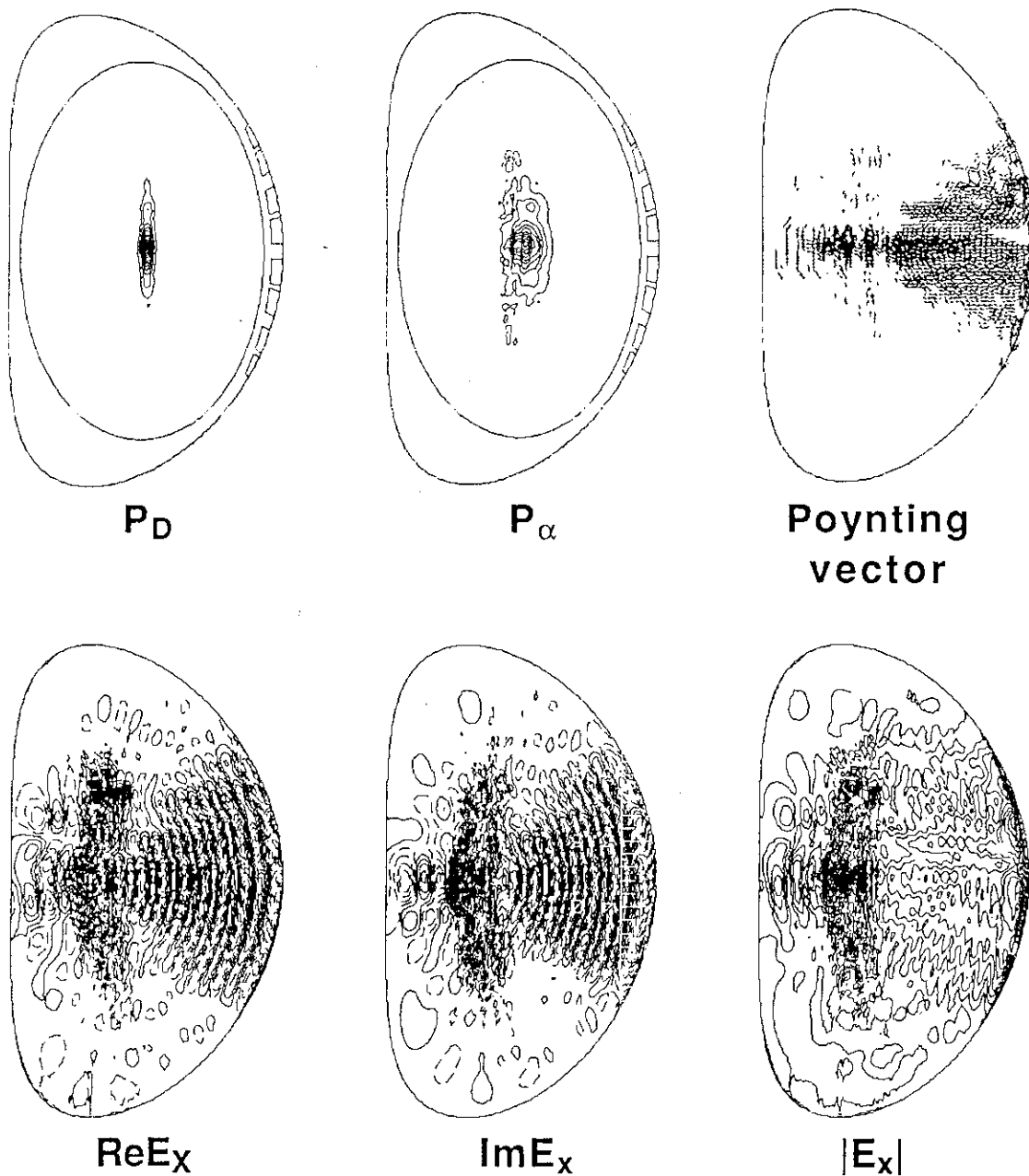


Fig. 2-8 (Continued)

(d) Poloidal phase difference = 90°

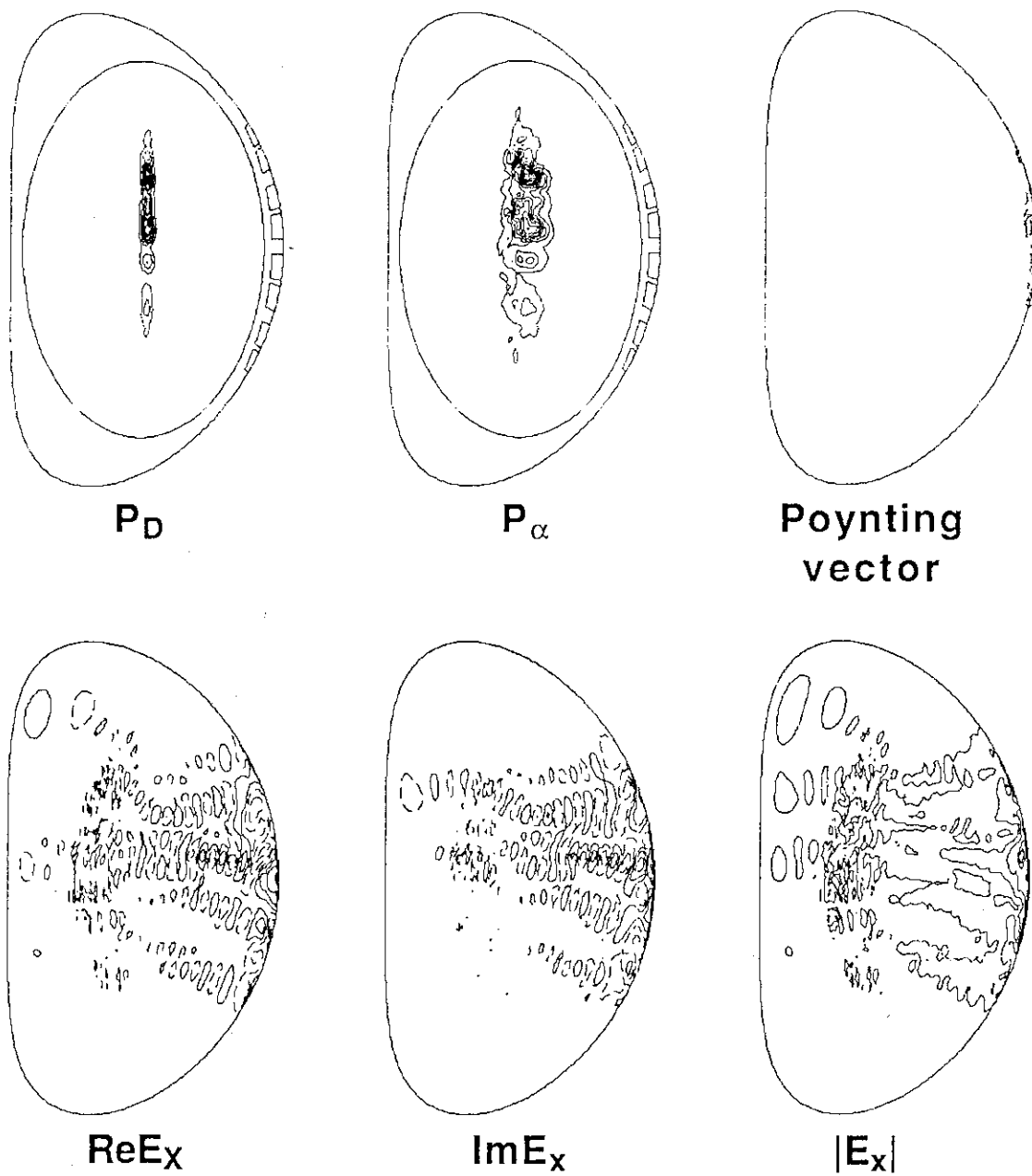


Fig. 2-8 (Continued)

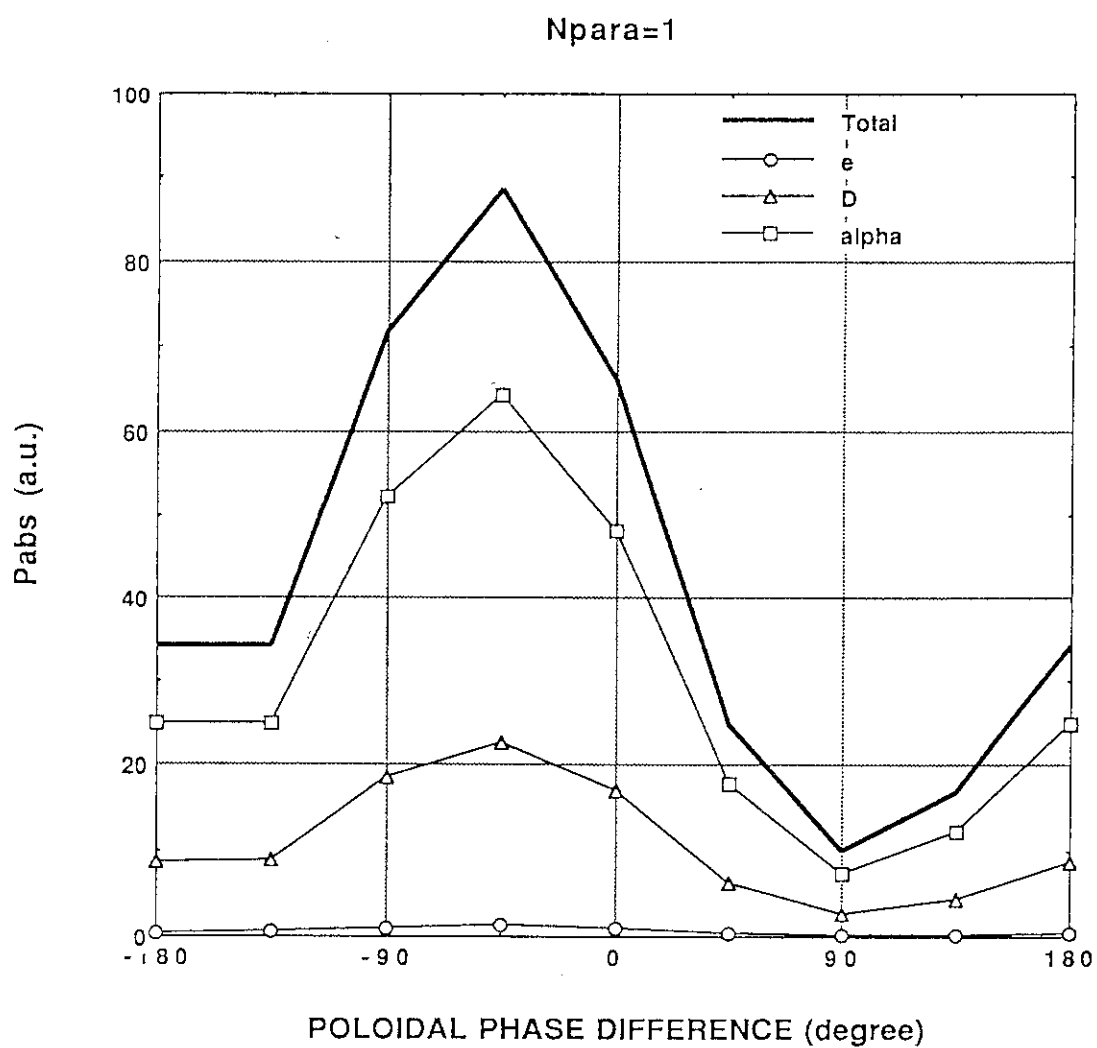


Fig. 2-9 Total and individual absorbed powers as a function of the poloidal phase difference from the 2-D full-wave code.

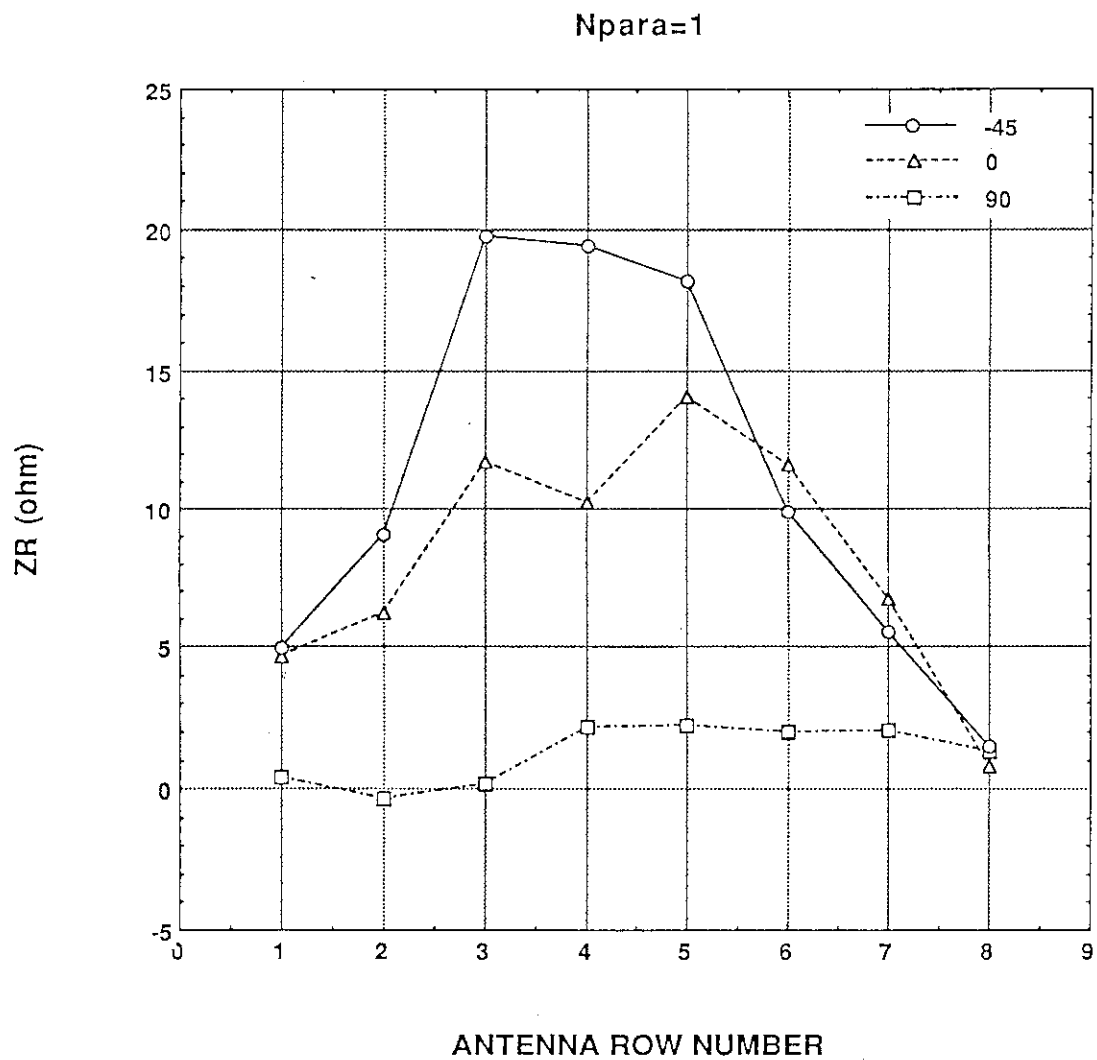


Fig. 2-10 Antenna loading resistance of each current strap for various poloidal phase differences from the 2-D full-wave code.

3. SYSTEM DESIGN FOR FER

3.1 Outline of the FER Ion Cyclotron Wave System

3.1.1 Design policy

The objectives of the IC system for FER are mainly central heating and burn control, and supplementarily current profile control. Therefore, the system can be designed to be compact in comparison with an IC system oriented for the current driver (e.g. ITER IC system⁹⁾). Design policy of the FER IC system is as follows.

1. Antenna phasing is possible both in toroidal and poloidal directions for optimization of the heating and the coupling and capability of the current drive.
2. The antenna spectrum should be satisfactory with a single horizontal port. This point is important for a compact launching system.
3. A concept of waveguide (e.g., ridged waveguide) is utilized in the vacuum transmission line. A ceramic support, which is a critical part in the reactor environment, can be avoided inside the cryostat.
4. An overall structure of the launcher is plug-in module, which is suitable for remote maintenance.
5. A frequency should be in a range where high power tetrode (≥ 2 MW/tube) is available.
6. Ion heating in the plasma core can be expected for efficient burn control of high density plasmas. This is possible by using second harmonic resonance heating of fuel ions with low $N_{||}$.
7. Supplemental current profile control is possible by accelerating electrons via transit time magnetic pumping (TTMP) or deuterium beam ions via second harmonic resonance with the neutral beam current drive.
8. Heating of a hydrogen plasma should be also possible at a frequency of 80 MHz (second harmonic minority helium 4 heating).

Figure 3-1 shows a concept of the antenna proposed for the FER IC system. Features of the antenna are (1) compact in-port design and (2) waveguide-fed loop antenna array.¹³⁾ A radiation part of the antenna consists of conventional and reliable multiple-loop array, but a ridged waveguide is utilized as a vacuum transmission line instead of a coaxial line. Thereby the antenna is free from a ceramic support inside the cryostat. By optimizing a shape of the ridge (Sec. 4.3), a cutoff frequency of the ridged waveguide can be reduced

down to 43 MHz. Frequencies near the tritium second harmonic resonance frequency, which are important both for heating and current drive, are included in the frequency range.

3.1.2 Basic specifications

Basic specifications of the FER IC system are determined to satisfy above requirements:

Injection power	20MW
Frequency	50 MHz ~ 85 MHz
No. of port	1
Size of port	1.2 m (width) \times 3 m (height)
Launcher	
Type	Phased loop array
No. of current strap	4 (toroidal direction) 5 (poloidal direction)
$N_{ }$	0 ~ 12
Power density	6.4 MW/m ²
Transmission line	
Vacuum side	Ridged waveguide
Pressurized side	Coaxial line
No. of lines	20
Power source	
Tube	Tetrode
Output power	2 MW/tube
No. of amplifier channel	20

3.2 Launching System

3.2.1 Overall structure

A basic concept of the total launching system is presented here. Detailed description of a front part of the launcher is given in Sec. 4.1. Figures 3-2 and 3-3 show respectively elevation and horizontal views of an overall structure of the total launching system. The launcher plug is installed in the horizontal port of FER. The design is based on the concept where the port is supported on the cryostat. The launcher plug is supported by the port and

partly from a supporting structure outside the cryostat. Large double bellows and driving mechanism are used for moving the launcher plug radially. A detailed study will be necessary for supporting and driving the launcher plug.

A detailed structure of the launcher plug is shown in Fig. 3-4 (elevation view) and Fig. 3-5 (horizontal view). Ridged waveguides are connected by coaxial transmission lines inside the launcher plug. Optimum connection between the ridged waveguide and the coaxial line should be studied further. The coaxial lines are bent at an angle of 90° inside the launcher plug and come out from it. Primary and secondary feedthroughs are placed in the coaxial line outside the cryostat. Ceramic supports are necessary between the junction of waveguide and coax and the primary feedthrough, since a distance between them are long. They will be placed at the point where the neutron fluence is less than 10^{18} n/cm^2 .

A rear part of the launcher after the double bellow is enveloped by a container with a double door. Inside of the container is filled with water for shielding in operation. Coaxial transmission lines are also contained in boxes for double containment of tritium and radiation shielding. The boxes are separated in parts with primary and secondary feedthroughs.

A matching network consists of one line stretcher and one stub tuner per one antenna channel. This combination is suitable for a wide band system.

3.2.2 Radiation shielding

Personal access should be secured outside the reactor room during operation and inside the reactor room one week after shut-down. A limit dose for personal access is 2.5 mrem/h. A dose rate at the first wall is 4×10^{13} mrem/h during operation and 8×10^9 mrem/h one week after shut-down. Dose rates at various positions without shielding, which are estimated from results of a 2-D Monte Carlo calculation for the NBI beam line,¹⁴⁾ are given below.

	First wall (mrem/h)	Outside wall of cryostat (mrem/h)	Outside wall of reactor room (mrem/h)
During operation	4×10^{13}	5×10^{11}	1.3×10^{10}
One week after shut-down	8×10^9	1×10^8	3×10^6

We evaluate radiation shielding needed for the present system to satisfy above criterion. We assume that a dose rate is reduced by one order of magnitude for each bend and absorbing materials around the coaxial lines. Reduction of the dose rate from the first wall

at various positions is indicated in Fig. 3-6. Then the dose rate at the outside wall of the reactor room is 8.3 mrem/h during operation. Only small additional shield is necessary to reduce to 2.5 mrem/h level outside the reactor room. On the other hand, in the reactor room, thick additional shield is necessary for personal access according to the distance from the first wall. If the shield is composed of 20 % S.S. and 80 % H₂O, thickness of 135 cm and 35 cm is necessary around the primary feedthrough and the secondary feedthrough, respectively. At the rear part of the launcher plug, the container filled with water, whose radial thickness is about 2 m, is sufficient for the shielding.

3.2.3 Cooling system

The launcher has two water cooling piping systems. One is for the Faraday shield and the guard limiter, and the other is for the ridged waveguides including the current straps. They are shown in Figs. 3-4 and 3-5.

(1) Faraday shield and guard limiter

Heat load on the Faraday shield and the guard limiter are summarized in Table 3-1. We assume that the alpha particle loss¹⁵⁾ (q_α) to the Faraday shield is negligibly small, because the Faraday shield is recessed by 15 mm from the top surface of the guard limiter. In turn, q_α to the inside surface of the guard limiter is enhanced by a factor of $l_{FS}/(2 \times l_{recess}) + 1$ from the value to a uniform wall surface near the equatorial plane (7 W/cm^2), where l_{FS} and l_{recess} are toroidal length of the Faraday shield and perimeter of the inside surface of the guard limiter, respectively. $l_{FS} = 1000 \text{ mm}$ and $l_{recess} = 46 \text{ mm}$ in the present design. We take q_α to the outside surface of the guard limiter to be 7 W/cm^2 . We assume VSWR (voltage standing wave ratio) of the antenna of 15 and a beryllium armor tile to evaluate RF loss on the Faraday shield.

Each heat load integrated on the Faraday shield and the guard limiter is shown in Table 3-2. Total heat loads on the Faraday shield and the guard limiter are about 1360 kW and 550 kW, respectively. Flow rates required for water cooling of the Faraday shield and the guard limiter are 32.4 l/sec and 13 l/sec, respectively, assuming temperature rise of water of 10 °C. Diameter of cooling water pipes of about 12 cm is needed assuming flow speed of 2 m/sec and four pipes.

(2) Ridged waveguide

RF loss of the ridged waveguide (6 m long) is estimated to be about 5% with VSWR \approx 15. Total RF loss is about 1 MW. Required flow rate is 24 l/sec. Diameter of the water cooling pipe is about 9 cm for a main pipe assuming flow speed of 2 m/sec and number of four. Diameter of a branch pipe to each waveguide is about 3 cm.

3.2.4 Vacuum pumping system

Evacuation piping system for the launcher is also indicated in Figs 3-4 and 3-5. The launcher is surrounded by an evacuation jacket in the middle part of the plug. Inside of the ridged waveguides are evacuated through holes ($\phi 75$) made in the side walls of the ridged waveguides as shown in Fig. 3-4. A conductance of the evacuation piping system is estimated to be $0.6 \text{ m}^3/\text{sec}$ (H_2), where we take a diameter of the main evacuation pipe to be 150 mm. Assuming a pumping speed of a pump to be 2000 l/sec, a total conductance is $0.47 \text{ m}^3/\text{sec}$. In order to keep the pressure in the ridged waveguide at a low level (e.g., $<10^{-5}$ Torr), a degassing rate should be less than $2.2 \times 10^{-6} \text{ Pa} \cdot \text{m}^3/\text{sec} \cdot \text{m}^2$ (1.7×10^{-9} Torr·l/sec·cm²). This number is about two order of magnitude larger than the JT-60 data $1.3 \times 10^{-8} \text{ Pa} \cdot \text{m}^3/\text{sec} \cdot \text{m}^2$ (after 350 °C, 48 hours baking), but is smaller by one order than the value before baking ($2.9 \times 10^{-5} \text{ Pa} \cdot \text{m}^3/\text{sec} \cdot \text{m}^2$). Database of a degassing rate during RF injection is necessary for further detailed design.

3.2.5 Tritium safety

All parts of the antenna system in contact with the primary vacuum should have a double containment structure for tritium safety. In addition to the two-stage feedthroughs, another tritium barrier should be inserted between the secondary feedthrough and the matching network. We evaluate tritium permeation into the cooling water of the Faraday shield. Although the materials of the Faraday shield are beryllium and inconel in the present design, we assume stainless steel for calculation because of lack of data base for beryllium and inconel. The calculation is made by using TPERM code.¹⁶⁾ Tritium permeation rate against stainless steel of 10 mm thickness, q , is obtained as

$$q = 2.2 \times 10^{-4} \text{ g/m}^2/\text{day}$$

Surface of the Faraday shield facing to the plasma, S , is about 2 m^2 . Flow rate of the cooling water for the Faraday shield, w , is 1950 l/m. Total volume of the water of the Faraday shield cooling system is $2.9 \times 10^4 \text{ l}$, assuming 15 minutes of a flow cycle. Then the tritium concentration in the cooling water after 2 weeks, D , is obtained by

$$D = \frac{S}{W} \times \int_1^{14} q dt \approx 1.5 \times 10^{-3} \text{ (Ci/l)} \quad (3-1)$$

This value is similar to the one in the cooling water of the first wall.

Tritium influx into the vacuum pumping is also evaluated. Effective pumping speed for DT mixture gas is estimated to be $0.3 \text{ m}^3/\text{s}$, using calculated conductance of the launcher ($0.35 \text{ m}^3/\text{s}$ (DT)) and assuming $2 \text{ m}^3/\text{s}$ pumping speed of the vacuum pumping system. Then the tritium influx into the pumping system is $0.14 \text{ g/day} = 1340 \text{ Ci/day}$ for the pressure inside vacuum vessel of $4 \times 10^{-3} \text{ Pa}$ during operation.

3.2.6 Remote maintenance

Main item of remote maintenance for the launcher is replacement of tiles of the Faraday shield and the guard limiter. They will be renewed once a year because of erosion by disruptions. Two possibilities are considered for replacement of tiles. One is replacement of individual tile by a manipulator in the vacuum vessel. The other is replacement of the front end frame (guard limiter frame with Faraday shield) from the vacuum vessel. Therefore, replacement of the whole launcher plug is not necessary for routine maintenance.

Water cooling pipes to the front end frame are cut with a remote laser welder of in-pipe access. Weight of the front end frame is ~0.94 ton. Therefore, it can be removed with a rail-mouted vehicle proposed for remote maintenance of 1-ton divertor plates in FER.¹⁾ Weight of the launcher with supporting sleeve is estimated to be 70~80 ton. The launcher is pulled out from the port and is housed in a cask. Procedure of the replacement of the front end frame and the launcher plug is depicted in Fig. 3-7.

3.3 Transmission Line System

Each RF power unit delivers power to each antenna channel through a coaxial transmission line. Figures 3-2, 3-3, and 3-9 show the layout of the transmission lines from the RF power units to the launcher. Specifications and cooling design for the transmission system are as follows:

Coaxial line between generator and matching network:

Transmitted power	2 MW
Diameter of outer conductor	9 inch
Characteristic impedance	50 Ω
VSWR	1.5
Number of line	20
Line length	~ 70 m
Transmission efficiency per 70 m of line	0.985 @ 85 MHz
Filling pressure	2 bar (gauge)
Gas	SF ₆ or dry air
Cooling	Water
flow velocity	0.5 m/sec
flow rate	210 l/min
environment temp.	30°C
temp. rise of water	1.4°C

temp. of conductor 47°C

Coaxial line between matching network and ridged waveguide:

Transmitted power	2 MW
Diameter of outer conductor	9 inch
Characteristic impedance	30 Ω
VSWR	10
Number of line	20
Line length	~ 20 m
Transmission efficiency per 20 m of line	0.973 @ 85 MHz
Filling pressure	2 bar (gauge)
Gas	SF ₆ or dry air
Cooling	Water
flow velocity	0.5 m/sec
flow rate	410 l/min
environment temp.	30°C
temp. rise of water	1.3°C
temp. of conductor	53°C

3.4 RF Power System

An output power level of an RF power unit is designed to be 2MW in the frequency range of 50-85MHz with a high power tetrode (X2274 made by Varian Eimac). The following table shows operational parameters of a high power tetrode (X2274) and a driver tetrode (4CW100,000E).

Tetrode	X-2274	4CW-100,000E
Anode Voltage [kV]	25.0	15
Screen Grid Voltage [V]	1,400	800
Control Grid Voltage [V]	-600	-450
Output Power [kW]	2,200	104
Input Power [kW]	82	4
Anode Current [A]	118	9.5
Efficiency [%]	74	73
Screen Grid Current [A]	4.72	0.065
Control Grid Current [A]	4.03	—

Gain [dB]

14.4

14.1

Figures 3-8 (a) and (b) show conceptual drawings of an output cavity for X2274 and 4CW100000E, respectively. Input power needed for each stage of the RF power unit is shown in the following table.

	High Power AMP.	Intermediate AMP.	Oscillator and Solid State AMP.
Anode Power Supply	$2.95 \text{ MVA} \times 1.1 = 3245 \text{ kVA}$	$143 \text{ kVA} \times 1.1 = 157 \text{ kVA}$	
Screen Grid	$6.6 \text{ kVA} \times 2 = 13.2 \text{ kVA}$	$0.6 \text{ kVA} \times 2 = 1.2 \text{ kVA}$	20 kVA
Control Grid	$2.4 \text{ kVA} \times 2 = 4.8 \text{ kVA}$	$0.5 \text{ kVA} \times 2 = 1 \text{ kVA}$	
Filament	$10.5 \text{ kVA} \times 1.2 = 12.6 \text{ kVA}$	$3.3 \text{ kVA} \times 1.5 = 4.95 \text{ kVA}$	
Blower	10 kVA	5 kVA	5 kVA
Total	3285.6 kVA	169.2 kVA	25 kVA

Input Power of 1 unit = 3.5 MVA

Total Input Power of 20 unit = 70 MVA

$$\text{Total Efficiency} = \frac{\text{Total Output Power}}{\text{Total Input Power}} = \frac{2.2 \text{ MW} \times 20}{70 \text{ MVA}} = 63 \%$$

Figure 3-9 shows plan view of the amplifier room. We consider 20 power units in order to deliver 40 MW total generator power and at least 20 MW of torus injection power. Each generator output is fed into each antenna channel. The area of the generator room is $50 \times 30 \text{ m}^2$ and the height is 10 m.

3.5 Total System Efficiency

The total system efficiency at 85MHz is evaluated as follows:

	For VSWR = 5	For VSWR = 10
Generator	0.63	0.63
Transmission line		
Coaxial line		
Generator-stub	0.985	0.985
Stub-ridged waveguide	0.986	0.973
Ridged waveguide ¹	0.98	0.96
Support System	0.97	0.97
(assumed to be 2MVA)		
Total	0.58	0.56

The total system efficiency is thus slightly dependent on the VSWR value in the transmission lines between the stub and the antenna. The total system efficiency is 56–58% with the VSWR of 5–10.

¹ A model of a parallel plate transmission line is used to evaluate transmission loss of the ridged waveguide.

Table 3-1 Heat load on the Faraday shield and the guard limiter

Radiation (q_p)	15.4 W/cm ²
Nuclear heating (q_n)	10 W/cm ³
Alpha particle loss (q_α)	
to Faraday shield	0
to guard limiter	
(inside surface)	160 W/cm ²
(outside surface)	7 W/cm ²
RF Loss on Faraday shield (VSWR=15)	
low-Z part	
beryllium	0.38 W/cm ² (Max 8.7 W/cm ²)
graphite	11.8 W/cm ² (Max 267 W/cm ²)
inconel part	0.5 W/cm ² (Max 10.9 W/cm ²)

Table 3-2 Heat load and water cooling for the launcher

	Radiation (kW)	α particle loss (kW)	Nuclear heat (kW)	RF loss (kW)	Total load (kW)	Required flow rate (l/sec)
Faraday screen	380	-	630	350	1360	32.4
Guard limiter	-	340	220	-	550	13
Ridged W.G.	-	-	-	1000	1000	24

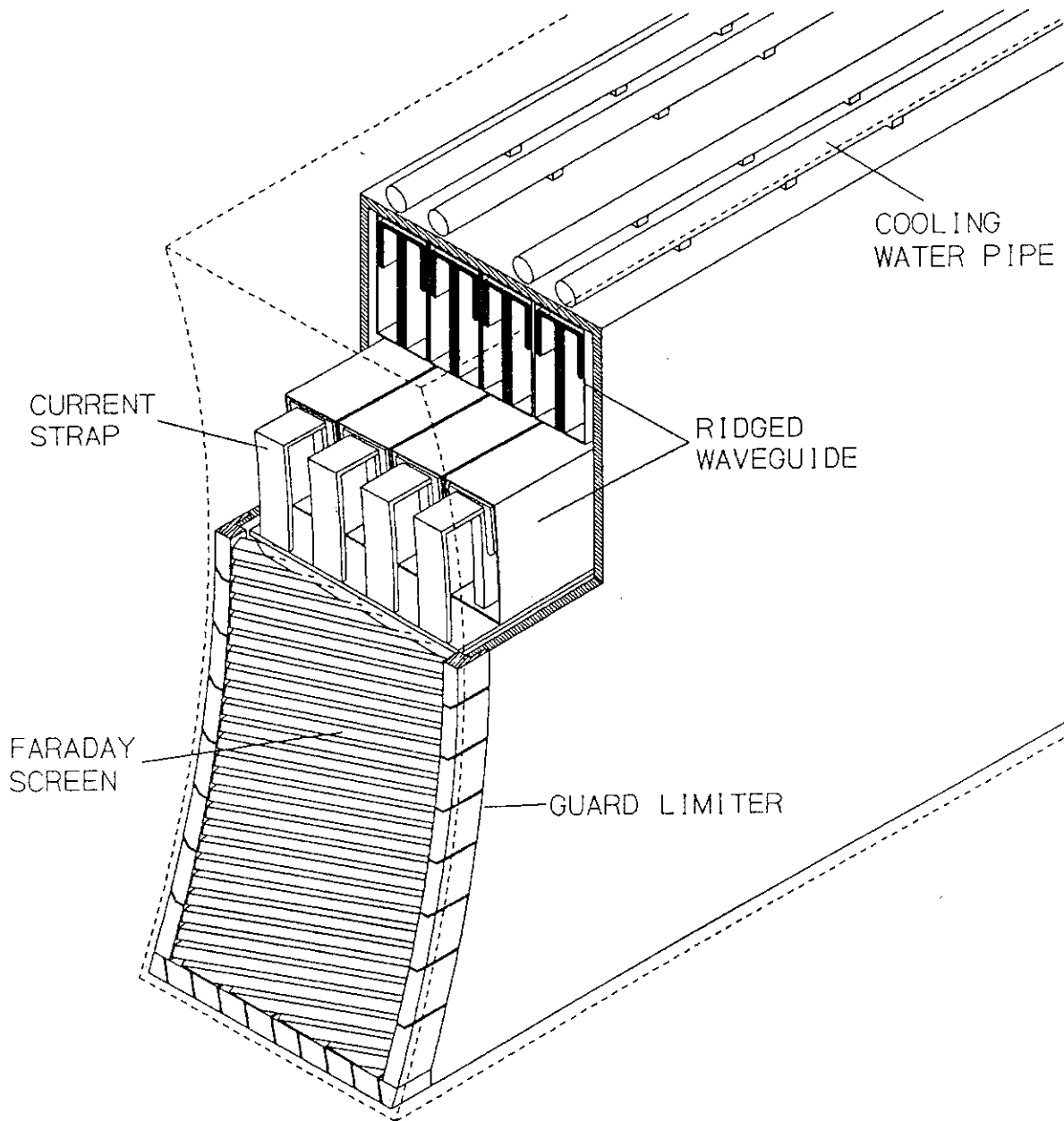


Fig. 3-1 Perspective view of the FER IC antenna.

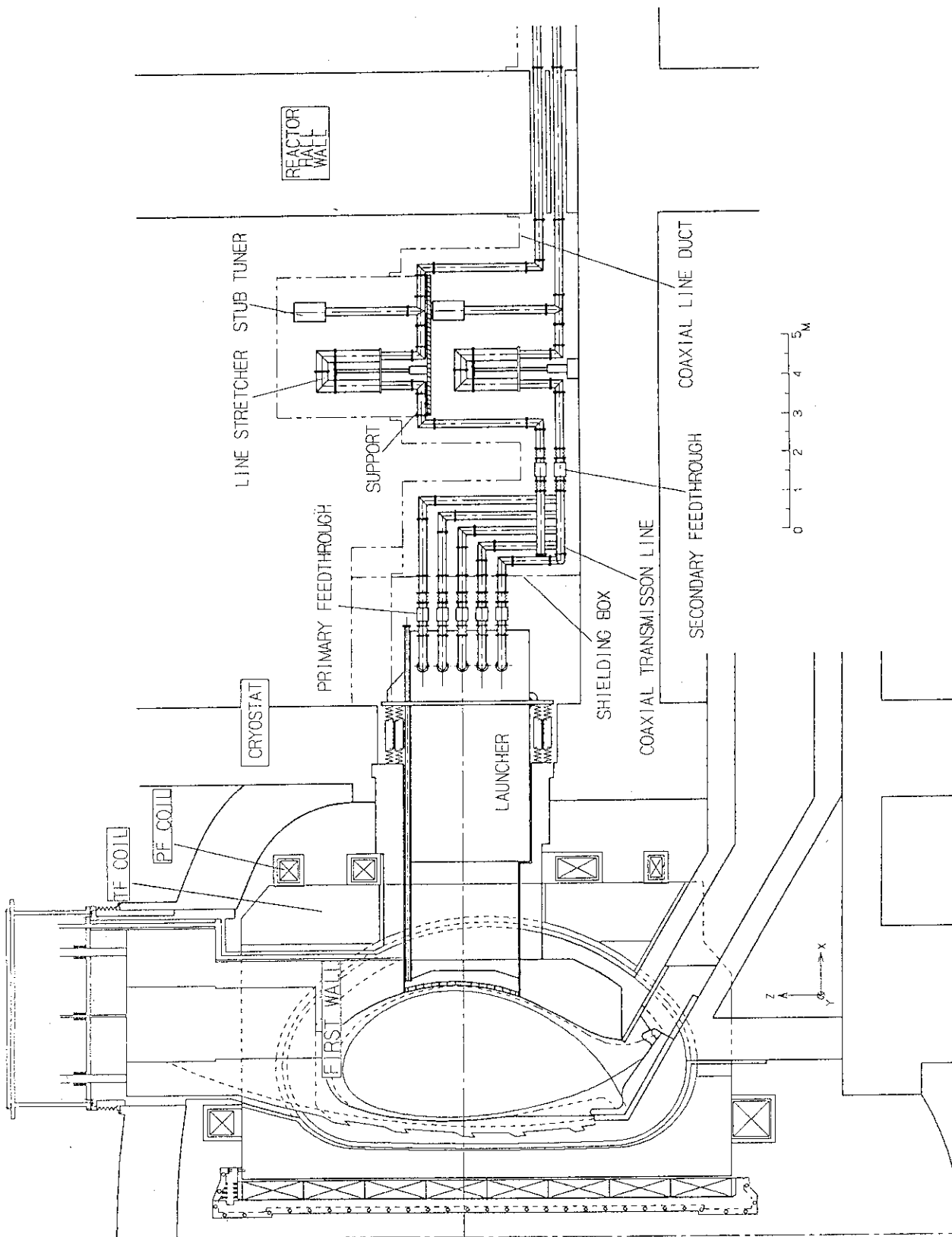


Fig. 3-2 Side view of the FER IC launching system.

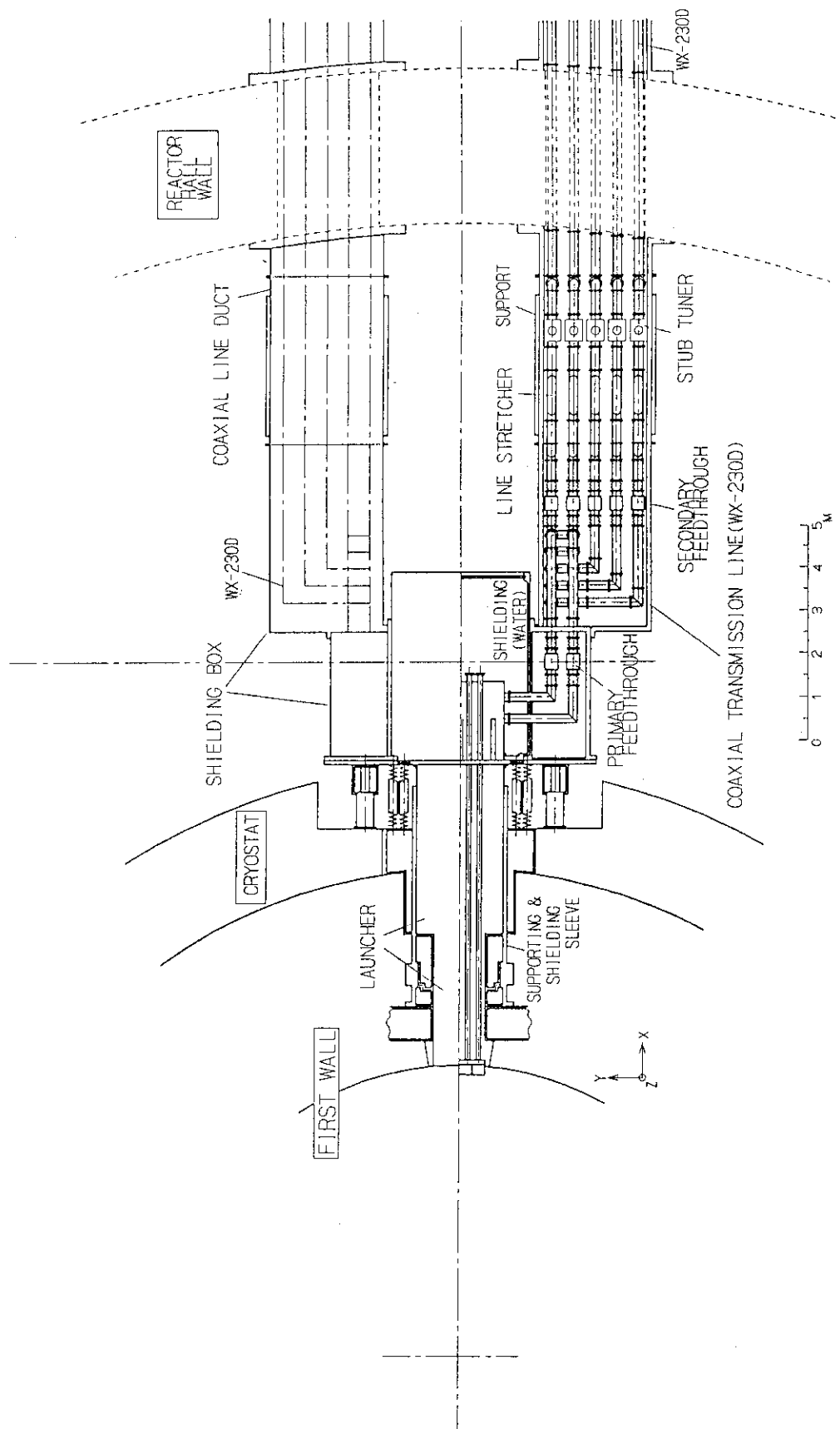


Fig. 3-3 Top view of the FER IC launching system.

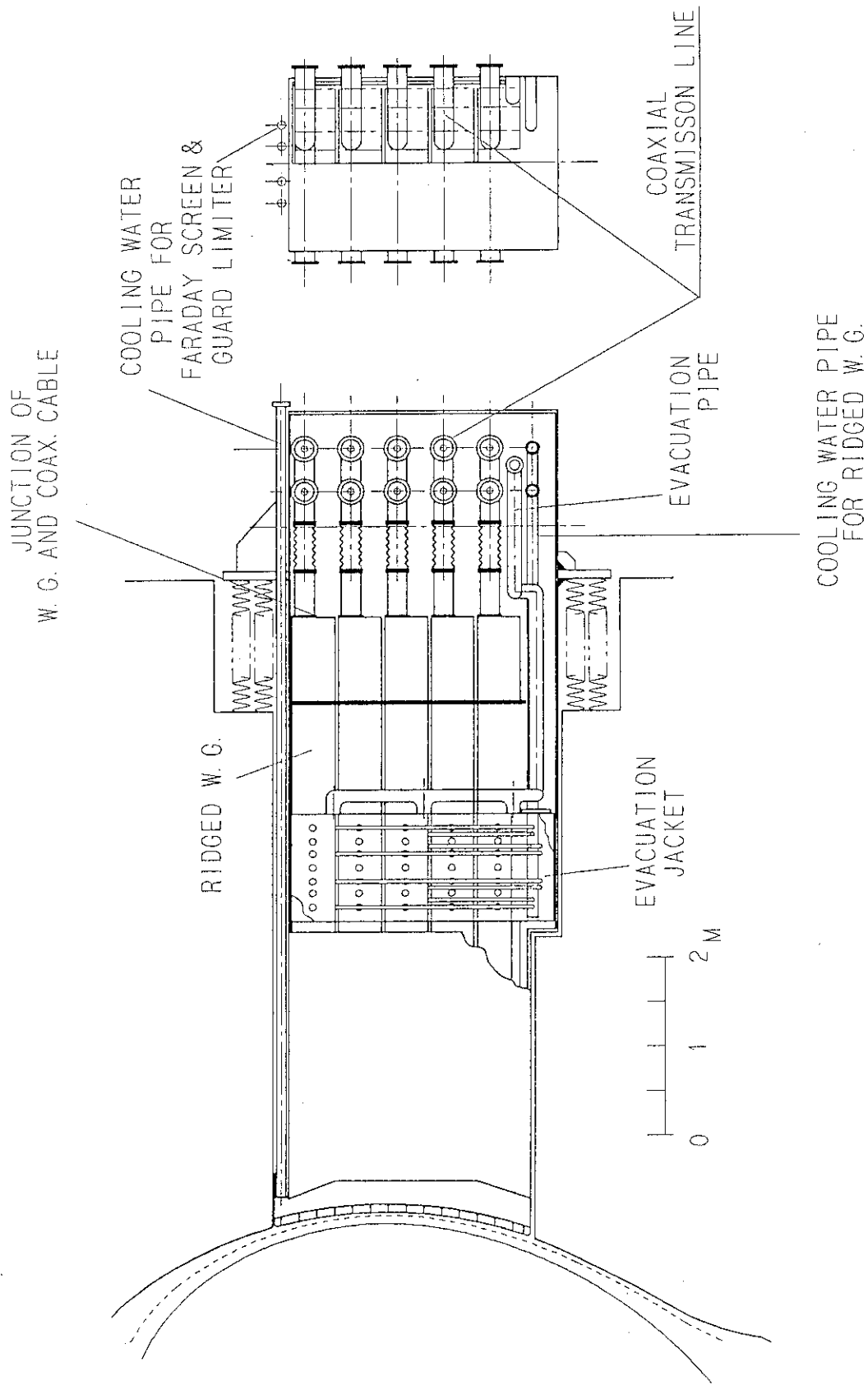


Fig. 3-4 Side and rear views of the FER IC launcher.

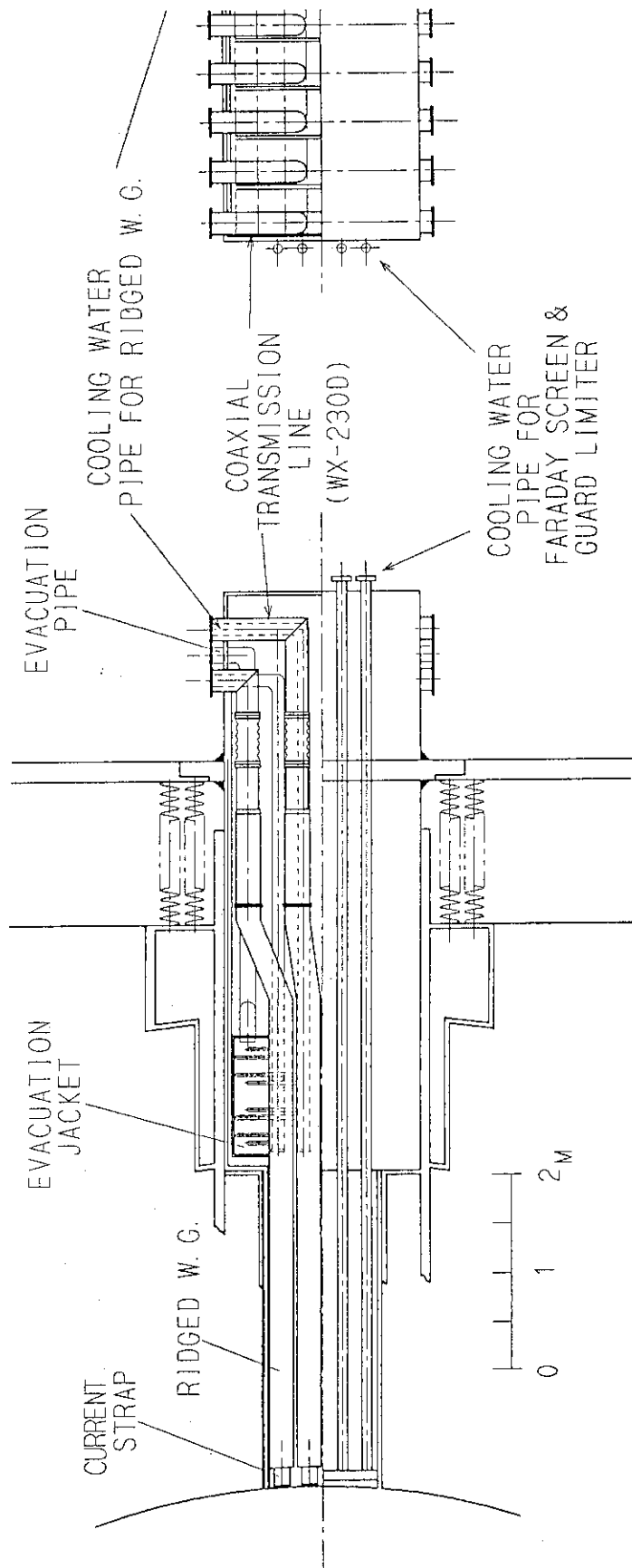


Fig. 3-5 Top and rear views of the FER IC launcher.

FER IC Launching System

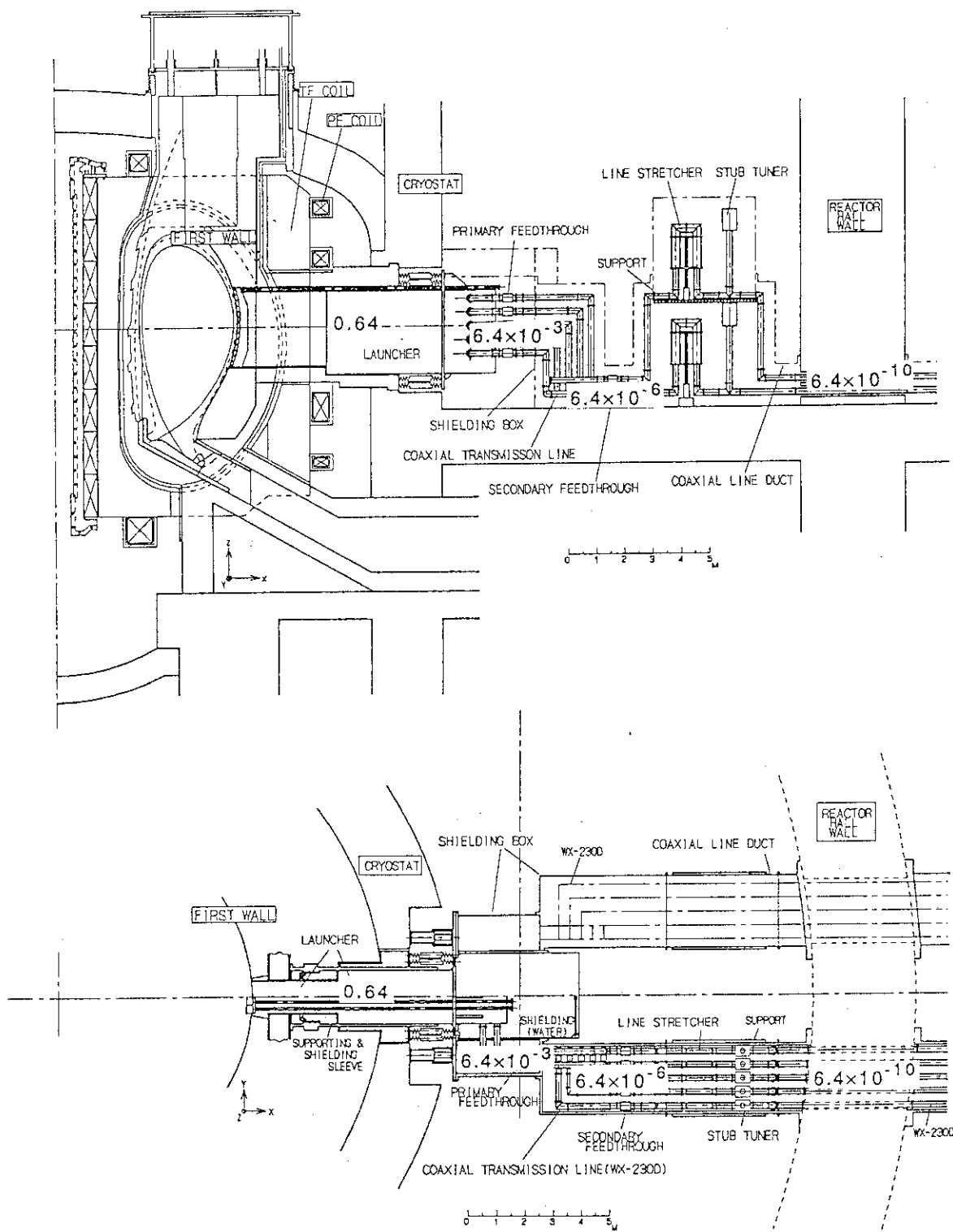


Fig. 3-6 Reduction of the dose rate from the first wall.

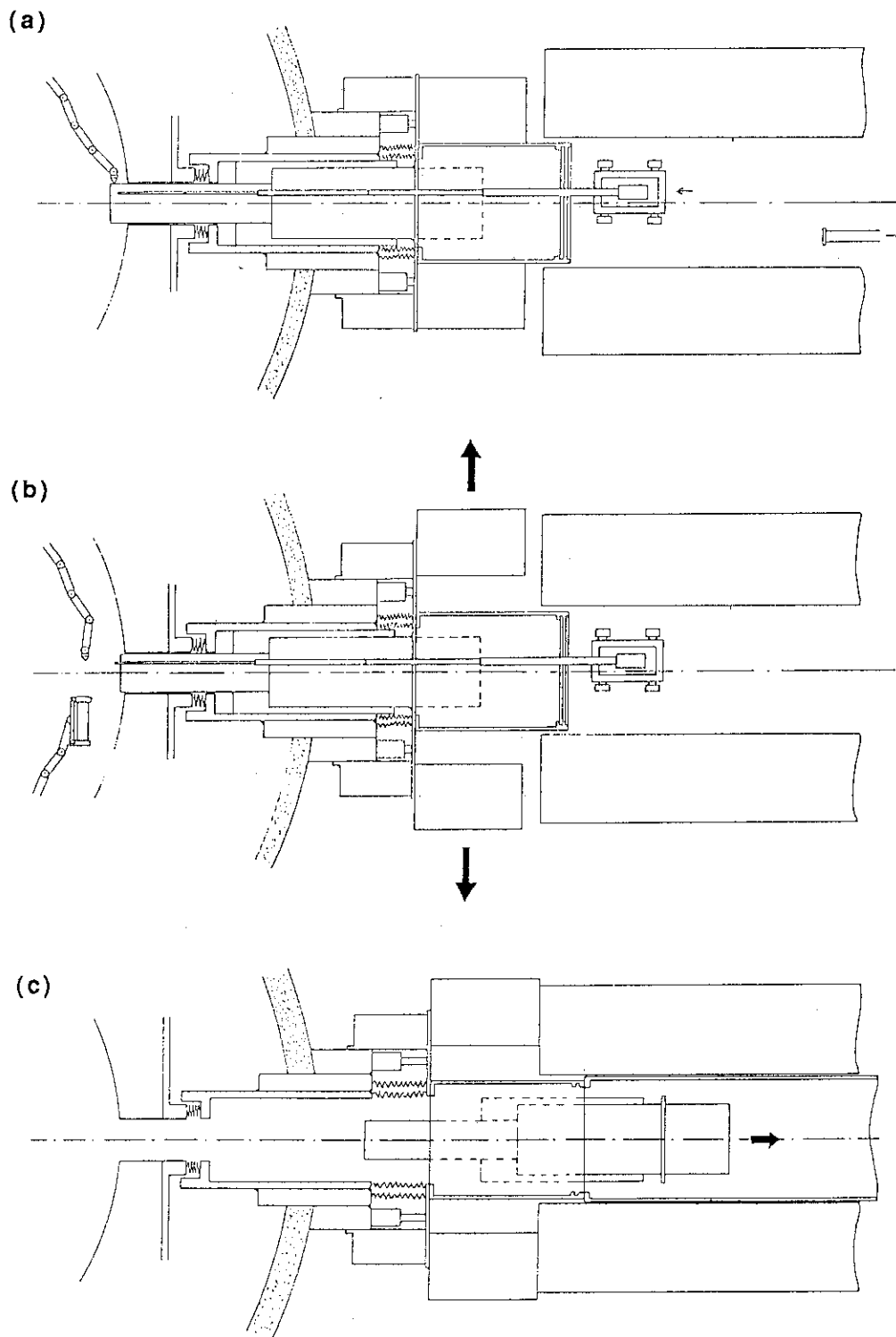


Fig. 3-7 Concept for remote maintenance of the Faraday shield and the guard limiter ((a)-(b)) and the launcher plug ((b)-(c)).

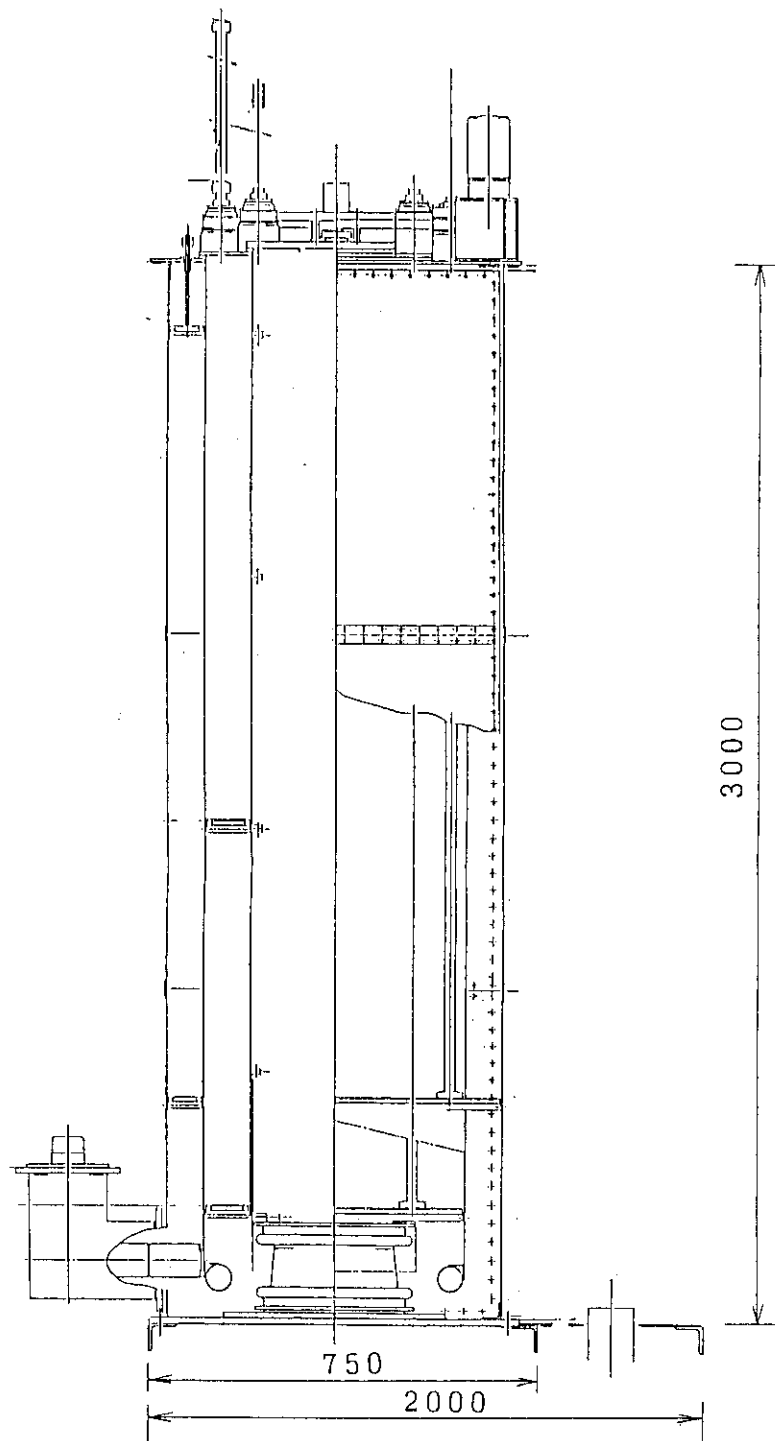


Fig. 3-8 (a) Conceptual drawing of the output cavity for X2274.

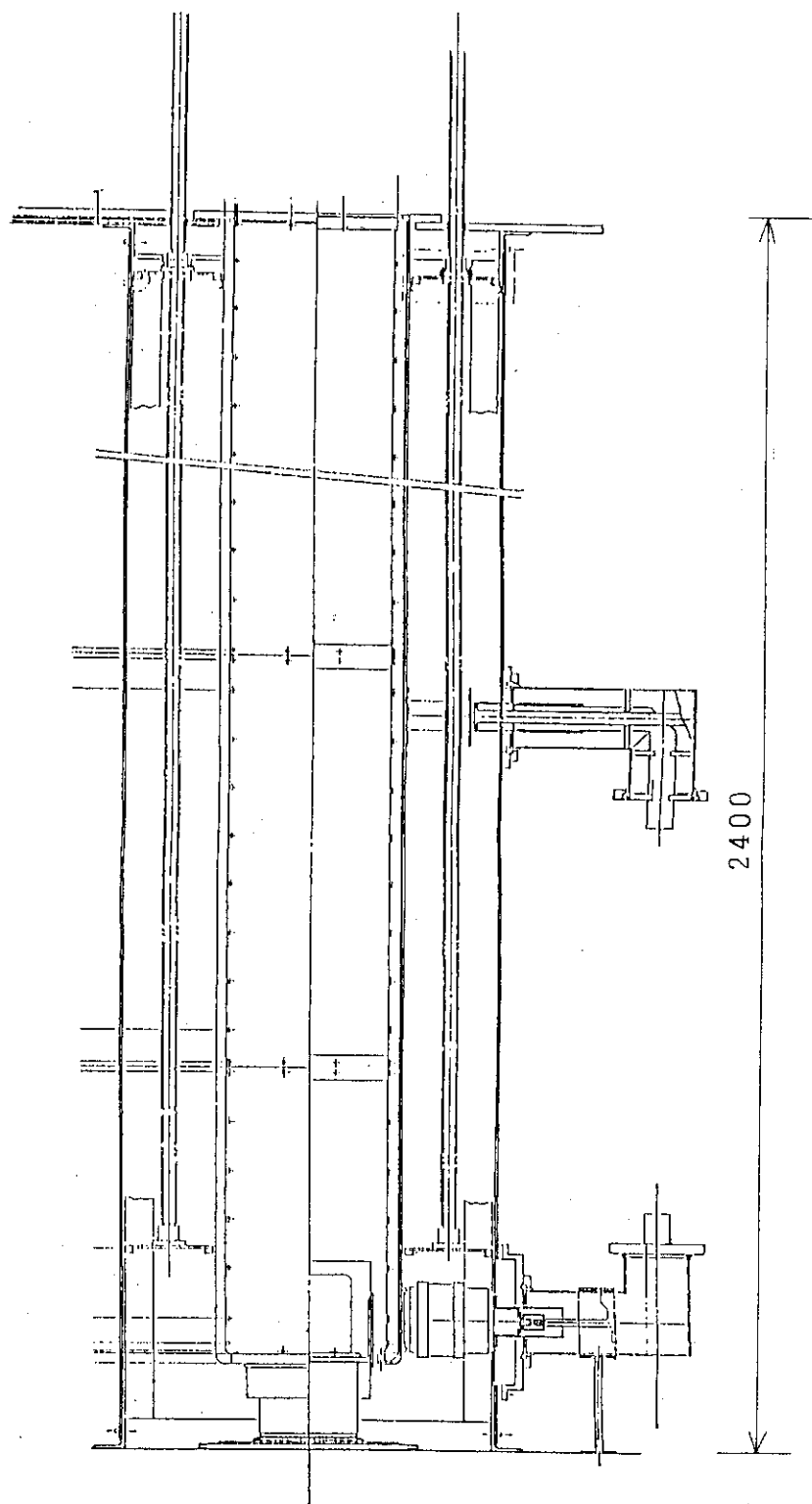


Fig. 3-8 (b) Conceptual drawing of the output cavity for 4CW100000E.

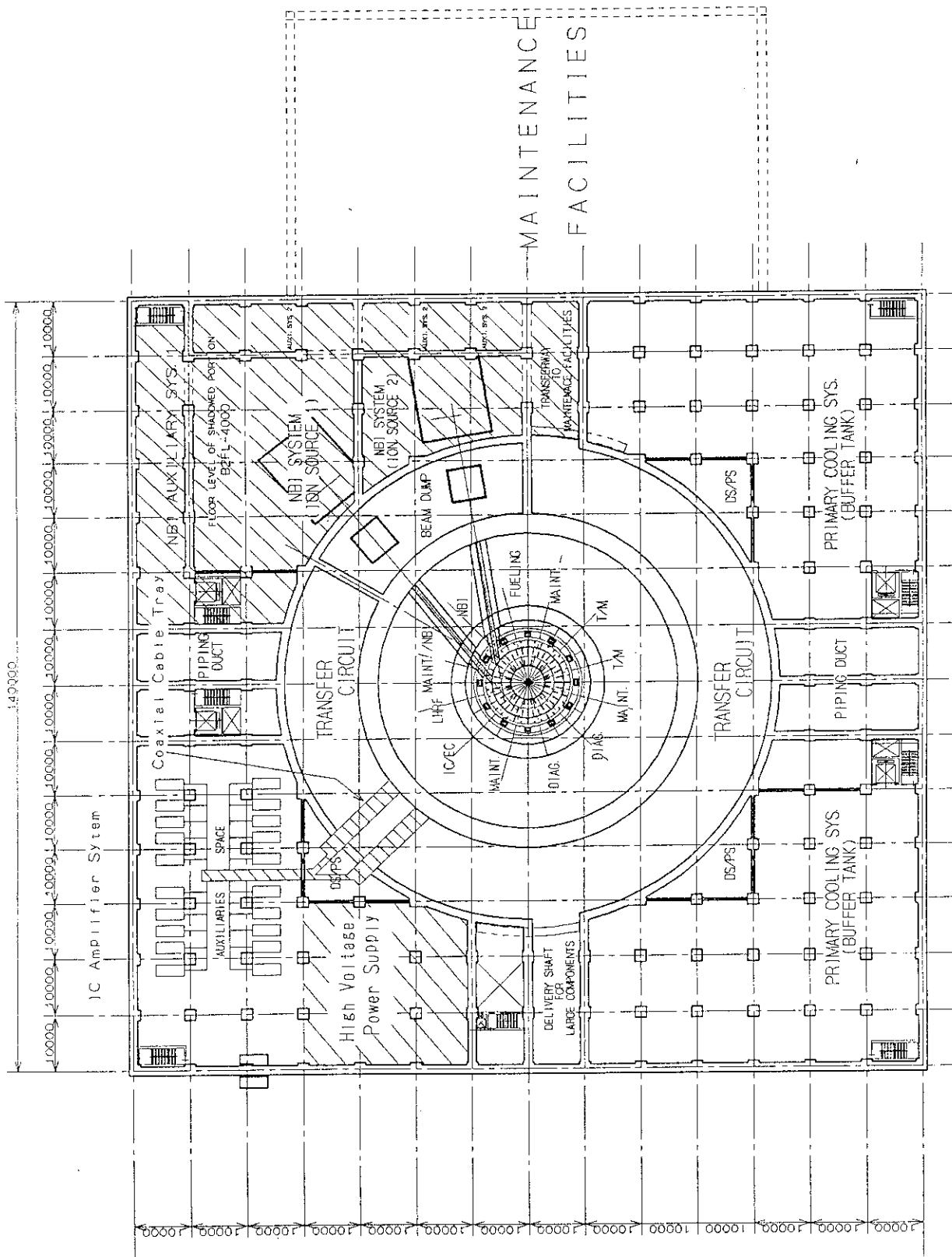


Fig. 3-9 Plan view of the FER IC system showing the layout of the transmission lines and the RF power units.

4. ANTENNA DESIGN AND ANALYSIS

4.1 Basic Structure

Figures 4-1 and 4-2 show respectively front and side views of the front part of the FER IC launcher. A phased loop antenna array is used as radiation elements. Number of current straps is 20 (4 in toroidal direction and 5 in poloidal direction). The size of each current strap is 16 cm in width, 48 cm in length and 20 cm in depth. Each current strap is directed in the same way. RF current is fed from the top part of each current strap. Short-circuit is located in the bottom part of each current strap. The distance between central lines of adjacent current straps is 24.8 cm. Septa between adjacent current straps will be necessary to reduce mutual coupling between straps adequately and that not to give unfavourable effects on wave spectrum. Each current strap is connected by a T-shaped ridged waveguide with arms, which plays a role of a vacuum transmission line. Therefore, no ceramic support is needed inside the cryostat. Cross-section of the ridged waveguide is 485 mm (height) \times 228 mm (width). Thickness of an outer wall of the ridged waveguide is 5 mm. Gaps between the ridge and the wall is 12 mm in toroidal direction and 8 mm in poloidal direction. By selecting a length of the arm to be 205 mm, cutoff frequency of the waveguide can be reduced as low as 43 MHz (see Fig. 4-13).

The Faraday shield is single-layer and open-type, which is favourable for reducing RF loss and has been demonstrated to be quite effective in JT-60.¹⁷⁾ The Faraday shield is made of water-cooled inconel pipe whose cross-section is parallelogram (48 mm in height and 43 mm in depth, see Fig. 4-17). The plasma-facing side is protected by replaceable tiles of low-Z material (beryllium). Thickness of the tile must be so large as to withstand erosion associated with disruptions and to match frequency of remote maintenance (at most once per year). Faraday shield will be inclined to follow the magnetic field lines (≈ 15 degrees). A front end frame including the Faraday shield and the guard limiter is detachable from the main body for the remote maintenance.

Specifications of the FER IC launcher are as follows.

Injected power	20MW
Frequency	50-85 MHz
Port	
type	horizontal port
size	3 m (H) \times 1.2 m (W)
number	1
Launcher size	2.75 m (H) \times 1.14 m (W)

	2.895m(H) with cooling pipe
Power density at the Faraday shield	6.4 MW/m ²
Radiation element	loop antenna array
Vacuum transmission line	ridged waveguide
Current straps	
number	4 toroidally 5 poloidally
size	16 cm (W) 48 cm (H) 20 cm (D)
distance between adjacent straps	24.8 cm
gap to Faraday shield	15 mm
Ridged waveguide	
size	485 mm (H) 228 mm (W)
gap between ridge and wall	12 mm (// B) 8 mm (⊥ B)
Faraday shield	
cross-section	50 mm (H) 43 mm (D)
pitch	66 mm
inclination	15° to toroidal direction

Difference between the FER antenna and the high frequency ITER antenna is minor. Because of higher frequency range for ITER (70-110 MHz), the length of current straps is 36 cm and the arm length of the ridge is 75 mm for the ITER antenna.⁹⁾

4.2 Antenna-Plasma Coupling

4.2.1 Coupling calculation

The antenna-plasma coupling is calculated with a three dimensional antenna coupling code including radial feeder currents.¹⁸⁾ The code is based on cold plasma and strong damping model, i.e. the wave field is calculated by a multi-layer method in a region between a conducting wall including an antenna and a certain layer inside a plasma from which waves are not reflected. Namely, we assume that waves are perfectly absorbed

beyond that layer. The code predicts coupling resistances of the JT-60 2×2 antenna satisfactorily.¹⁹⁾ Exact antenna configuration, i.e., 5×4 array, is taken into account in the code. A geometry for the antenna-plasma coupling calculation is shown in Fig. 4-3. A distance between the guard limiter and the current strap, d , is 73 mm, which includes the Faraday shield thickness of 43 mm. A standard value of the distance between the separatrix and the antenna guard limiter is 15 cm. Two types of the electron density profile in the scrape-off layer (H-mode and L-mode) are considered for FER/ITER. Typical examples are shown in Fig. 4-3, whose parameters are indicated below:

	$n_e(\text{separatrix})$	e-folding length, λ_n
H-mode	$6.6 \times 10^{19} \text{ m}^{-3}$	2.1 cm
L-mode	$4.0 \times 10^{19} \text{ m}^{-3}$	3.7 cm

Scrape-off density profile of H-mode is employed in the present coupling calculation, since this is more severe condition for antenna-plasma coupling than L-mode one.

The coupling code gives an antenna radiation impedance of each current strap ($Z_R(i) + jZ_I(i)$, $i=1\sim 20$). We assume that an antenna input impedance, Z_A , is given approximately by $Z_A = (Z_R + jZ_I) / ((\sinh \alpha L_a)^2 + (\cos \beta L_a)^2)$, where α is an equivalent attenuation constant of the antenna as a transmission line, β the phase constant and L_a the antenna length. We derive α from the relation $Z_R = 1/2 \cdot Z_0 \cdot \sinh 2\alpha L_a$, where Z_0 is the characteristic impedance of the antenna. A coupling resistance R_c is defined as an equivalent loading resistance when the antenna is connected with a transmission line of the characteristic impedance Z_i . R_c is expressed as

$$R_c = \frac{Z_i}{\rho} \quad (4-1)$$

$$\rho = \frac{1+\Gamma}{1-\Gamma} \quad (4-2)$$

$$\Gamma = \sqrt{\frac{(\text{Re}(Z_A) - Z_i)^2 + (\text{Im}(Z_A))^2}{(\text{Re}(Z_A) + Z_i)^2 + (\text{Im}(Z_A))^2}} \quad (4-3)$$

We evaluate a coupling capability of the antenna system with the coupling resistance and the real part of the antenna radiation impedance, because they are closely related with a power handling capability of the antenna system as discussed in 4.2.3. We take averaged values of the coupling resistance and the real part of the antenna radiation impedance over all current straps for simplicity.

4.2.2 Coupling properties

We show coupling properties of the 5×4 array. Matching of the current strap and the ridged waveguide is an important point for consistency of this antenna system. Length (L_a) and width (W_a) of the current strap are set to be 0.48m and 0.16 m, respectively. 0.48 m of L_a is the maximum allowable antenna length in the present antenna design and corresponds to a quarter wavelength at 90 MHz including reduction of wavelength by the Faraday shield. The characteristic impedance of the ridged waveguide ranges $28 \Omega \sim 16 \Omega$ in the frequency range of 50 MHz \sim 85 MHz (see Fig. 4-13).

(1) Loading impedance and coupling resistance

Figure 4-4 shows Z_R , Z_I and R_c as a function of frequency. A parallel refractive index corresponding to a peak position of the antenna current spectrum, $N_{||}(p)$, is set to be unity in this case, since low $N_{||}$ is required for the central ion heating (see Sec. 2.2). Phase differences between toroidally adjacent current straps are $14.7^\circ \sim 25.0^\circ$ for 50 MHz \sim 85 MHz. Phase difference in the poloidal direction is zero. As shown in Fig. 4-4, good coupling capability can be expected in the frequency range of 50 MHz \sim 85 MHz. Z_R increases monotonically with increasing frequency. Absolute value of Z_I approaches to zero at 85 MHz, since the antenna length is chosen to be a quarter wavelength at 90 MHz. As the characteristic impedance of the ridged waveguide decreases with increasing frequency, R_c takes the largest value ($\sim 6 \Omega$) at a frequency of 47 MHz, which is near the cut-off frequency of the ridged waveguide. R_c decreases rapidly at 50 MHz and takes a value of $3 \sim 5 \Omega$ in the frequency range of 50 MHz \sim 85 MHz.

(2) Antenna radiated power spectra

Figures 4-5 (a) and 4-5 (b) show the antenna radiated power spectra at 50 MHz and 80 MHz, respectively. Almost all radiation concentrates in a region below $|N_{||}|=1$. Remarkable peaks appear just below $|N_{||}|=1$. They are due to a coaxial mode, which is excited by radial feeder currents. They can propagate inside the plasma region if the density gradient is not too steep. Actually, the radiated spectrum at the antenna surface coincides with the one at the non-reflection surface in the plasma in the calculation. As indicated in Fig. 2-2, the power is absorbed in a single pass with $N_{||}(p)=1$. Thus, the coaxial mode has a potentiality to improve the coupling capability in keeping good heating capability (single pass absorption and central power deposition).

(3) Dependence on antenna-plasma distance

Figure 4-6 shows dependence of R_c on the antenna-plasma distance, d , at various frequencies. The d -dependence of R_c is not so strong, since the coaxial mode is dominant

in the antenna radiation. Reduction of R_c with increasing d becomes less significant with increasing frequency.

(4) Comparison with other antenna configuration

In the present design, each current strap is directed in the same way. RF current is fed from the top part of each current strap. Each current strap is short-circuited at each ground plate (or toroidal septum). In this design, the radial feeder current tends not to be cancelled each other. This is the reason why the coaxial mode is relatively strong. We compare this type of poloidal antenna configuration (Type A in Fig. 4-7) with other type of antenna configuration (Type B in Fig. 4-7). In the case of Type B, two current straps are coupled and RF currents are fed from the top and the bottom of each current strap. Therefore, feeder currents are cancelled at the short-circuit. Then, the coaxial mode is less significant than in the case of Type A. Figure 4-8 shows Z_R , Z_I and R_c for 4×4 array with Type B configuration as a function of frequency. Z_R decreases with increasing frequency, since the coaxial mode becomes smaller with decreasing feeder current with increasing frequency. Behaviour of Z_I is similar with the case of the 5×4 array with Type A configuration. A value of R_c becomes much smaller in comparison with the case of the 5×4 array, because the antenna input impedance is high and matching of the antenna with the ridged waveguide with low characteristic impedance is poor. A transmission line with much higher characteristic impedance is suitable for this antenna system. Antenna radiated spectra of the 4×4 array with Type B configuration are indicated in Figs 4-9 (a) and (b). It is found that the coaxial mode becomes less significant with this configuration than with Type A configuration as shown in Figs 4-5 (a) and (b). Especially, difference between them at 80 MHz is significant.

4.2.3 Power injection capability

Power injection capability of the launcher is evaluated with following formulas.

$$P_a \text{ (MW) - limited in loop antenna part} = 10 \cdot Z_R \frac{V_{Amax}^2}{Z_{0A}^2} \quad (4-4)$$

$$P_a \text{ (MW) - limited in ridged waveguide part} = 10 \cdot R_c \frac{G^2 \cdot E_{max}^2}{Z_i^2} \quad (4-5)$$

Z_R ;	real part of the antenna radiation impedance
R_c ;	antenna coupling resistance
Z_{0A} ;	characteristic impedance of loop antenna (40 Ω)

Z_i ;	characteristic impedance of ridged waveguide ($16 \Omega \sim 28 \Omega$, dependent on frequency)
V_{Amax} ;	maximum voltage in the loop antenna part (35 kV)
E_{max} ;	maximum electric field generated at the gap of the ridged waveguide (20 kV/cm)
G ;	gap length of the ridged waveguide (1.2 cm)

Figure 4-10 shows the 5×4 array antenna injection power limited by the ridged waveguide part as a function of frequency. The launcher can afford to have 20 MW injection power capability in the frequency range of 50 MHz \sim 85 MHz. The power limited at the loop antenna part is also high enough because of large Z_R in this frequency range.

4.3 Analysis of T-shaped Ridged Waveguide with Arms

4.3.1 Introductory remarks

Ridged waveguides have an electrical small cross section to propagate waves less than the cutoff frequency of a rectangular waveguide.²⁰⁾ The cutoff frequency is decreased by increasing a ridge surface, such as a T-shaped ridge.^{21,22)} The cutoff frequency of the T-shaped ridged waveguide can be decreased further by using a small gap between the ridge and the waveguide inner wall. However, it is not permitted for high power application to have very small gap spacing which causes the electric field break down.

To decrease its cutoff frequency without using small gap spacing, a T-shaped ridged waveguide with arms is presented in this section. The cutoff frequency, the waveguide impedance, and the field distribution of the ridged waveguide with arms are calculated by finite element method to obtain an electrical small waveguide.

4.3.2 Cutoff frequency

The cutoff frequency f_c of a T-shaped ridged without arms, $P_3=0$ in Fig. 4-11 (a), is calculated approximately as following equation.

$$f_c = (c/\pi) \sqrt{P_1/(W \cdot H \cdot A)} \quad (4-6)$$

where c is the velocity of light, and $A=W-2 \times P_2$. One method to reduce the cutoff frequency for constant waveguide cross section $W \cdot H$ is obtained by decreasing P_1 , however, which is not appropriate for high power application. Another technique to increase the ridge length A , is given by adding arms to the both sides of the ridge shown in Fig. 4-11 (a). This structure does not have small gap spacing inside the waveguide to

reduce the cutoff frequency. To investigate this waveguide characteristics, a finite element method (FEM) is used in this section.²³⁾

The dominant mode propagating in the z direction of this waveguide is a TE mode, and its fields are expressed by a potential Φ as follows.

$$\vec{E} = -j\omega\mu\vec{\nabla}\times\Phi\vec{z} \quad (4-7)$$

$$\vec{H} = \vec{\nabla}\times\vec{\nabla}\times\Phi\vec{z} \quad (4-8)$$

where ω is the angular frequency, μ is the permeability in free space, and \vec{z} is a unit vector in the z direction, respectively. To evaluate the cutoff frequency of this waveguide, the FEM is used by a following functional $\Gamma(\Phi)$.

$$\Gamma(\Phi) = \frac{1}{4}\mu k^2 \iint (k^2\Phi^2 - \Phi_x^2 - \Phi_y^2) dx dy \quad (4-9)$$

where k is the wavenumber of the waveguide, Φ_i is the partial derivative of Φ about i , and the waveguide cross section is in the xy plane. In the following calculation, the waveguide cross section is divided by 67 triangles, and the potential in each element is approximated by the second order polynomial.

Table 4-1 shows cutoff frequencies as a function of the arm length P3 for four sets of P1 and P2 parameters. Parameters of the waveguide cross section, H and W, are 456 mm and 228 mm, respectively. Gap spacings P1 and P2 are larger than 10mm not to make large electric fields inside there. The cutoff frequency is decreased by increasing P3. For example, the cutoff frequency is 61.42(MHz) for the waveguide P1=P2=12(mm) with no arms P3=0(mm). Therefore, the cutoff frequency is reduced 20% by using arms P3=205(mm), rather than the waveguide without arms P3=0, which shows the effect of the arms to decrease the cutoff frequency without using small gap spacing. The cutoff frequency is decreased by using long length arms in each parameter in Table 4-1.

4.3.3 Waveguide impedance

The waveguide impedance should be matched to an antenna impedance to suppress the reflection waves from the load. The waveguide impedance of the ridged waveguide is approximated by dividing the voltage squared at center of the ridge by a transmitting power on the analogy of a rectangular waveguide.

Figure 4-12 shows calculated waveguide impedance for four sets of P1 and P2 parameters with the waveguide cross-section for FER and ITER (485 mm in height and

228 mm in width). The waveguide impedance is diverged at the cutoff frequency, and is converged for more than 60MHz in each parameters. The waveguide impedance is reduced by large arm length, because the center electric field strength is decreased by long arms. Electric fields between the ridge and the waveguide wall is expanded by the long arms, which reduces the electric field strength.

For the FER IC antenna (50 MHz ~ 85 MHz), $P1 = 8$ mm, $P2 = 12$ mm and $P3 = 205$ mm are adopted, while for the high-frequency ITER IC antenna (70 MHz ~ 110 MHz), $P1 = P2 = 12$ mm and $P3 = 75$ mm are taken. Waveguide impedance calculated with the parameter set for FER is shown in Fig. 4-13.

4.3.4 Electric field distribution

For high power application, sharp edges of the ridge should be rounded not to make large electric fields there. The electric field has a singular condition at those points theoretically. In general, those edges can be cut to avoid the singular condition without changing the waveguide characteristics. Figure 4-14 shows the electric field distributions along the ridge for four shaped ridges in Fig. 4-11 (b). Two peaks appears for the ridge without cut edge at points 4 and 7 in Fig. 4-14 (a). The first peak is disappeared by large cut of Fig. 4-14 (b) and (d), and is reduced by small cut of Fig. 4-14 (c). The electric field distribution for two cut edges of Fig. 4-14 (d) becomes almost uniform by the point 6, which verifies the effect of cut edge. It should be noted that cutoff frequencies for four kinds of ridge are changed only 2.5% by cut edges. This result indicates that the ridge edges can be cut without changing the waveguide characteristics.

To verify the effect of cut edges to decrease the electric field strength, electric field distributions of another parameter (FER waveguide parameter) are shown in Fig. 4-15, where the electric field strength at point 1 is also presented for 1 MW power transmission. In this example, electric field at the point 4 edge is also decreased by the edge cut.

4.3.5 Transmission loss

Transmission loss of T-shaped ridged waveguide with arms are calculated by currents flowing along the waveguide. The current distribution is given by tangential components of magnetic field along the inner wall of the waveguide. For the parameter of Fig. 4-15 and conductivity of copper, transmission losses are shown in Fig. 4-16. The waveguide without cut edges has more than five times transmission loss than the waveguide with cut edges. The current flowing along the ridge becomes very large at the edges, and are suppressed by cut edges. True value of the transmission loss of the waveguide, however, will be much less if we take realistic round corners of the ridge and the waveguide wall into account.

4.3.6 Concluding remarks

The ridged waveguide with arms to decrease the cutoff frequency without using small gap spacing in the waveguide is presented to obtain an electrically small waveguide for high power microwave transmission. The cutoff frequency and waveguide impedance of the waveguide are calculated by the finite element method, and the cutoff frequency of the waveguide with arms can be reduced 20% less than the waveguide without arms. Electric field distributions are also calculated, and the cut edge is efficient to obtain a uniform electric field distribution in the waveguide without changing the waveguide characteristics.

4.4 Analysis of Faraday Shield

The current straps are protected from direct impinging of neutral particles by a Faraday shield, which also plays an important role in cancelling a parallel electric field in order to minimize coupling with the slow wave. The Faraday shield is protected by guard limiters from direct bombardment of charged particles including energetic alpha particles. The frame of the Faraday shield and the guard limiter is detachable from the launcher for maintenance.

A thick and open-type Faraday shield is proposed for the FER IC system and the high-frequency ITER IC system. Thickness and height of each pipe of the Faraday shield is 43 mm and 48 mm, respectively. Pitch of the pipe is 66 mm. Cross-section and detailed dimensions of the Faraday shield are shown in Fig. 4-17. Heat loads on the Faraday shield are shown in Table 3-1. RF loss on the graphite is the most severe heat load on the Faraday shield. Beryllium is an attractive material for the armor plate in order to reduce RF losses as well as impurity radiation. Replaceable beryllium armor plates are assumed to be employed for this reason. Figure 4-18 shows a calculation model for analyzing steady-state temperature profile and thermal stress of the Faraday shield as well as material of each part of the Faraday shield. Temperature contour of the Faraday shield with beryllium armor plate is shown in Fig. 4-19. The highest temperature (370 °C) appears on the lower corner of the armor plate due to the highest RF loss density there and up-and-down asymmetry of the distance from the heat sink (molybdenum bolt). The stress contour and the deformation of the Faraday shield with beryllium armor plates are shown in Fig. 4-20 and Fig. 4-21. The maximum stress (54 kgf/mm²) appears in the molybdenum washer inserted between the beryllium tile and the inconel pipe. This value is smaller than the limit value ($3S_m=85$ kgf/mm²) of molybdenum. The maximum stress in the beryllium tile (~20 kgf/mm²) is smaller than the limit value (29.5 kgf/mm²), too. The maximum deformation which is found at the lower corner of the armor plate is 0.12 mm. Consequently, there is no problem on the thermal stress of the Faraday shield with beryllium tiles.

4.5 Analysis of Guard Limiter

An example of the design of the antenna guard limiter for the FER IC system and the high frequency ITER IC system is shown in Fig. 4-22. Main role of the guard limiter is protection of the Faraday shield from charged particles. As a radial position of the guard limiter is flush to the first wall in a standard case, the guard limiter receives large heat flux mainly due to alpha particles as discussed in 3.2.3 (1). The heat loads on the guard limiter are given in Table 3-1. Figure 4-23 shows a model for thermal analysis of the guard limiter. A plasma-facing part of the guard limiter is made of graphite or carbon-carbon composite. Due to a relatively large heat flux, the graphite or carbon-carbon composite part (hereafter we call this low-Z part) should be closely contacted with a heat sink (water cooling pipe of copper) by brazing. The low-Z part is connected by a molybdenum plate, through which the guard limiter is attached on the launcher jacket by bolts. Such kind of the antenna guard limiter except the close contact heat sink was successfully applied for the JT-60 ICRF antenna. A material of the launcher jacket is stainless-steel. It is assumed that cooling water flows with a speed of 2 m/s inside the copper pipe and the jacket wall.

Temperature contour of the guard limiter is indicated in Fig. 4-24. We assume that a heat transfer coefficient at the brazing region between the low-Z part and the copper pipe is $1.0 \times 10^{-2} \text{ W/cm}^2 \cdot ^\circ\text{C}$. The maximum temperature which appears in the low-Z part is 990°C , which is well below the limit for the graphite. The maximum temperature of the molybdenum plate is 300°C , which appears at the middle point of the portion facing the thick wall of the launcher jacket. A constraint condition for the thermal stress analysis is indicated in Fig. 4-25. The guard limiter is assumed to be free only in the radial direction. The stress contour is shown in Fig. 4-26. The stress in the low-Z part is less than 10 kg/mm^2 . There is no problem in this part. The maximum stress in the molybdenum part is 74.8 kgf/mm^2 , which is less than the allowable value for molybdenum ($3S_m = 85 \text{ kgf/mm}^2$). The maximum stress which appears in the launcher jacket is 67.4 kgf/mm^2 , which exceeds the allowable value for stainless-steel ($3S_m = 40.5 \text{ kgf/mm}^2$). It is necessary to change the material of the front part of the launcher jacket to inconel whose allowable stress ($3S_m$) is 87 kgf/mm^2 .

4.6 Analysis of Electromagnetic Force during Disruption

The antenna system is required to withstand plasma current disruptions at 22MA ($dI_p/dt = 1 \text{ MA/msec}$) on ITER. Analyses of electromagnetic force and resultant stress during disruption are made for the Faraday shields, the loop antenna element, the ridged waveguide and the launcher jacket.

Models for analyses of eddy current, electromagnetic force and stress for each component are shown in Figs 4-27 (a)~(e). Each component forms a loop and the eddy

current is calculated from an equivalent circuit equation. The maximum value of the eddy current, i_{\max} , is obtained by

$$i_{\max} = \frac{B \cdot S}{R(\tau_{\text{ex}} - \tau_c)} \left\{ \exp\left(-\frac{t_m}{\tau_{\text{ex}}}\right) - \exp\left(-\frac{t_m}{\tau_c}\right) \right\}, \quad (4-10)$$

where B is interlinkaging magnetic flux density, S interlinkaging area, R resistance of the loop, τ_{ex} decay time of the plasma current, τ_c time constant of the loop. t_m is a time when the eddy current reaches the maximum value and given by

$$t_m = \frac{\ln\left(\frac{1}{\tau_c}\right) - \ln\left(\frac{1}{\tau_{\text{ex}}}\right)}{\frac{1}{\tau_c} - \frac{1}{\tau_{\text{ex}}}}. \quad (4-11)$$

Each component of the magnetic field at the antenna position used in the calculation is as follows, $B_t = 3.5$ T, $B_p = 2.6$ T and $B_n = 0.5$ T, where B_n is a radial component of the magnetic field. The Faraday shield is made of inconel 625 and the other components are made of stainless steel. Allowable stresses ($1.5 S_m$) are 43.5 kgf/mm^2 for inconel and 20.3 kgf/mm^2 for stainless steel. Results of the stress analyses are summarized in the Table 4-2. All the values of the stress indicated in Table 4-2 are smaller than the allowable limit of each material with adequate design of each component. Following points have been found to be important for each component to withstand the electromagnetic force during disruptions.

(1) Faraday shield

As the toroidal length of the Faraday shield is relatively long ($\sim 1\text{m}$) in the present design, thickness of the Faraday shield is important to tolerate the electromagnetic force with B_p . Thickness of the inconel pipe of 35 mm is necessary.

(2) Loop antenna element

It is found that the loop antenna element cannot withstand the disruption force if the current strap is short-circuited on a common ground plate (toroidal septum). Therefore, we should assume separate short circuit plate. Thickness of the current strap of 35 mm is necessary.

(3) Ridged waveguide

We assume that only top plate of the T-shaped ridge deforms. In order to secure space inside the waveguide as much as possible, tapered cross-section of the top plate whose

stress is constant in the direction of the taper, as indicated in Fig. 4-27, is favourable. Thickness $f(x)$ (mm) is given by

$$f(x) = \sqrt{24.5 \cdot x}, \quad (4-12)$$

where x (mm) is the distance from the edge of the top plate and the constant stress of 19.2 kgf/mm^2 is assumed.

(4) Launcher jacket

All the torques acting on each component are supported by the launcher jacket, which is eventually supported by brackets on the cryostat. In order for the jacket to tolerate all the torques, thickness of the jacket of 45 mm is necessary.

Table 4-1 Cutoff frequency (MHz) of ridged waveguide
 $W=228$, $H=456$, $T_1=T_2=T_3=20$ (mm)

P1(mm)	P2(mm)	P3(mm)			
		0	100	205	296
10	10	57.90	49.68	44.81	41.53
12	12	61.42	54.25	49.20	46.24
10	12	59.08	52.03	47.29	44.22
8	12	55.95	48.49	45.21	42.38

Table 4-2 Results of electromagnetic force and stress analyses
 for antenna components during plasma current disruption.

Antenna component	Electromagnetic force	Moment/Torque	Stress
Faraday shield	2050 kgf/m with B_t by \dot{B}_p	1.2×10^4 kgf·mm	4.0 kgf/mm ²
	1530 kgf/m with B_p by \dot{B}_p	1.35×10^5 kgf·mm	35.7 kgf/mm ²
Loop antenna element			
Feeder ¹	2.7×10^3 kgf with B_t by \dot{B}_p	4.4×10^5 kgf·mm	14.6 kgf/mm ²
Current strap ²	6.1×10^3 kgf with B_t by \dot{B}_n	9.8×10^5 kgf·mm	17.4 kgf/mm ²
Short circuit plate ³	2.65×10^3 kgf with B_t by \dot{B}_p	4.2×10^5 kgf·mm	6.5 kgf/mm ²
Ridged waveguide			
Frame	2.6 ton with B_t by \dot{B}_n		0.26 kgf/mm ²
Top and bottom plates	118 ton with B_t by \dot{B}_p	5.64×10^4 ton·mm	
T-shaped ridge	157 ton with B_t by \dot{B}_p	3.20×10^4 ton·mm	19.2 kgf/mm ²
Launcher jacket			
Frame	1520 ton with B_t by \dot{B}_p	1.73×10^6 ton·mm	7.27 kgf/mm ²
	206 ton with B_t by \dot{B}_n		2.58 kgf/mm ²
Top and bottom plates	1320 ton with B_t by \dot{B}_p	1.50×10^6 ton·mm	
Top and bottom plates of ridged waveguide (total)		1.13×10^6 ton·mm	
T-shaped ridge (total)		6.39×10^5 ton·mm	
Toroidal sepum (total)		1.68×10^5 ton·mm	
		5.17×10^6 ton·mm (total by \dot{B}_p)	19.5 kgf/mm ² (total by \dot{B}_p)

¹ 22 cm (l), 16 cm (w), 2.5 cm (t)

² 48 cm (l), 16 cm (w), 3.5 cm (t)

³ 22 cm (l), 16 cm (w), 3.8 cm (t)

— 56 —

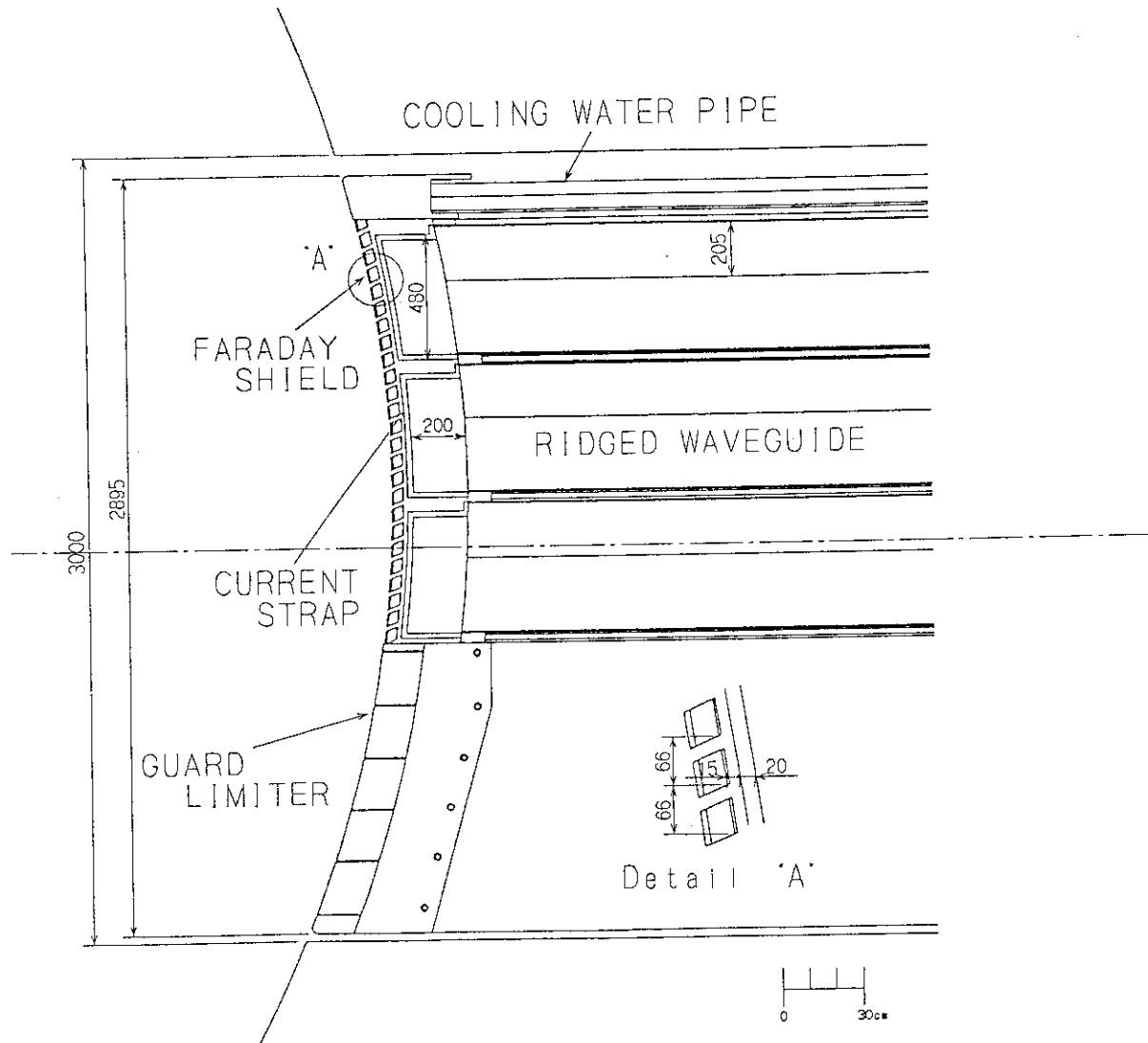


Fig. 4-2 Side view of the FER IC launcher

ELECTRON DENSITY PROFILE AND ANTENNA POSITION

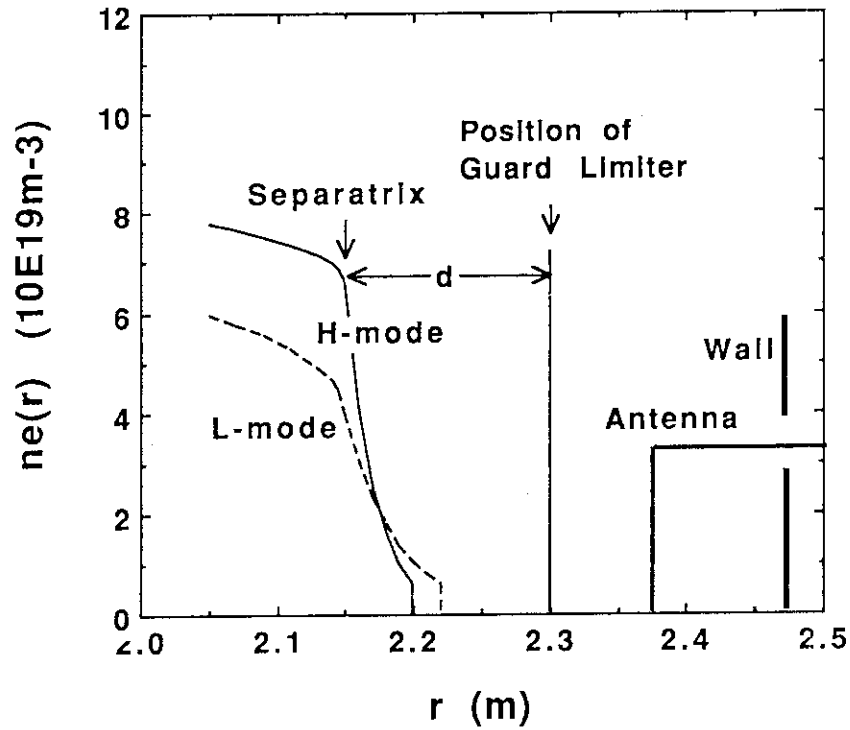


Fig. 4-3 Model for the antenna-plasma coupling calculation

5x4 Array, $L_a=0.48\text{m}$, $W_a=0.16\text{m}$
 $d=0.15\text{m}$, $N(p)=1$

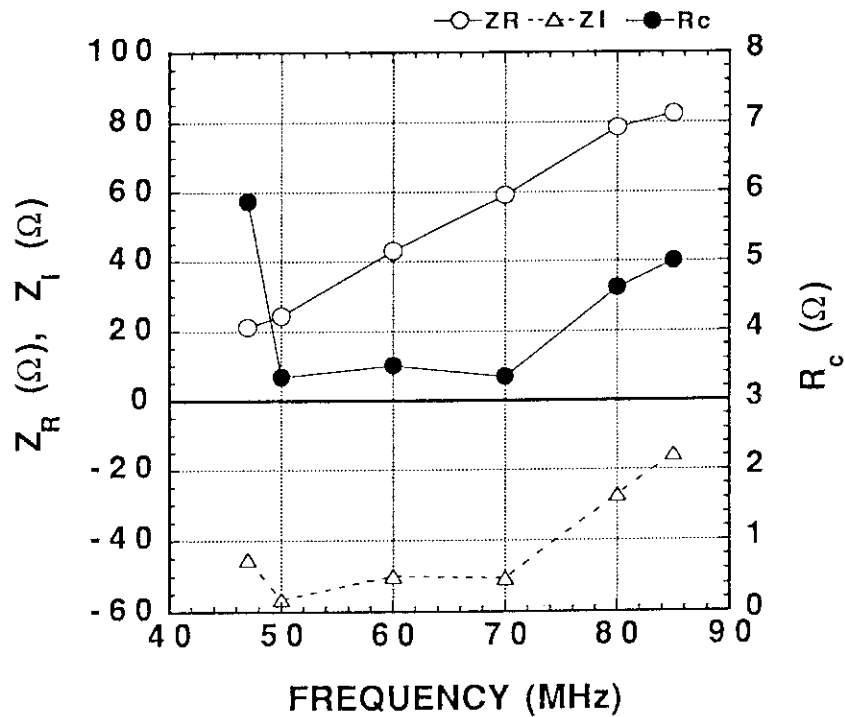
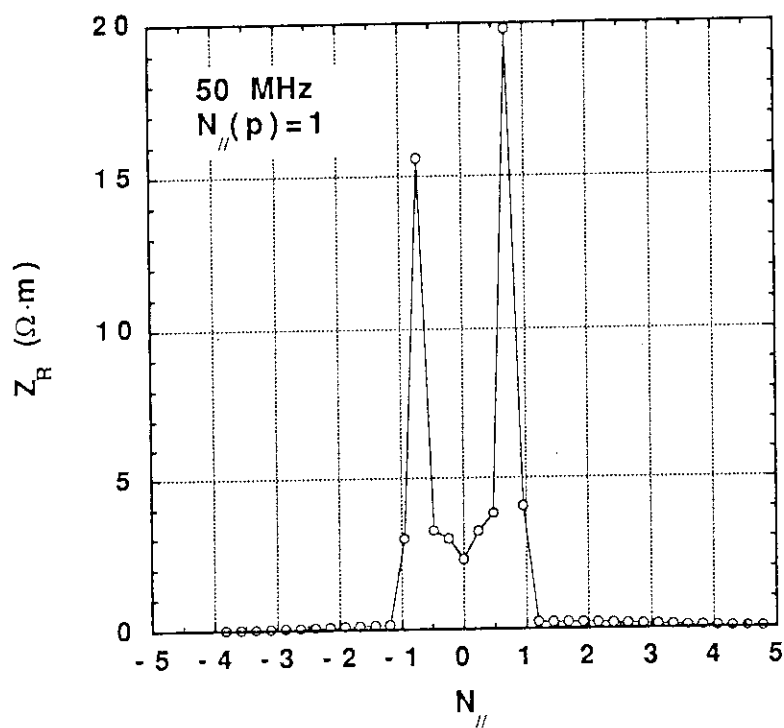


Fig. 4-4 Real and imaginary parts of the antenna radiation impedance, Z_R and Z_I , and antenna coupling resistance, R_c , evaluated with the characteristic impedance of the ridged waveguide, for the 5x4 array against frequency.

(a)

5x4 Array, $L_a=0.48\text{m}$, $W_a=0.16\text{m}$
 $d=0.15\text{m}$



(b)

5x4 Array, $L_a=0.48\text{m}$, $W_a=0.16\text{m}$
 $d=0.15\text{m}$

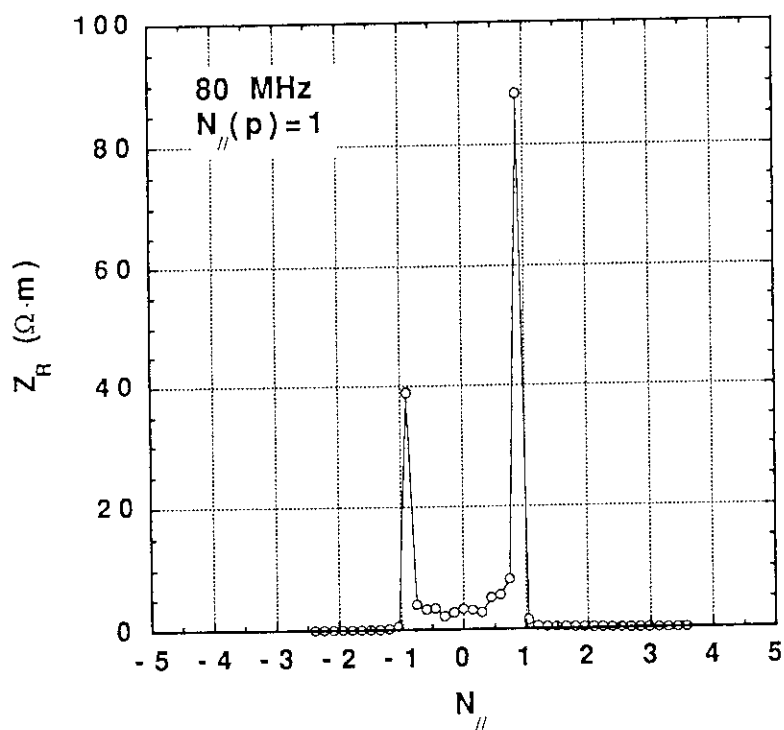


Fig. 4-5 Antenna radiated power spectra of the 5x4 array at
 (a) 50 MHz and (b) 80 MHz.

5x4 Array, $L_a=0.48\text{m}$, $W_a=0.16\text{m}$
 $N_{\parallel}(p)=1$

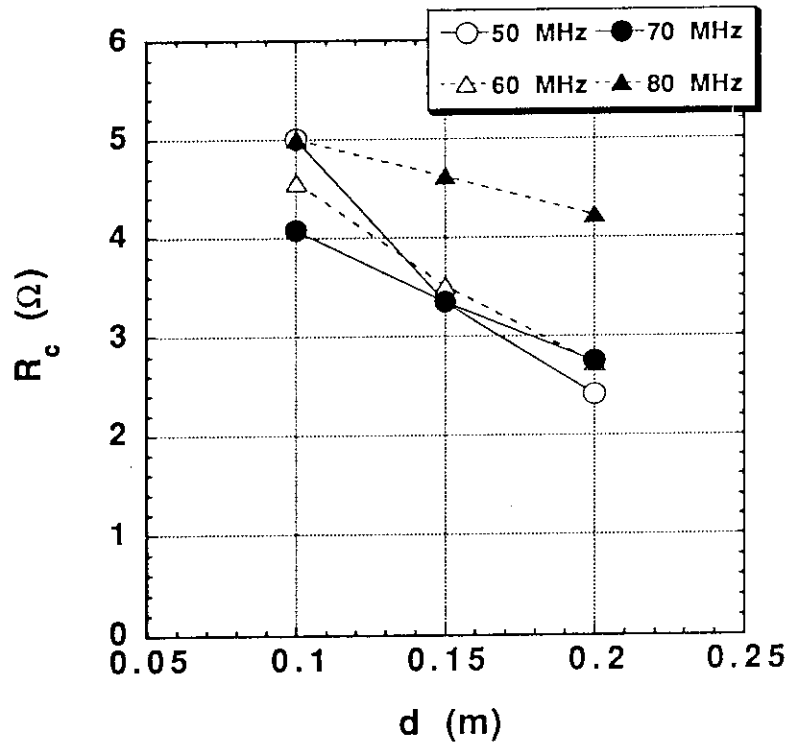


Fig. 4-6 Dependence of R_c on the antenna-plasma distance, d , at various frequencies.

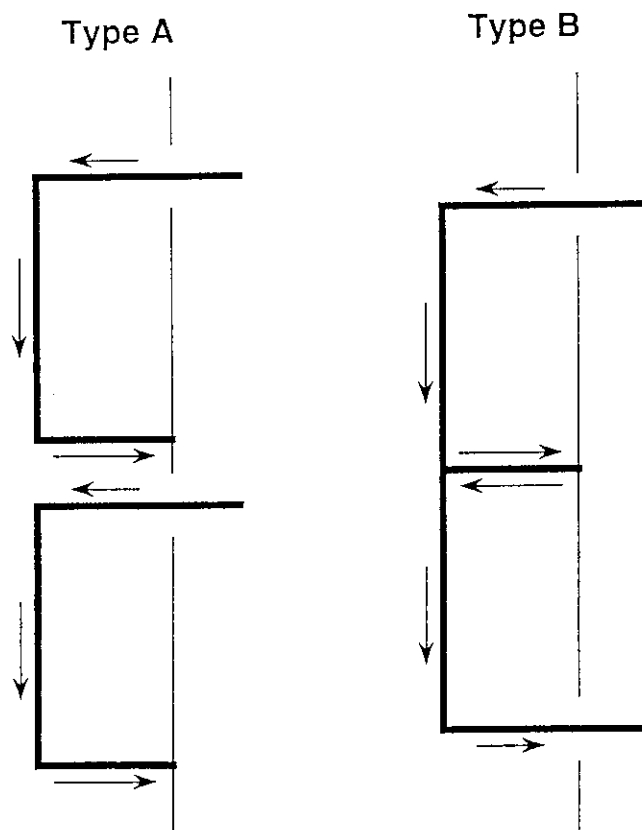


Fig. 4-7 Comparison of two antenna configurations in the poloidal direction.

4x4 Array, $L_a=0.48\text{m}$, $W_a=0.16\text{m}$
 $d=0.15\text{m}$, $N_{\parallel}(p)=1$

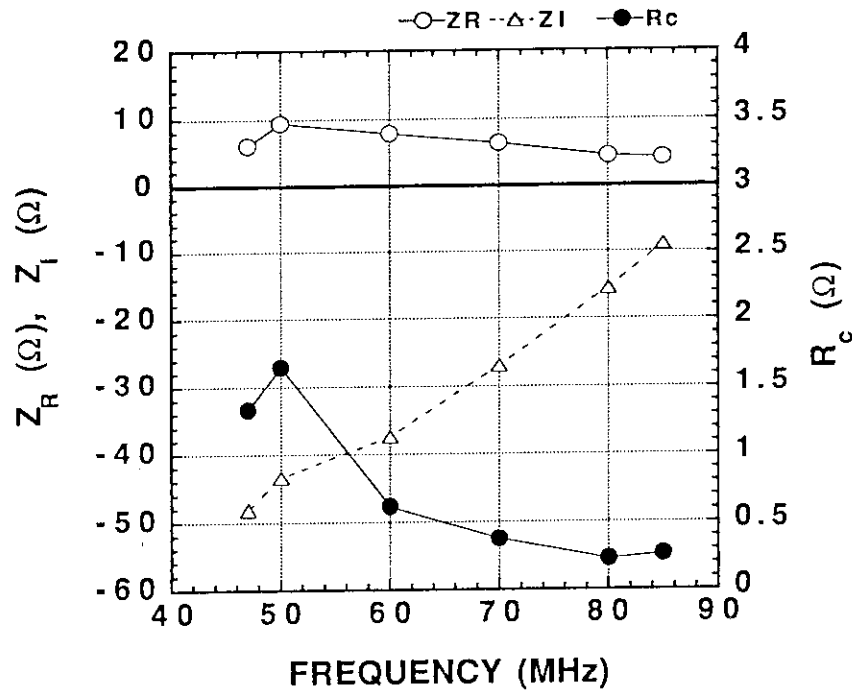


Fig. 4-8 Real and imaginary parts of the antenna radiation impedance, Z_R and Z_I , and antenna coupling resistance, R_c , evaluated with the characteristic impedance of the ridged waveguide, for the 4x4 array against frequency.

5x4 Array, $L_a=0.48\text{m}$, $W_a=0.16\text{m}$
 $d=0.15\text{m}$, $N_{\parallel}(p)=1$

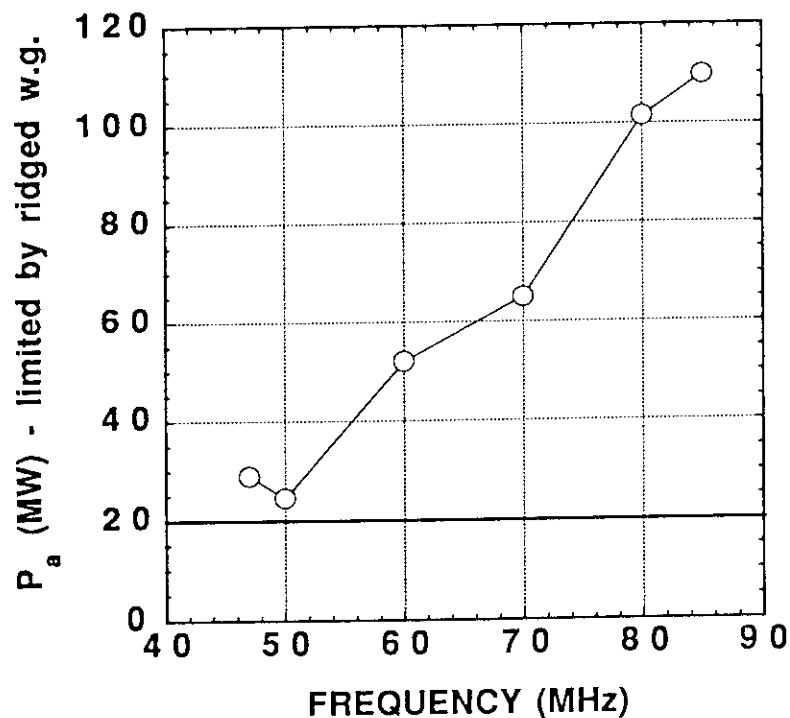
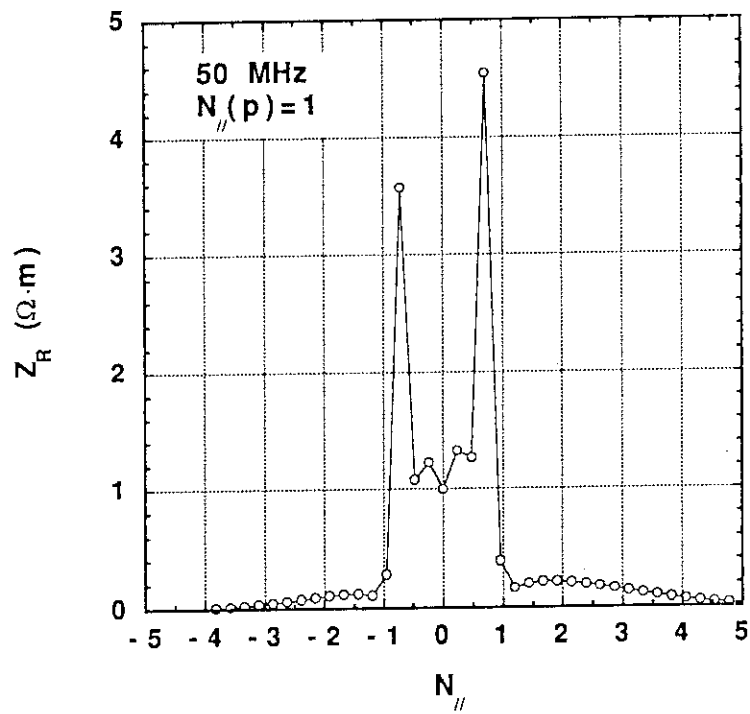


Fig. 4-10 Injection power capability of the 5x4 array antenna limited by the ridged waveguide part as a function of frequency

(a)

4x4 Array, $L_a=0.48\text{m}$, $W_a=0.16\text{m}$
 $d=0.15\text{m}$



(b)

4x4 Array, $L_a=0.48\text{m}$, $W_a=0.16\text{m}$
 $d=0.15\text{m}$

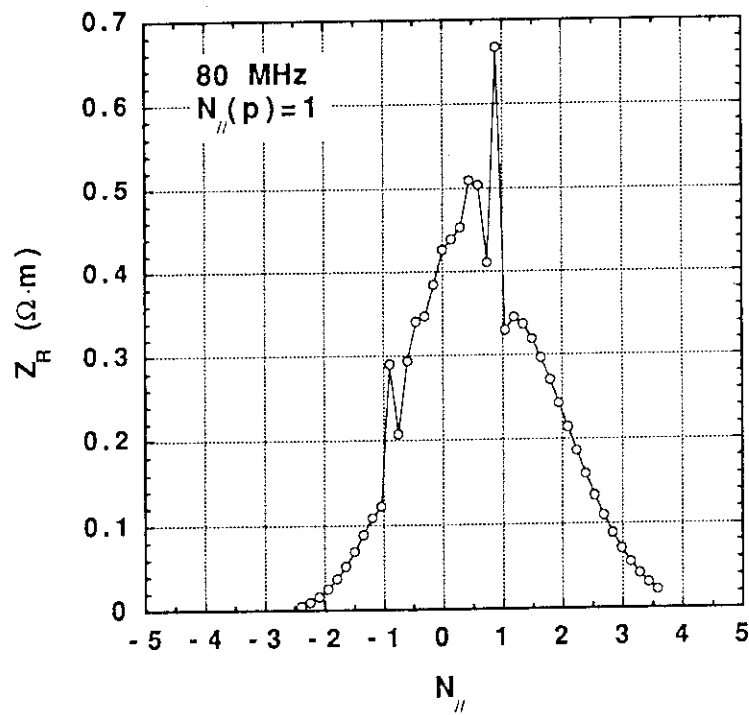
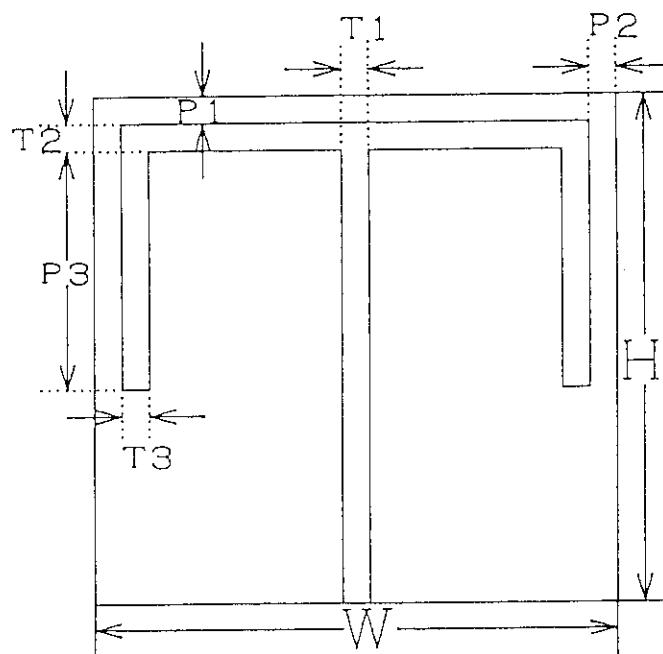
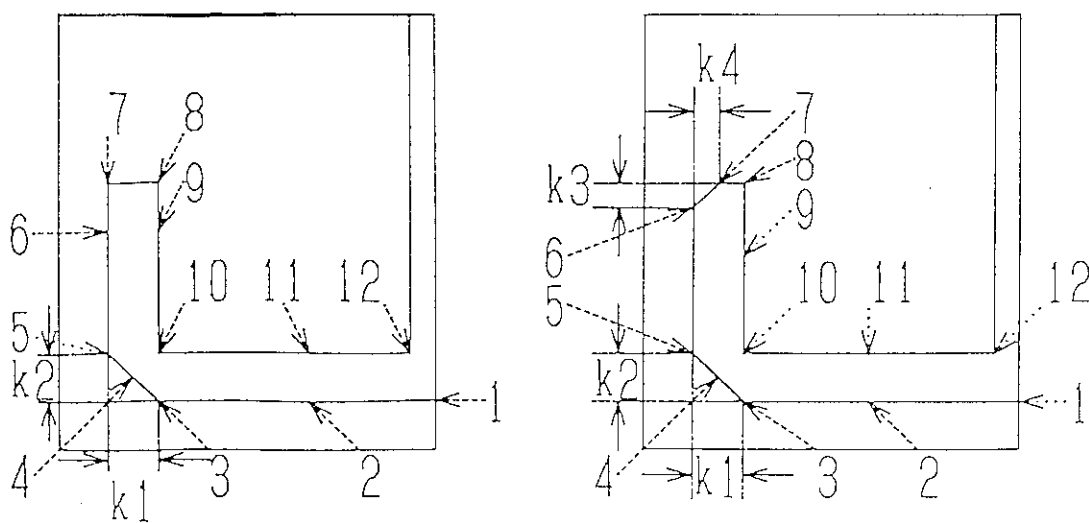


Fig. 4-9 Antenna radiated power spectra of the 4x4 array at
 (a) 50 MHz and (b) 80 MHz.



(a) waveguide parameters



(b) points for electric field distribution

Fig. 4-11 T-shaped ridged waveguide with arms

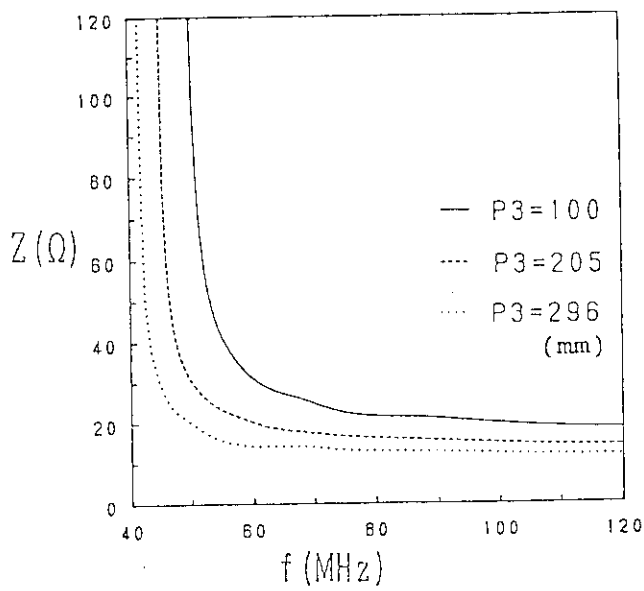
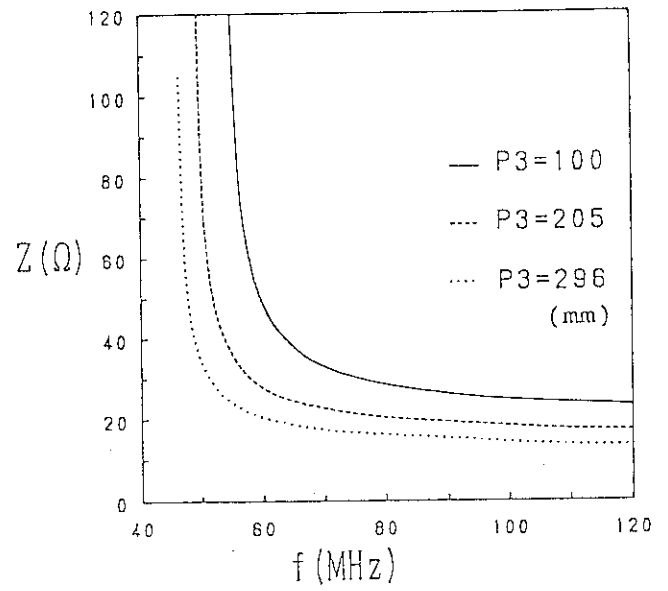
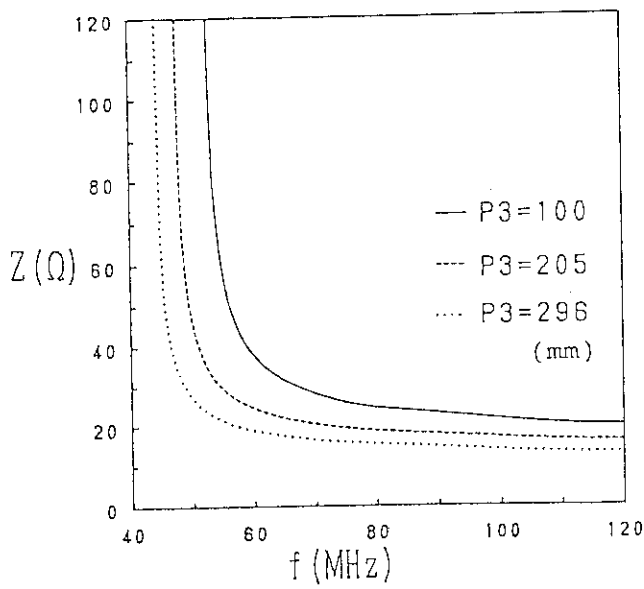
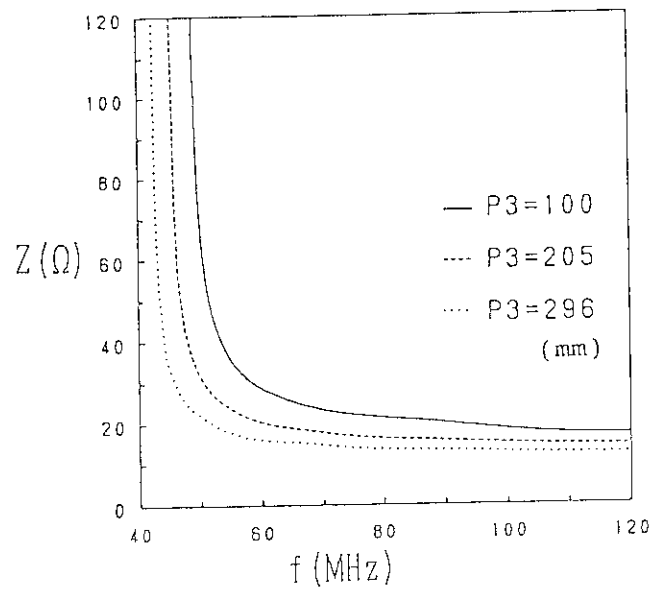
(a) $P1=P2=10$ (mm)(b) $P1=P2=12$ (mm)(c) $P1=10$, $P2=12$ (mm)(d) $P1=8$, $P2=12$ (mm)

Fig. 4-12 Waveguide impedance of ridged waveguide
 $W=228$, $H=456$, $T1=T2=T3=20$ (mm)

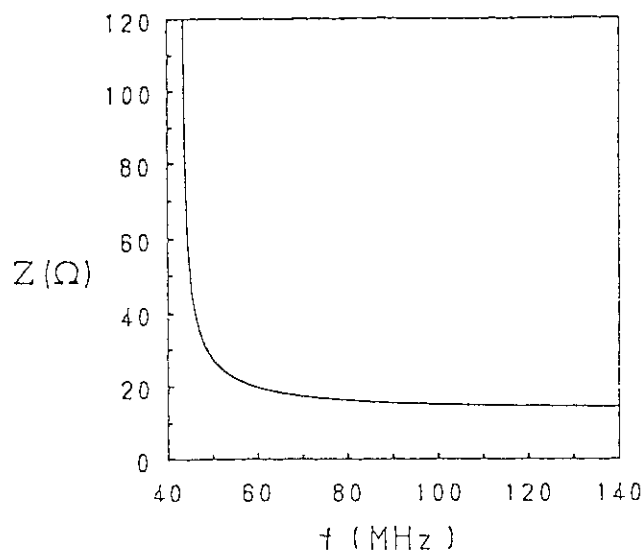


Fig. 4-13 Waveguide impedance of the ridged waveguide for the FER IC antenna. $W=228$, $H=485$, $P_1=8$, $P_2=12$, $P_3=205$, $T_1=T_2=T_3=20$ (mm)

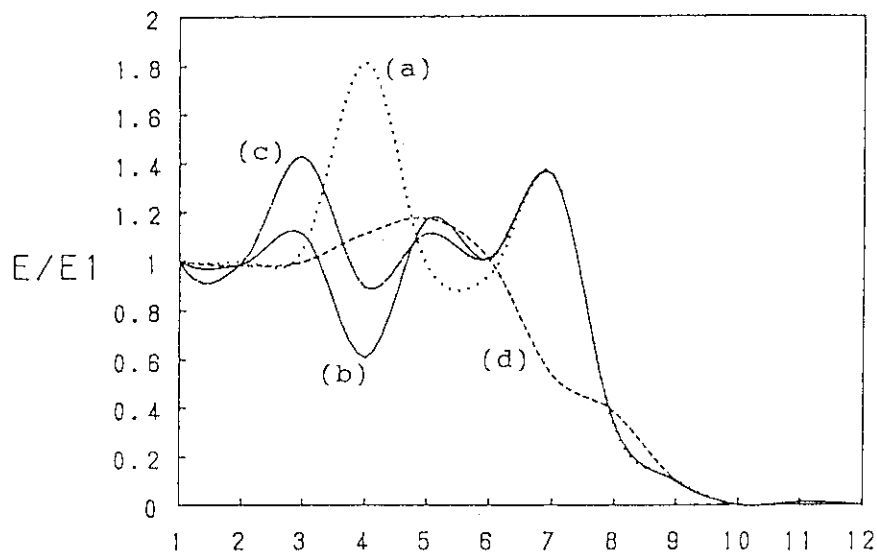


Fig. 4-14 Electric field distribution along the ridge of various cut edges. $W=228$, $H=485$, $P_1=P_2=12$, $P_3=50$, $T_1=T_2=T_3=20$ (mm)

(a) $k_1=k_2=0$,	$k_3=k_4=0$ (mm),	$f_c=55.277$ (MHz)
(b) $k_1=k_2=20$,	$k_3=k_4=0$ (mm),	$f_c=56.864$ (MHz)
(c) $k_1=k_2=10$,	$k_3=k_4=0$ (mm),	$f_c=54.973$ (MHz)
(d) $k_1=k_2=20$,	$k_3=k_4=10$ (mm),	$f_c=57.473$ (MHz)

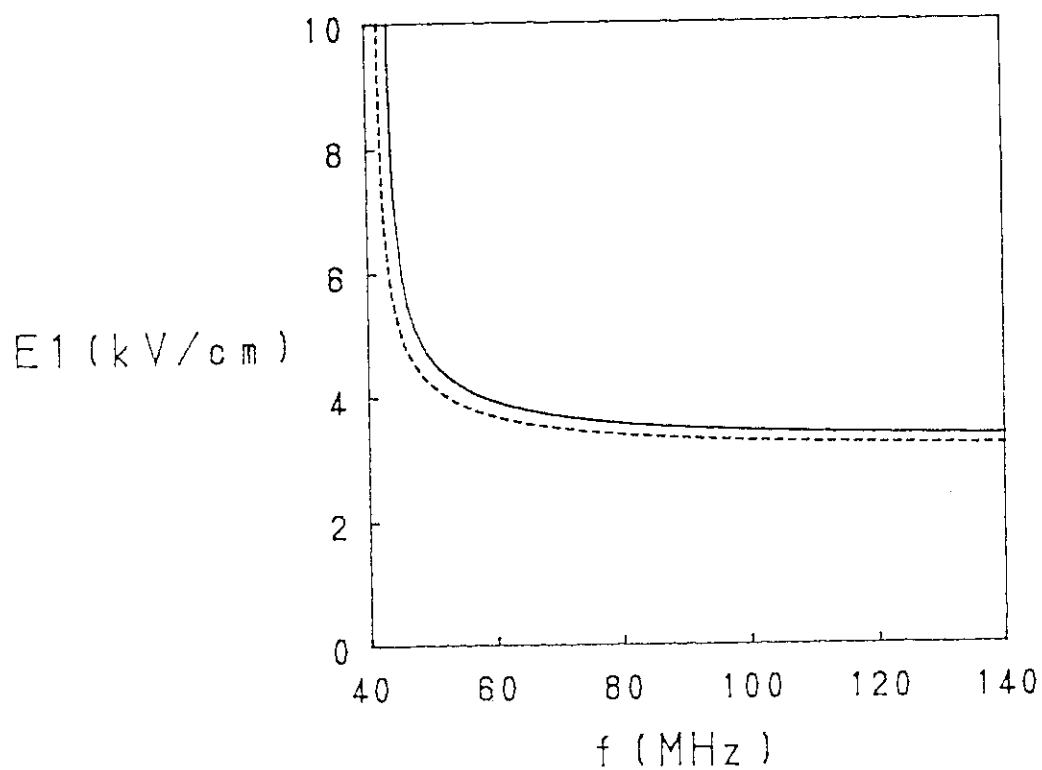
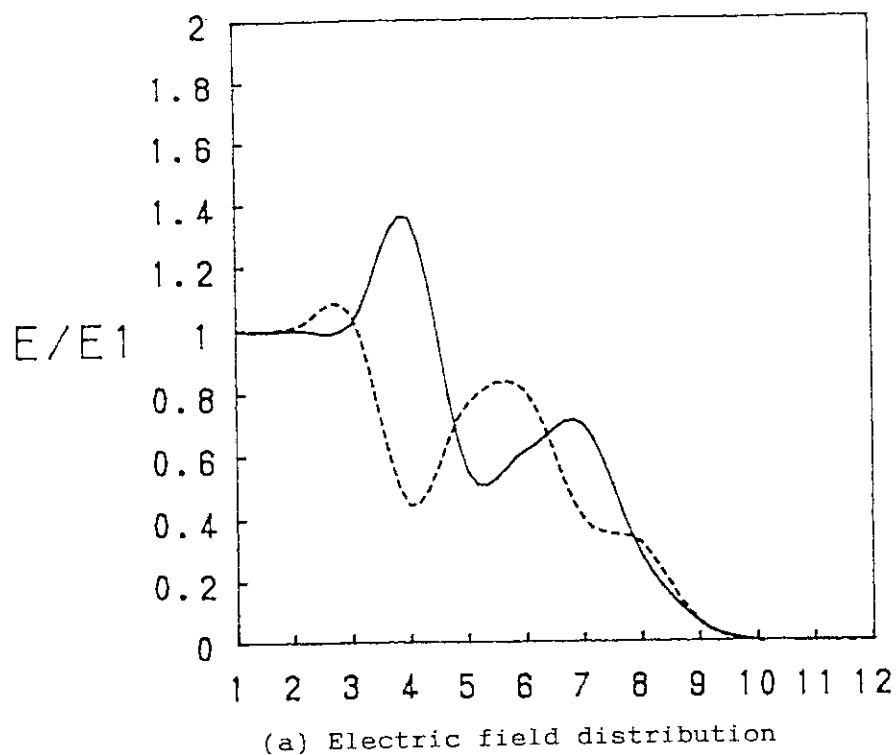


Fig. 4-15 (a) Electric field distribution along the ridge of the ridged waveguide for FER.

(b) Electric field strength at point 1 for 1 MW transmission

$W=228$, $H=485$, $P1=8$, $P2=12$, $P3=205$, $T1=T2=T3=20$ (mm)
 — $k1=k2=0$, $k3=k4=0$ (mm), $f_c=43.329$ (MHz)
 ---- $k1=k2=20$, $k3=k4=10$ (mm), $f_c=41.717$ (MHz)

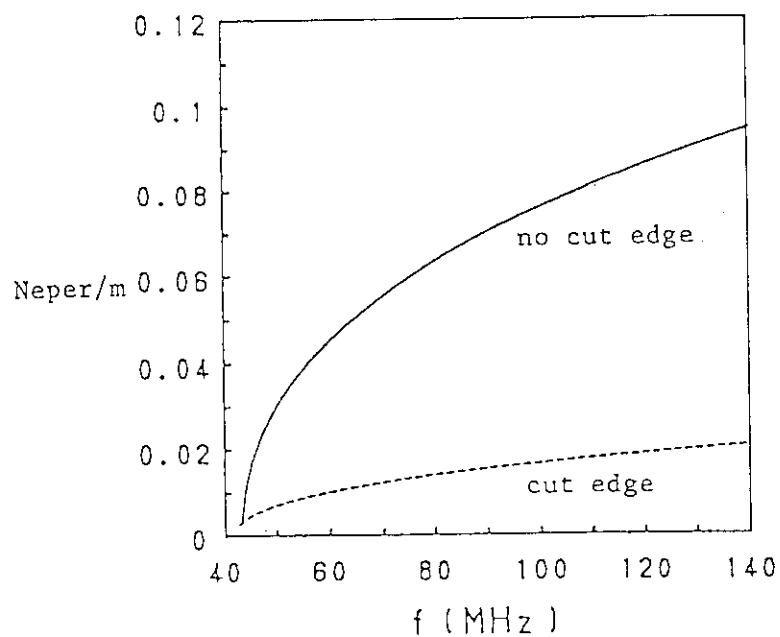


Fig. 4-16 Transmission loss of the ridged waveguide for FER.
W=228, H=485, P1=8, P2=12, T1=T2=T3=20(mm)

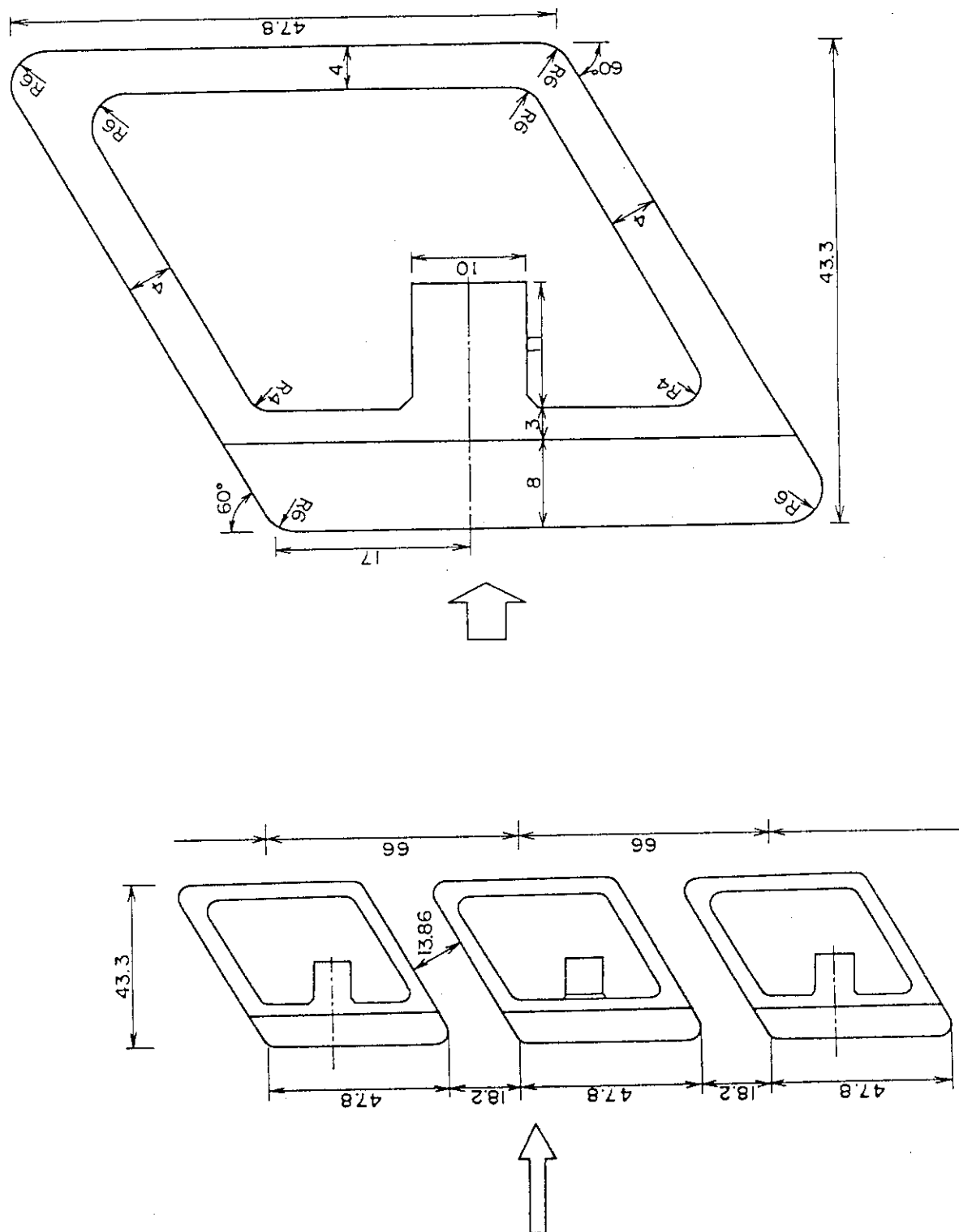


Fig. 4-17 Cross-section and detailed dimensions of the Faraday shield.

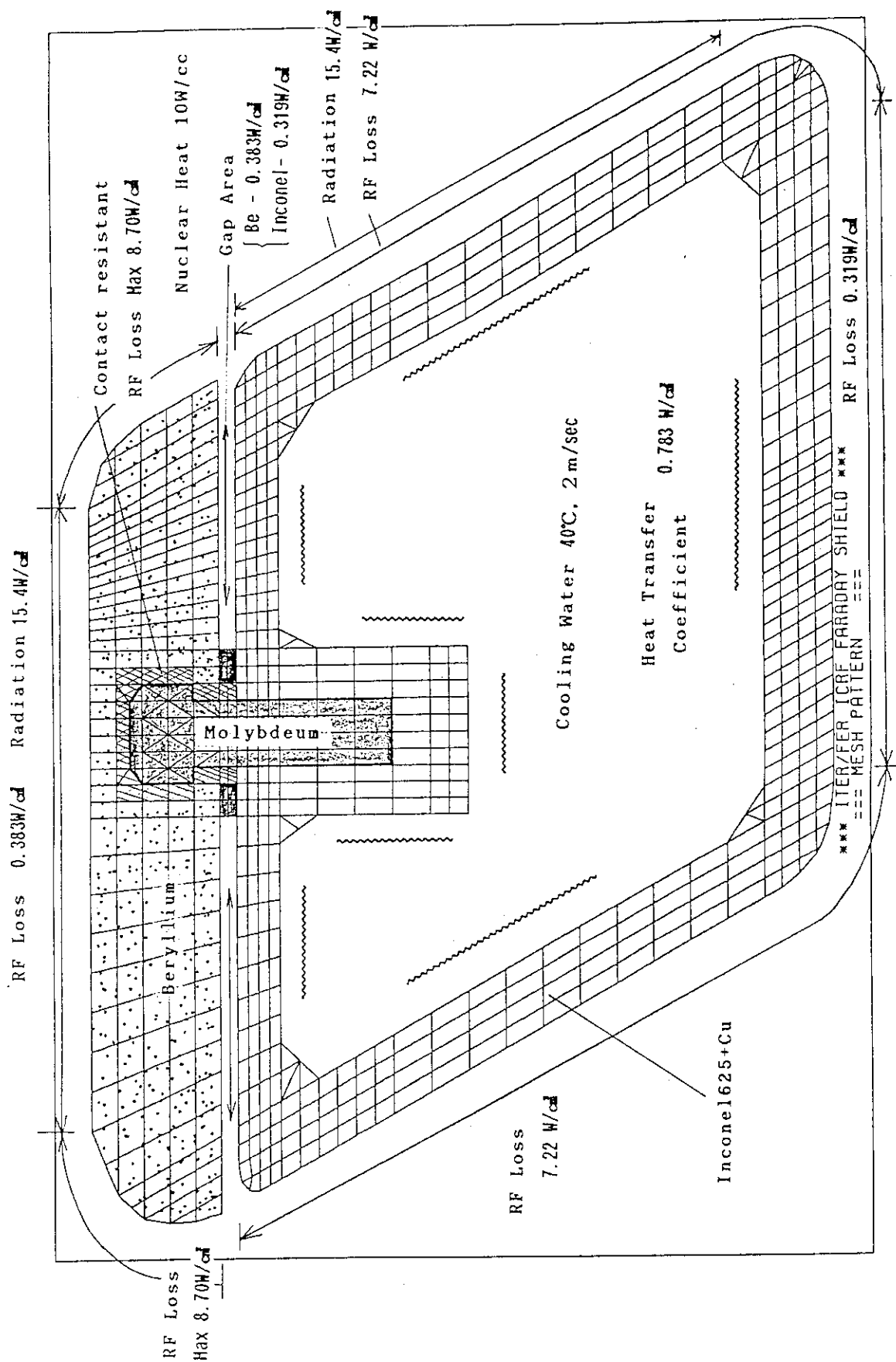


Fig. 4-18 Model for the thermal stress analysis of the Faraday shield.

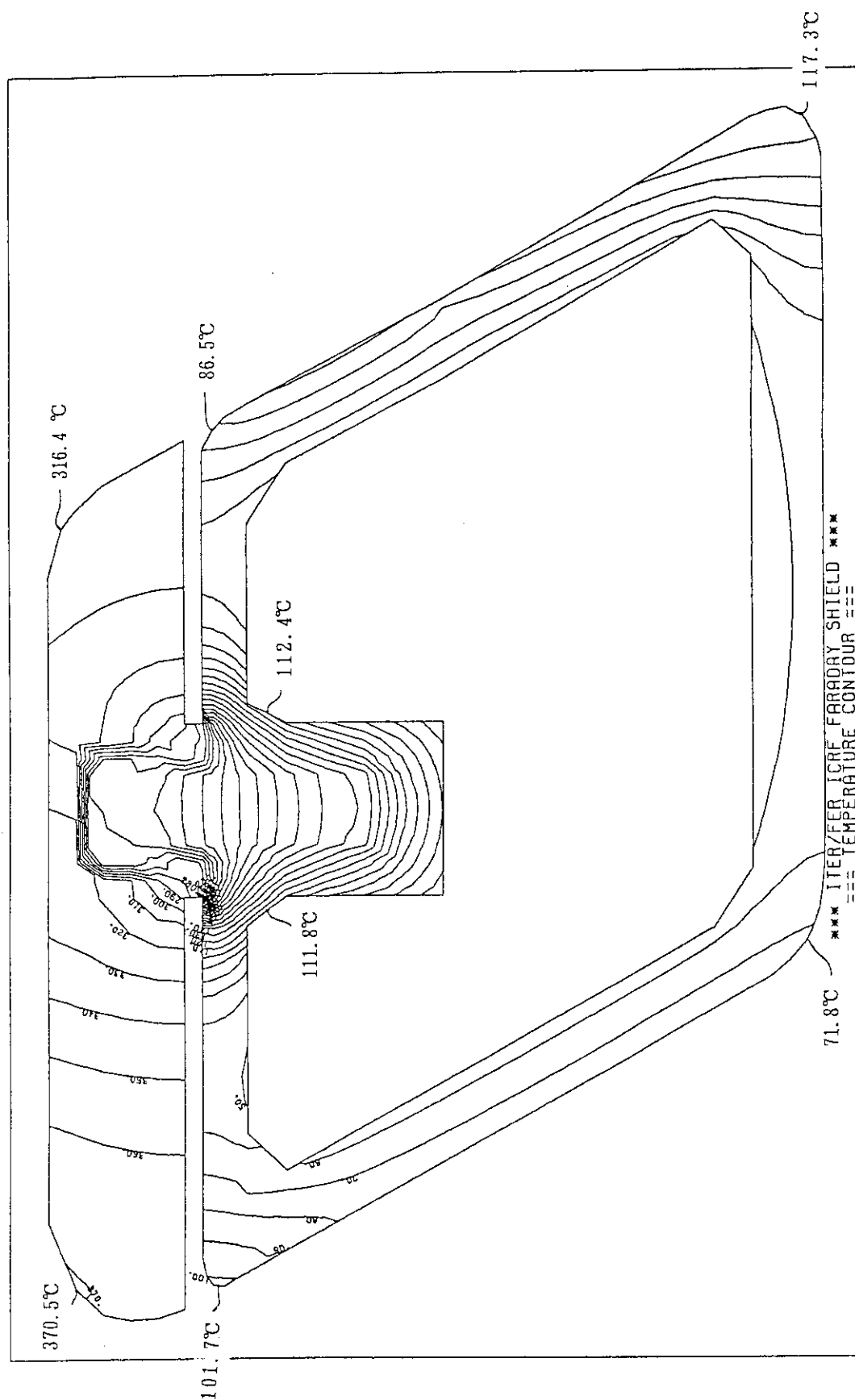


Fig. 4-19 Temperature Contour of the Faraday Shield with beryllium armor plate.

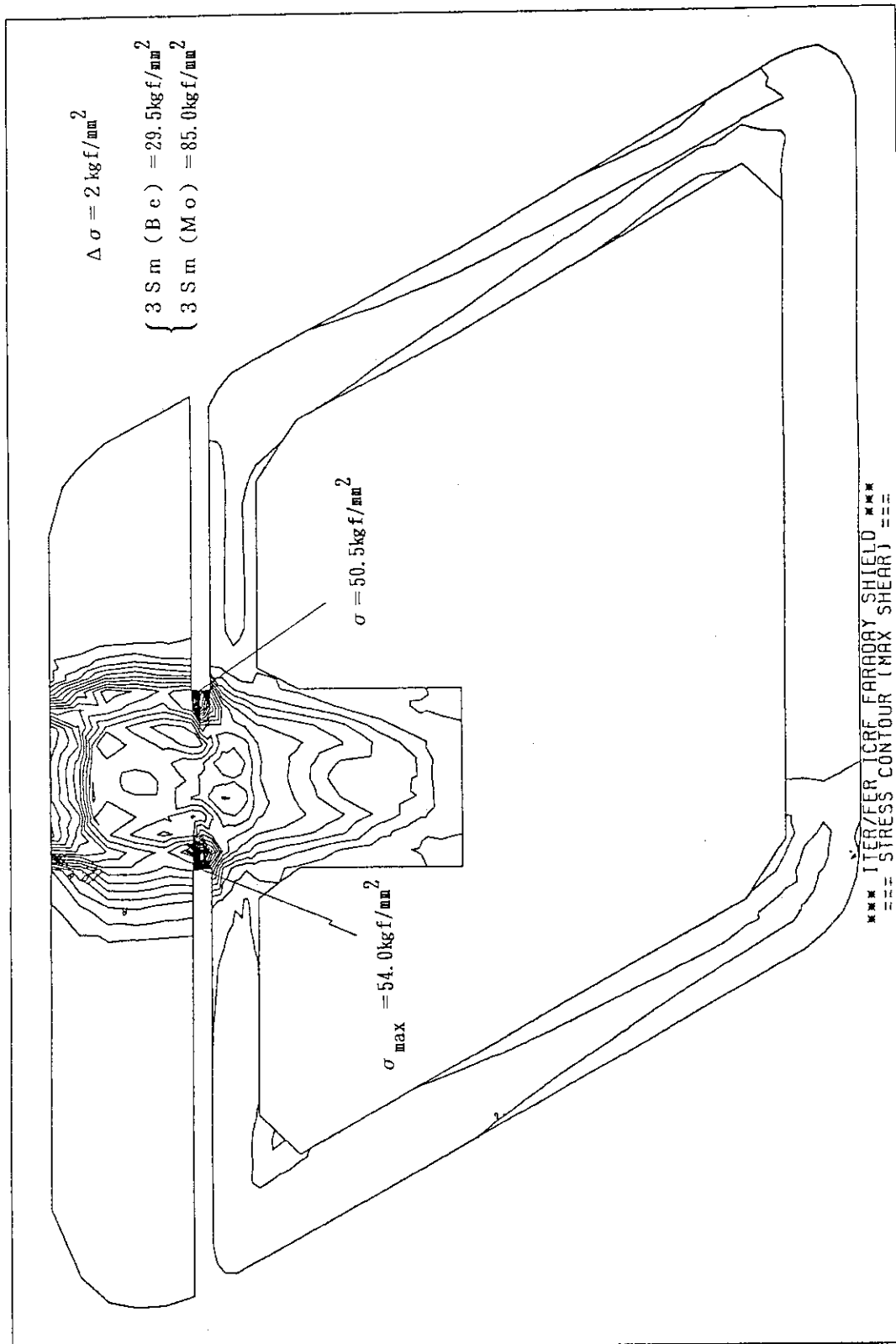


Fig. 4-20 Stress Contour of the Faraday Shield with beryllium armor plate.

Each line shows a step of $2 (\text{kgf/mm}^2)$.

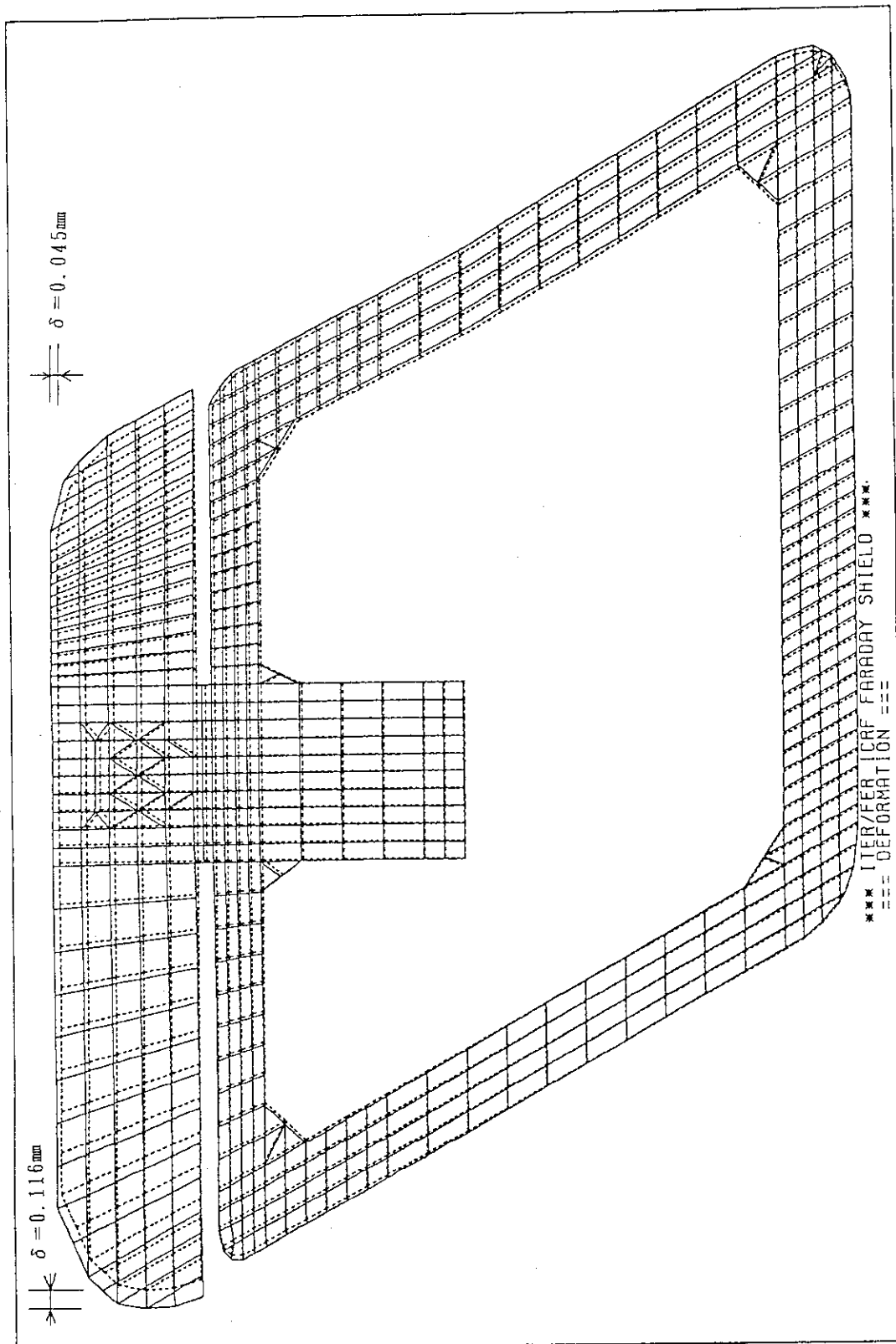


Fig. 4-21 Deformation of the Faraday Shield with beryllium armor plates.

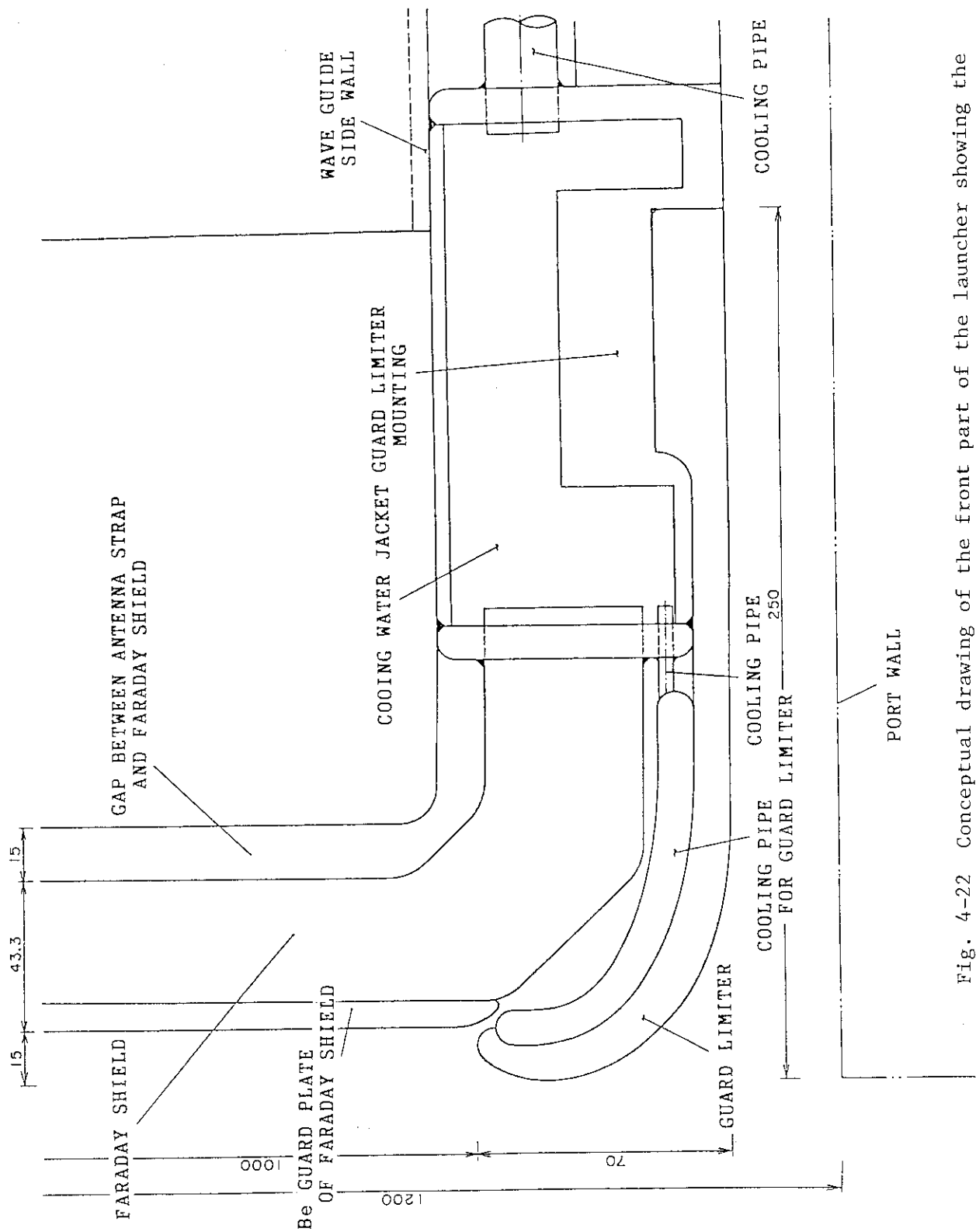


Fig. 4-22 Conceptual drawing of the front part of the launcher showing the guard limiter, the Faraday shield and the launcher jacket.

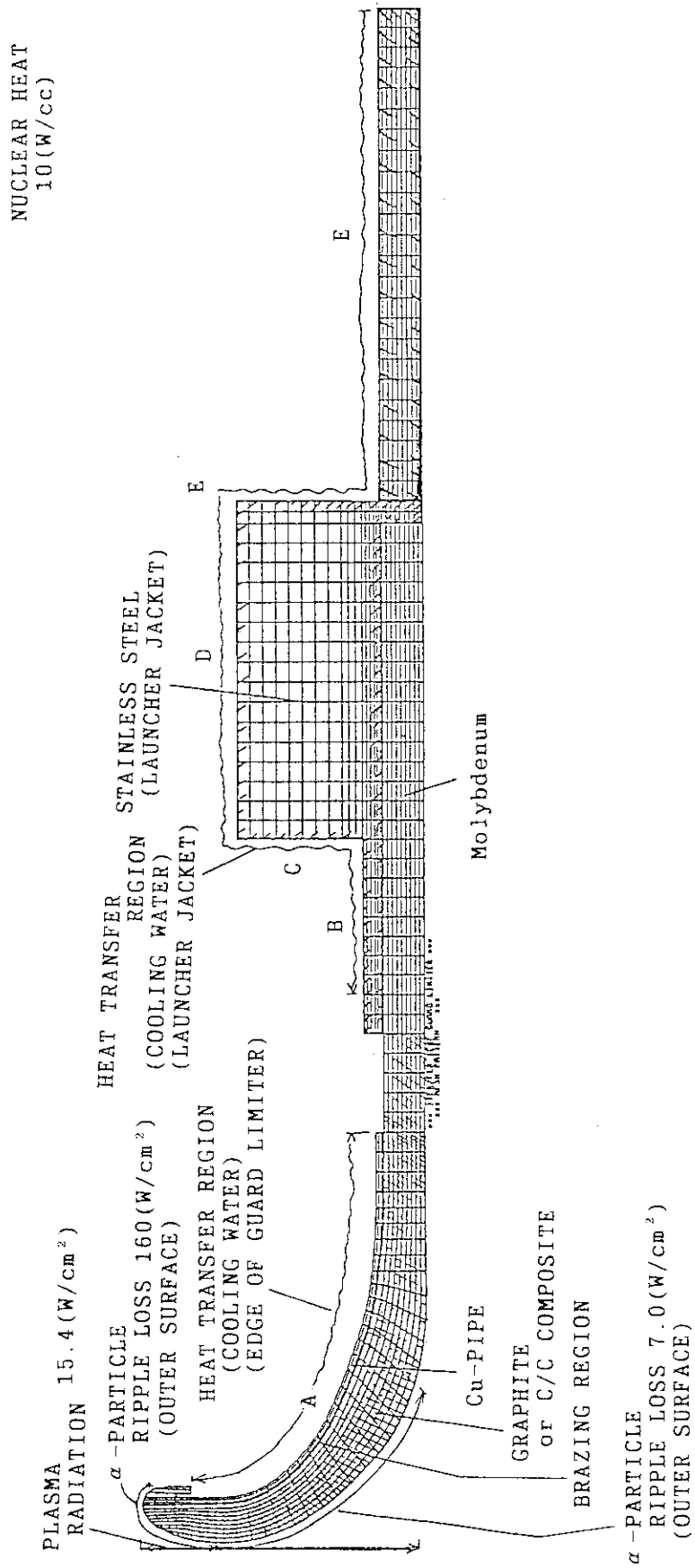


Fig. 4-23 Model for thermal analysis of the guard limiter

$T_{MAX} = 990.0\text{ }^{\circ}\text{C}$
 $\Delta T = 30\text{ }^{\circ}\text{C}$

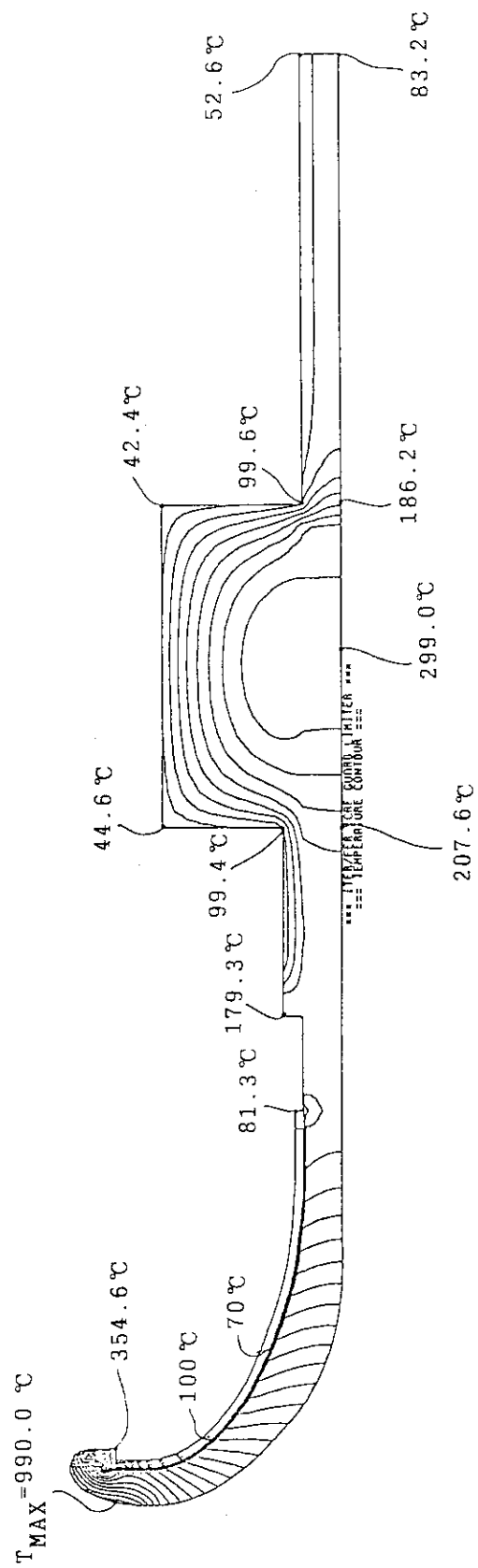


Fig. 4-24 Temperature contour of the guard limiter

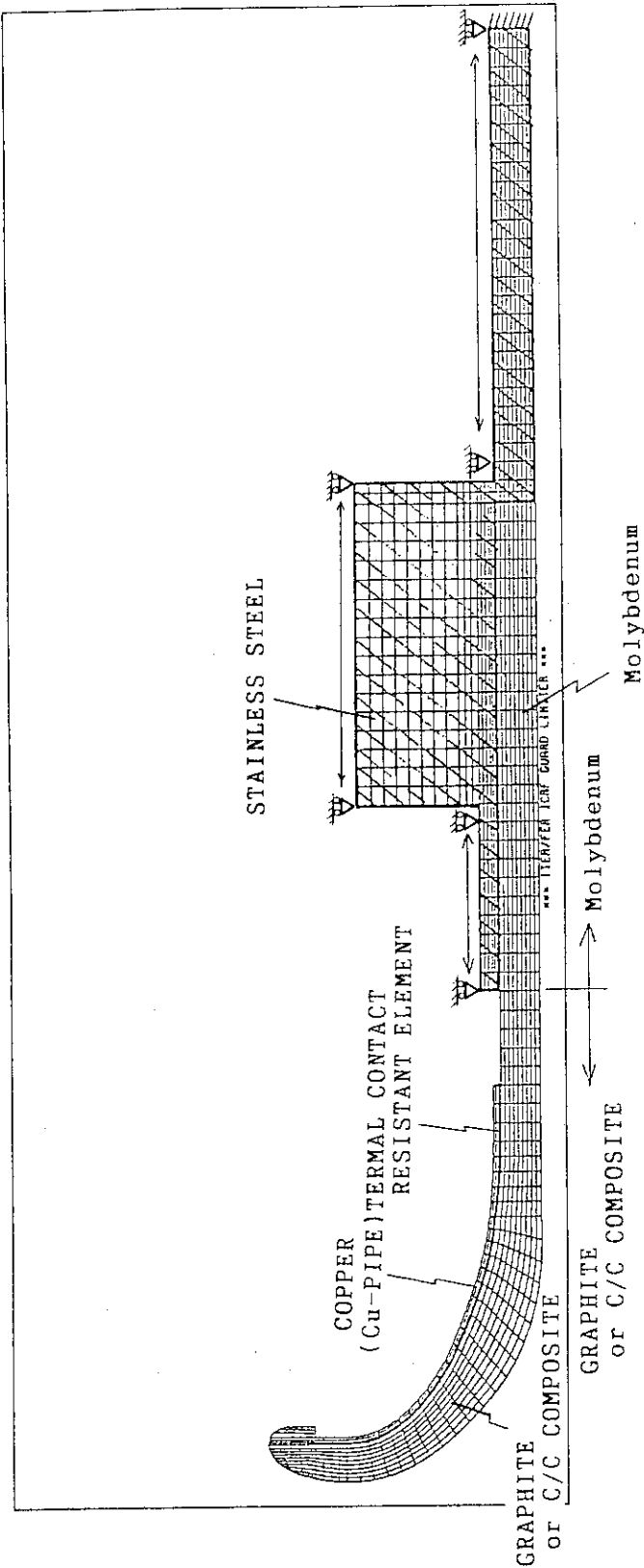


Fig. 4-25 Model for thermal stress analysis of the guard limiter.

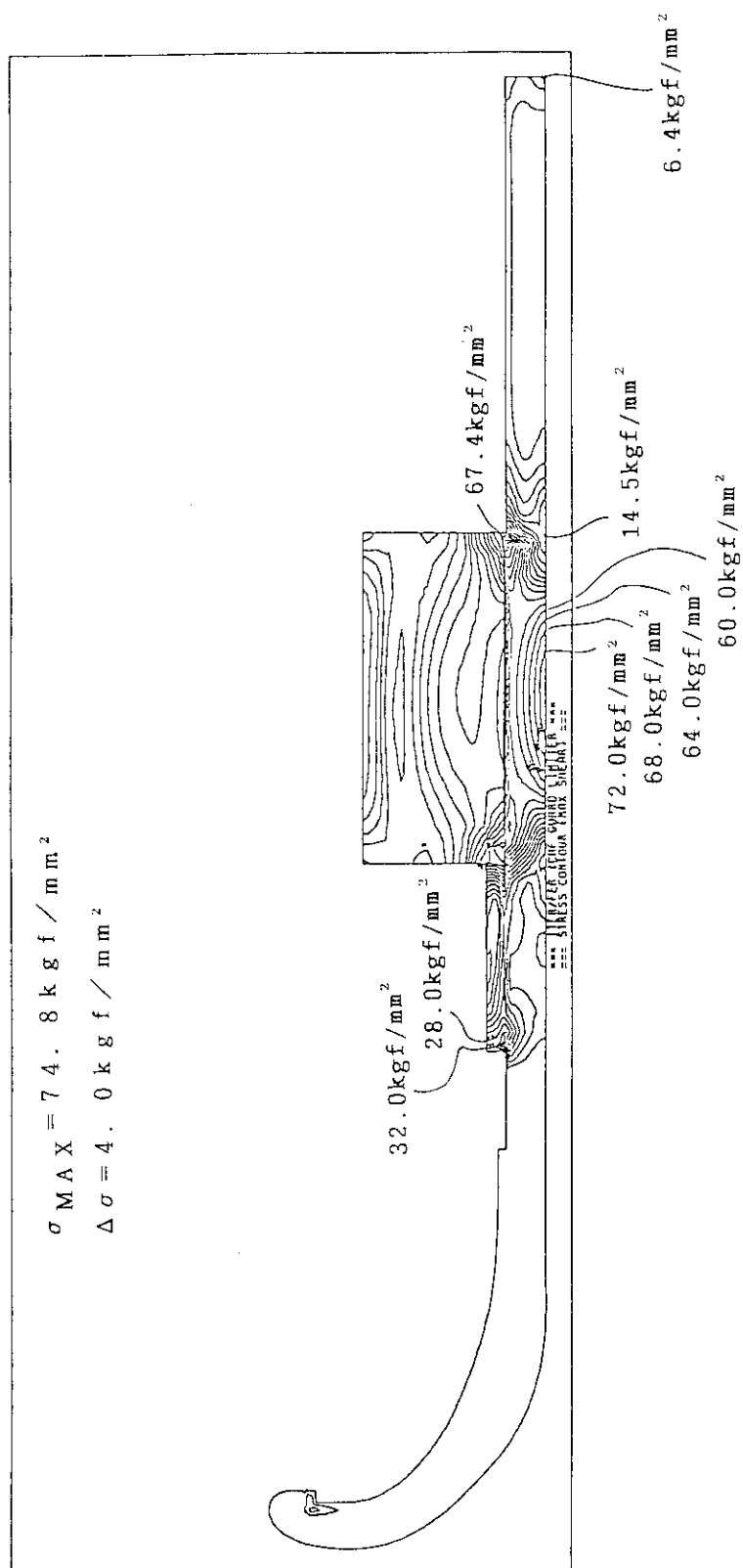


Fig. 4-26 Thermal stress contour of the guard limiter

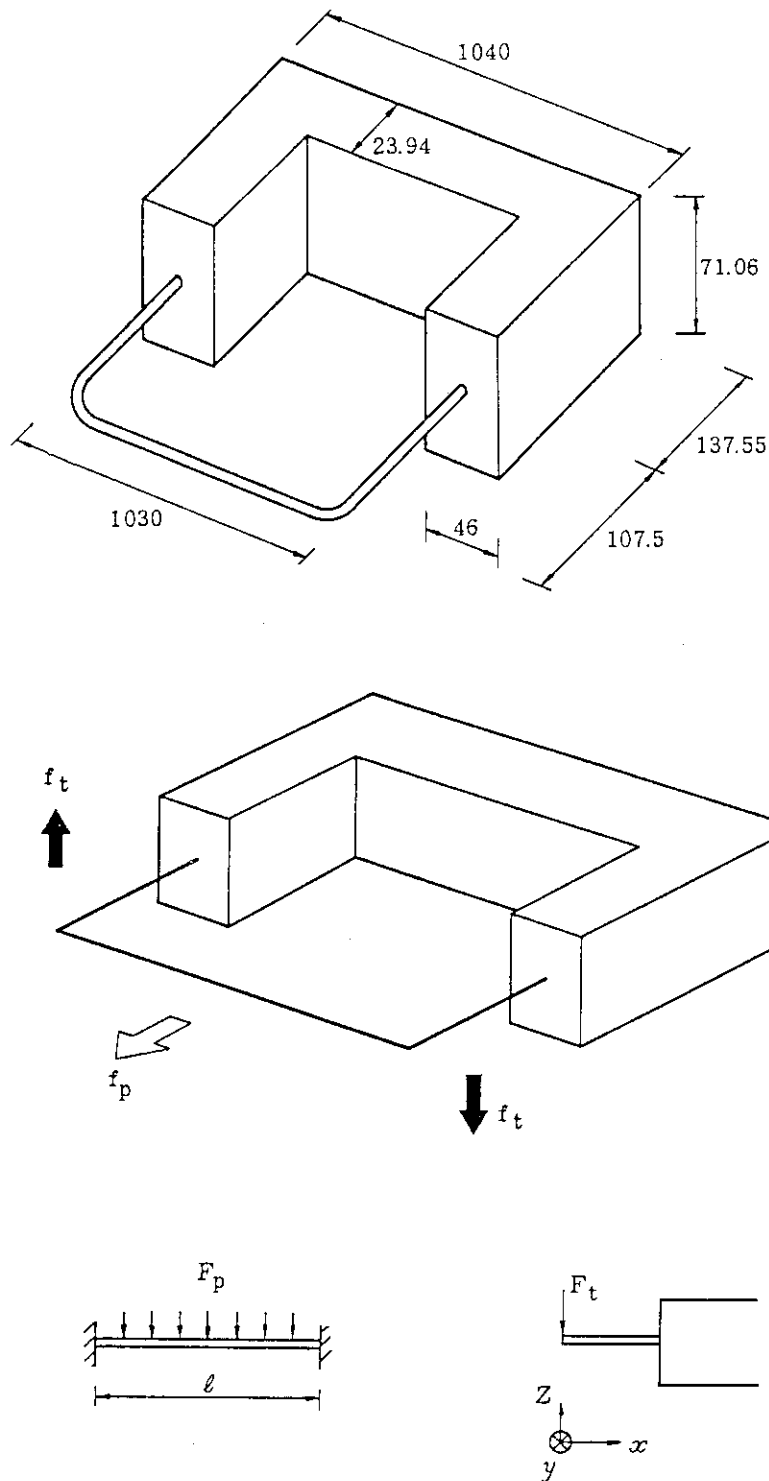


Fig. 4-27 Models for analyses of eddy current, electromagnetic force and stress on various structural components of the antenna system during plasma current disruption.

(a) Faraday shield

Current strap

Feeder & Short-circuit plate

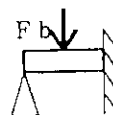
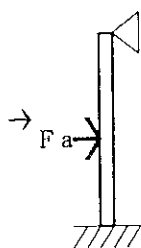
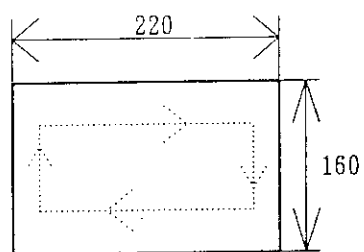
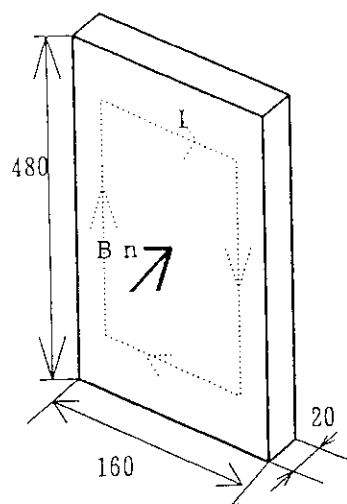
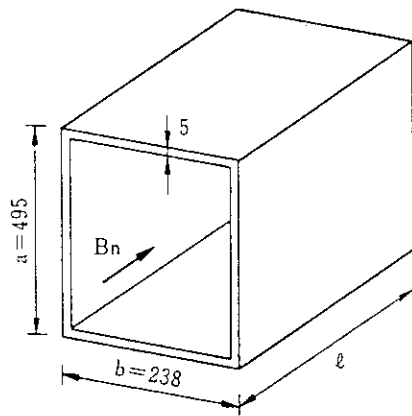


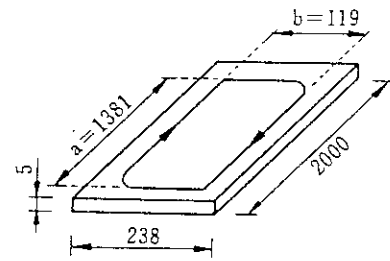
Fig. 4-27 (Continued)

(b) Loop antenna element

Frame



Top & bottom plates



T-shaped ridge

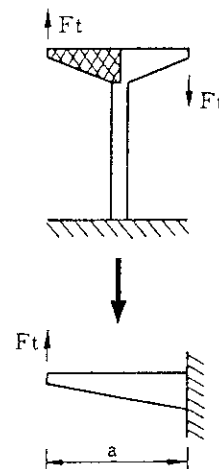
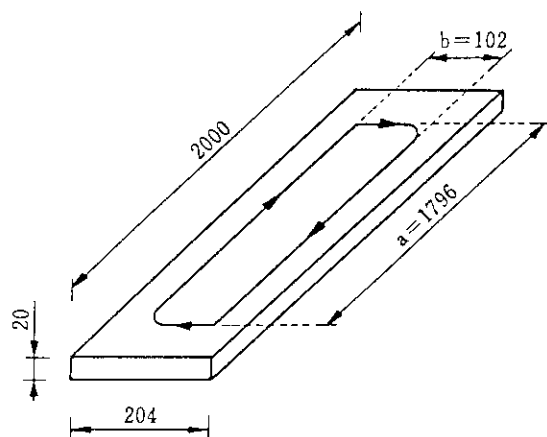
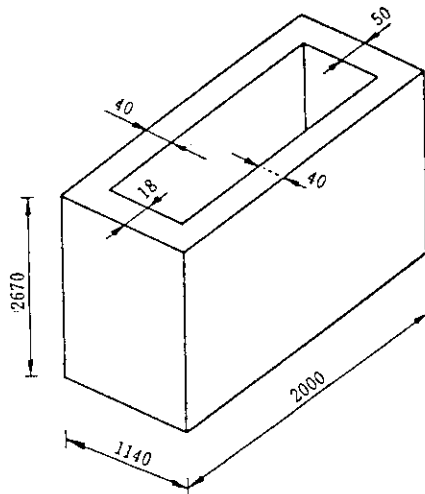
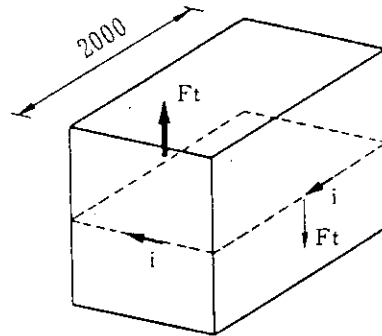


Fig. 4-27 (Continued)
(c) Ridged waveguide

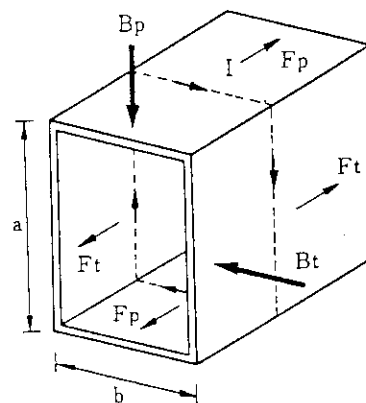
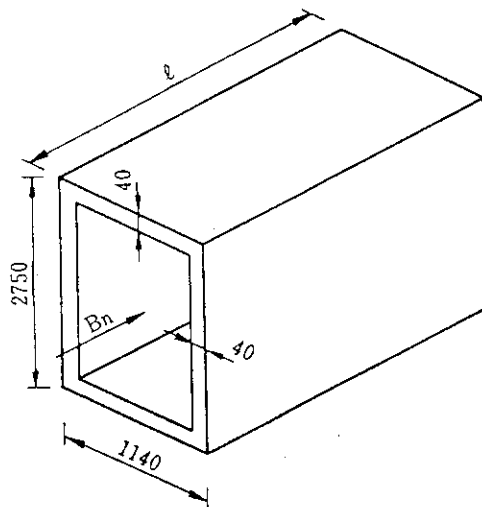
Frame



eddy current by dB_p/dt



eddy current by dB_n/dt



Top & bottom plates

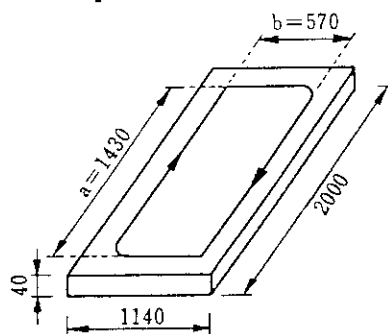


Fig. 4-27 (Continued)

(d) Launcher jacket

5. CONCLUSIONS, AND R&D NEEDS

5.1 Conclusions

Physics analysis and conceptual design study have been done for the FER IC system and the ITER high frequency IC system. The frequency range of the former system includes $2\omega_{cT}$ heating, current drive (TTMP) and $2\omega_{cD}$ heating. Physics analysis shows that the $2\omega_{cD}$ and $2\omega_{cT}$ heatings are suitable for burn control, because, even in the former case, wave power absorption by deuterons dominates the one by fusion alphas and it can bring the central ion heating in the ignition plasma parameters. Efficient burn control can be expected with centrally peaked ion heating. The central current drive is possible with slightly higher frequency from the tritium second harmonic resonance frequency. The current drive efficiency is 20-30 % smaller than the one of the lower frequency scenario ($\omega < \omega_{cT}$), but higher damping par pass can be expected. Strong coupling with deuterons will make local current profile control possible by accelerating deuterium beam ions with second or third harmonic ICRF waves in NBCD plasma. Enhancement of the current density by ICRF waves is localized near the cyclotron resonance layer. A current profile will be compensated by ICRF when penetration of the neutral beam changes. The system can also provide heating method of hydrogen plasma through helium 4 minority second harmonic heating, and D-He³ burn. From these respects, it can be concluded that the FER IC system is very attractive for the central ion heating and supplementary current drive system.

The launching system of the FER IC system and the ITER high frequency IC system is characterized by in-port plug and waveguide-fed loop antenna array. Merits are as follows.

- (1) Ceramic support is not necessary inside the cryostat.
- (2) There is no interference with the blankets.
- (3) Remote maintenance of the front end part of the launcher (Faraday shield and guard limiter) is relatively easy.

Overall structure of the launching system is consistent with radiation shielding, cooling, pumping, tritium safety and remote maintenance. The total system efficiency is expected to be nearly 60 %.

Power handling capability of the launcher is evaluated from the coupling calculation, assuming H mode scrape-off density profile ($n_e(\text{separatrix}) = 6.7 \times 10^{19} \text{ m}^{-3}$, e-folding length = 2.1 cm) and the maximum electric field strength in the ridged waveguide of 20 kV/cm. It is found that the coaxial mode dominates in the antenna radiation resistance for the 5×4 array. Hence, dependence of the coupling resistance on the antenna-plasma distance is quite small. The launcher can afford to have 20 MW injection power capability in the frequency range of 50 MHz ~ 85 MHz with the separatrix-antenna distance of 15 cm.

However, it should be checked carefully both in experiment and theory whether the coaxial mode works well or not.

Detailed analyses on important components such as the ridged waveguide, the Faraday shield and the guard limiter have been carried out. The shape of the ridge of the waveguide is optimized to provide desired frequency range with a finite element method. A gap distance between the ridge and the waveguide wall in the toroidal direction is set to be realistic value, i.e., 1.2 cm. The characteristic impedance is $28 \sim 16 \Omega$ in the frequency range of 50 ~ 85 MHz. From the thermal analysis of the Faraday shield, it is found that beryllium is suitable material for protection tiles of the Faraday shield. Due to the relatively large heat flux by α particles to the guard limiter, the front end part of the guard limiter (graphite or c-c composite) should be closely contacted with water cooling pipe of copper by brazing. Thick Faraday shield (43 mm in total thickness including beryllium tile) is necessary to tolerate disruption forces. In the conceptual design, it has been confirmed that all these components are possible with pertinent choice of design parameters and materials.

5.2 R&D Needs

5.2.1 R&D Programme

Specific R&D needed for the use of FWCD on ITER is minor; however some tasks have been identified that are necessary for the ITER FWCD system:⁹⁾

- (1) Radiation effects on ceramic insulators
- (2) Faraday shield materials and construction techniques should be tested to make sure that the Faraday shield will be able to meet the ITER reliability and life time requirements
- (3) Experience is needed in the design and operation of an antenna array suitable for FWCD.
- (4) Development work on the ridged waveguide will be needed to provide a back-up option to the coaxial conductor vacuum transmission line system.

For FER and Japanese contribution to ITER Long Term Technology R&D, an activity is focused on the development of a FWCD antenna system including development work on the ridged waveguide. The former could be installed and used for FWCD experiments on JT-60U.

5.2.2 Gain from JT-60/60U ICRF experiments and operations

Two main roles of ICRF heating in ITER/FER are central plasma heating and current drive, especially at high densities. As for plasma heating, high power ICRF experiments have been conducted in fundamental and second harmonic regimes on large tokamaks such as JET,²⁴⁾ JT-60²⁵⁾ and TFTR.²⁶⁾ Effectiveness of ICRF heating is well established while

further investigations are necessary for the current drive by ICRF waves. Sawtooth stabilization is observed accompanied with formation of an ion tail in ICRF heating experiments. Figure 5-1 shows a typical result of second harmonic minority heating in JT-60. When ICRF power, P_{IC} , of 2.2 MW is applied, the plasma store energy W^{DIA} and the central electron temperature T_{e0}^{ECE} significantly increase, indicating strong central electron heating with high heating efficiency.²⁷⁾ Calculations by a self-consistent wave code, which takes into account global wave structure and quasi-linear velocity distribution,²⁸⁾ suggest that these results are due to high energy ion generation in the plasma core. Moreover, the sawtooth period is extended up to 300 ms as long as the energy confinement time. Such sawtooth stabilization is observed even for high densities $\bar{n}_e \sim 7 \times 10^{19} \text{ m}^{-3}$ at relatively low power level $P_{IC} \geq 2 \text{ MW}$ on JT-60 while it is observed for $\bar{n}_e < 4 \times 10^{19} \text{ m}^{-3}$ on JET and TFTR. Although the reason for this difference may be due to the difference of the heating regime (second harmonic minority heating in JT-60, fundamental minority heating in JET and TFTR), a detail has not yet been understood. Therefore, objectives of ICRF heating in JT-60U will be focused on the investigation of the sawtooth stabilization of high density plasmas with much higher power than in JT-60 as well as the central heating of H-mode plasmas.

It can be recognized that JT-60U is very suitable tokamak device for FWCD experiment from the following reasons:

- (1) High electron temperature ($\sim 10 \text{ keV}$), which is highly demanded for FWCD experiment, can be expected with assistance of ECH (110 GHz, 5 MW).
- (2) High-frequency (110-131 MHz) and high-power (currently 6 MW, near future 10 MW) ICRF source is available.
- (3) Matching of FWCD and ECH frequencies is very good. Two FWCD regimes consistent with electron cyclotron central heating are possible.
 - (a) $\omega \sim 2.5\omega_{cH}$ ($5\omega_{cD}$) with $B_T = 3.3\text{--}3.5 \text{ T}$ (ECH; ω_{ce})
high confinement plasma
 - (b) $\omega \sim 4.5\omega_{cH}$ ($9\omega_{cD}$) with $B_T = 1.9 \text{ T}$ (ECH; $2\omega_{ce}$)
weaker ion damping
- (4) Two large horizontal ports (0.9 m in width and 0.78 m in height) are available for FWCD antennas.
- (5) Driven current at the 1-2 MA level at moderate electron density ($n_{e0} = 0.2 \times 10^{20} \text{ m}^{-3}$) is expected with 7 MW of total injection power, which is estimated assuming four current straps antenna, $N_{//} \approx 4$ and central electron temperature of 10 keV.

From a view point of the antenna engineering, the power injection capability and plasma-antenna coupling properties are matters of great interest. Features of JT-60 ICRF antenna were compact and high power density. The antenna was made up of 2×2 loops,

an open-type Faraday shield and a metallic casing. We could change the peak position of k_{\parallel} spectrum of the radiated power, $k_{\parallel}(\text{peak})$, by phasing loop element currents: $k_{\parallel}(\text{peak}) = 0 \text{ m}^{-1}$ for (0,0) phasing and $k_{\parallel}(\text{peak}) \sim 10 \text{ m}^{-1}$ for $(\pi, 0)$ phasing, where the former in parentheses is the toroidal phase difference of the loop currents and the latter the poloidal one. Figure 5-2 shows progress of the injected power P_{IC} as a function of the maximum voltage V_{max} in the coaxial line connected to the antenna in the JT-60 ICRF experiments.¹⁷⁾ The injection power of $\sim 3 \text{ MW}$ is achieved for both phasing modes. This corresponds to the injected power density of 16 MW/m^2 , the highest level among ICRF systems operating in the world. Although the effective heating is obtained for both phasing modes as described above, $(\pi, 0)$ phasing (high- k_{\parallel} mode) shows better heating efficiency than (0,0) phasing. Parametric decay instabilities, one of non-linear phenomena, are observed for (0,0) phasing but not for $(\pi, 0)$ phasing at such injected high power densities.²⁹⁾ On the other hand, the coupling resistance is $5 - 7 \Omega$ for (0,0) phasing and $1 - 3 \Omega$ for $(\pi, 0)$ phasing. These coupling properties are consistent with the predictions by the three-dimensional antenna-plasma coupling code including the effect of radial feeder currents.¹⁹⁾ Moreover, different behaviours of the coupling resistance between (0,0) and $(\pi, 0)$ phasing modes at H-mode transition are observed and analyzed by the code.³⁰⁾

On the basis of the good results on the JT-60 ICRF antenna, new antennas (two antennas) for JT-60U have been constructed.³¹⁾ The new antennas are also 2×2 loop array, essentially similar to the JT-60 antenna, but have three times larger size than that of the JT-60 antenna to improve power injection capability, especially for H-mode plasmas. The new antenna is equipped with poloidal septum and optimized to have $k_{\parallel}(\text{peak}) \sim 7.5 \text{ m}^{-1}$ with sharp peaks. An impedance matching system is composed of a high power phase shifter, one stub tuner ($\lambda/4$ choke type) and a frequency feed back control system to enhance a power handling capability and to easily make impedance matching for any antenna impedance with low reflectivity ($\sim 5 \%$). Effectiveness of the frequency feedback control system has already been confirmed in the JT-60 ICRF experiment. The output power of the ICRF heating system will be increased from 6 MW to 10 MW .

Thus, further data on power injection capability, limitation of stand-off voltage, coupling properties and antenna impedance matching will be obtained and effects of poloidal septum will be understood through the JT-60U ICRF experiments and operations.

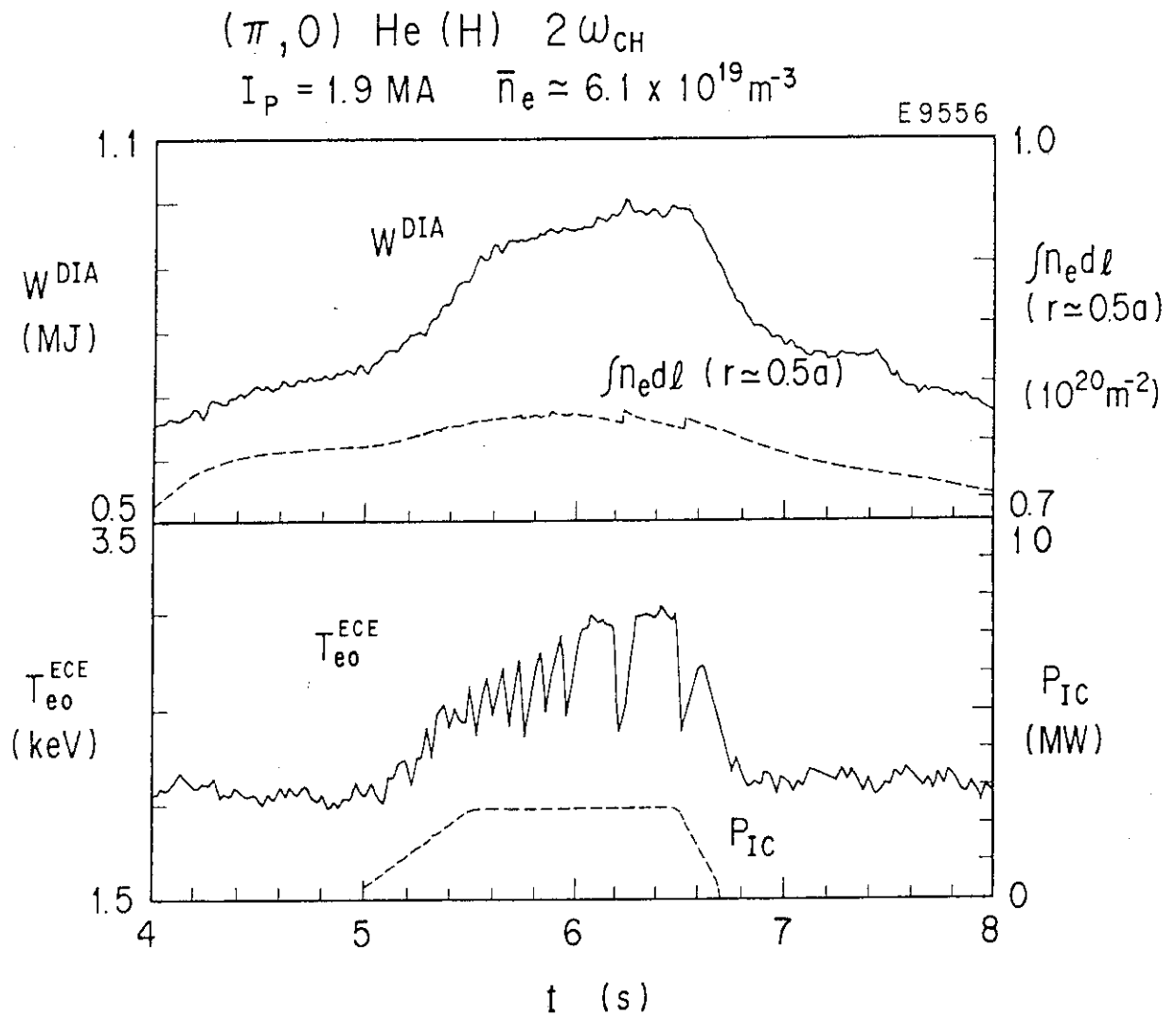


Fig. 5-1 Typical result of second harmonic minority ICRF heating in JT-60 at $\bar{n}_e = 6.1 \times 10^{19} \text{ m}^{-3}$.

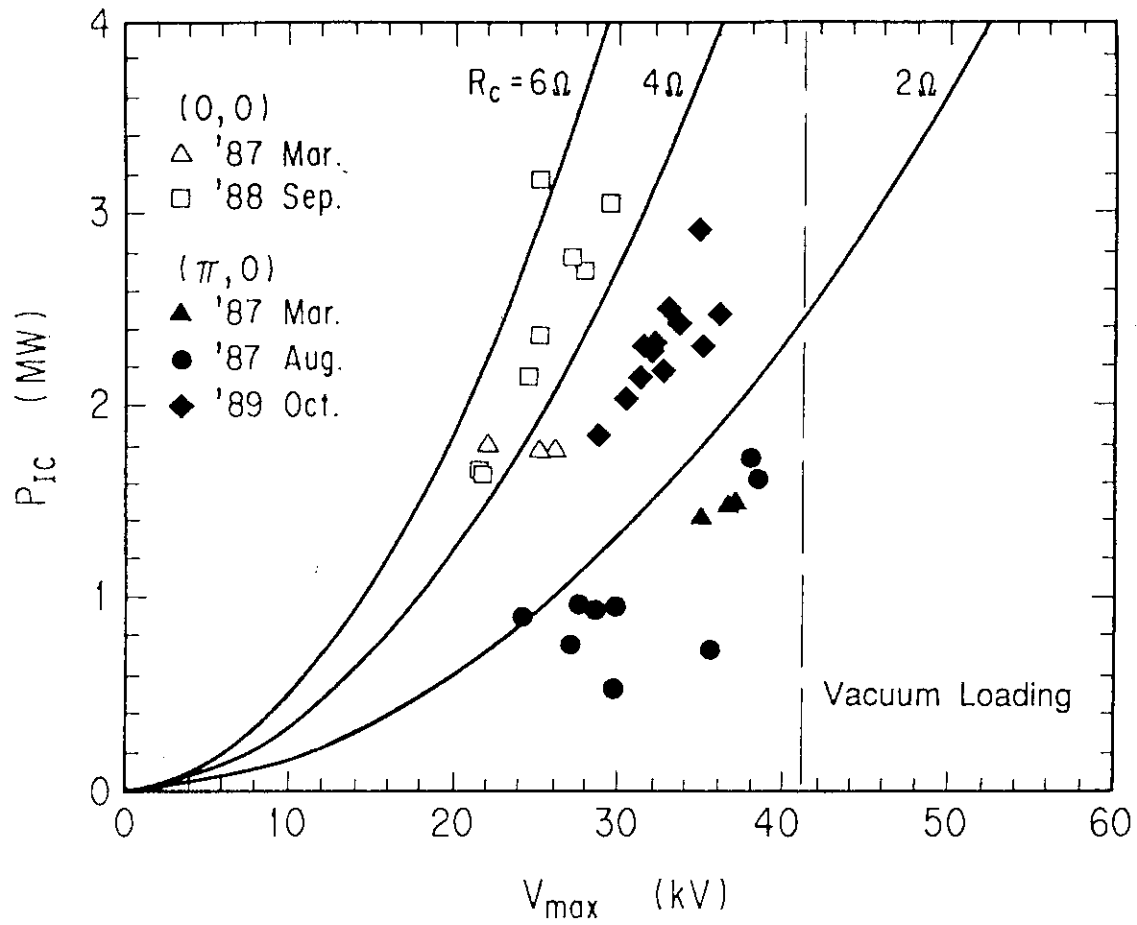


Fig. 5-2 Progress of the injected power P_{IC} as a function of the maximum voltage V_{max} in the coaxial line connected to the antenna in the JT-60 ICRF experiments.

ACKNOWLEDGEMENTS

We would like to thank all members of the FER Team and the ITER Team for useful discussions, comments and supports. We are much indebted to Drs. J. Jacquinot and D. Swain for fruitful discussions. Dr. Y. Kishimoto contributed valuable discussion on current drive calculation. Drs. K. Uehara and T. Yamamoto read and criticized the manuscript. We would also like to express our appreciation to Dr. T. Iijima, S. Tamura, Y. Tanaka, S. Shimamoto and M. Ohta for their encouragement and support.

REFERENCES

- 1) Matsuda S. et al. : Proc. 13th Int. Conf. on Plasma Physics and Controlled Nuclear Fusion Research, Washington (1990), IAEA-CN-53/G-2-2.
- 2) Tomabechi K. et al. : Proc. 13th Int. Conf. on Plasma Physics and Controlled Nuclear Fusion Research, Washington (1990), IAEA-CN-53/F-1-1.
- 3) Nevins W. et al. : Proc. 13th Int. Conf. on Plasma Physics and Controlled Nuclear Fusion Research, Washington (1990), IAEA-CN-53/F-3-4.
- 4) Zarnstorff M. et al. : Phys. Rev. Lett., 60 (1988) 1306.
- 5) Challis C. et al. : 14th Europ. Conf. on Contr. Fusion and Plasma Phys. (Madrid, 1987) Part III 1026.
- 6) Simonen T. et al., : Phys. Rev. Lett. 61 (1988) 1720.
- 7) JT-60 Team : 16 th Europ. Conf. on Contr. Fusion and Plasma Phys. (Venice, 1989).
- 8) Naito O. et al. : Nucl. Fusion 30 (1990) 1137.
- 9) Parail V. et al. : "ITER Current Drive and Heating System", ITER Documentation Series, No 32, IAEA (to be published).
- 10) Fukuyama A. et al. : "A Frequency Survey for Fast Wave Current Drive in ITER", ITER-IL-PH-6-9-J-6 (1989).
- 11) Ehst D.A. et al. : "Neoclassical Effects on RF Current Drive", ANL/FPP/TM-247 (1990).
- 12) Fukuyama A. et al. : Computer Physics Reports 4 (1986) 137-181.
- 13) Arai H. and Goto N. : IEEE Transaction on Plasma Science, vol. PS-13 (1985) 582-586.
- 14) Maki K. et al. : "Japanese Contributions to ITER Shielding Neutronics Design", JAERI-M 91-046 (1991).
- 15) Tani K. et al. : "Heat Load on the First Wall due to Ripple Loss of Alpha Particles", ITER Internal Letter ITER-IL-PH-1-9-J-2 (1989).

ACKNOWLEDGEMENTS

We would like to thank all members of the FER Team and the ITER Team for useful discussions, comments and supports. We are much indebted to Drs. J. Jacquinet and D. Swain for fruitful discussions. Dr. Y. Kishimoto contributed valuable discussion on current drive calculation. Drs. K. Uehara and T. Yamamoto read and criticized the manuscript. We would also like to express our appreciation to Dr. T. Iijima, S. Tamura, Y. Tanaka, S. Shimamoto and M. Ohta for their encouragement and support.

REFERENCES

- 1) Matsuda S. et al. : Proc. 13th Int. Conf. on Plasma Physics and Controlled Nuclear Fusion Research, Washington (1990), IAEA-CN-53/G-2-2.
- 2) Tomabechi K. et al. : Proc. 13th Int. Conf. on Plasma Physics and Controlled Nuclear Fusion Research, Washington (1990), IAEA-CN-53/F-1-1.
- 3) Nevins W. et al. : Proc. 13th Int. Conf. on Plasma Physics and Controlled Nuclear Fusion Research, Washington (1990), IAEA-CN-53/F-3-4.
- 4) Zarnstorff M. et al. : Phys. Rev. Lett., 60 (1988) 1306.
- 5) Challis C. et al. : 14th Europ. Conf. on Contr. Fusion and Plasma Phys. (Madrid, 1987) Part III 1026.
- 6) Simonen T. et al., : Phys. Rev. Lett. 61 (1988) 1720.
- 7) JT-60 Team : 16 th Europ. Conf. on Contr. Fusion and Plasma Phys. (Venice, 1989).
- 8) Naito O. et al. : Nucl. Fusion 30 (1990) 1137.
- 9) Parail V. et al. : "ITER Current Drive and Heating System", ITER Documentation Series, No 32, IAEA (to be published).
- 10) Fukuyama A. et al. : "A Frequency Survey for Fast Wave Current Drive in ITER", ITER-IL-PH-6-9-J-6 (1989).
- 11) Ehst D.A. et al. : "Neoclassical Effects on RF Current Drive", ANL/FPP/TM-247 (1990).
- 12) Fukuyama A. et al. : Computer Physics Reports 4 (1986) 137-181.
- 13) Arai H. and Goto N. : IEEE Transaction on Plasma Science, vol. PS-13 (1985) 582-586.
- 14) Maki K. et al. : "Japanese Contributions to ITER Shielding Neutronics Design", JAERI-M 91-046 (1991).
- 15) Tani K. et al. : "Heat Load on the First Wall due to Ripple Loss of Alpha Particles", ITER Internal Letter ITER-IL-PH-1-9-J-2 (1989).

- 16) Nakahara K. and Seki Y. : "Development of TPERM Code to Calculate Tritium Diffusion in Fusion Reactor Structures", JAERI-M 87-118 (1987) (in Japanese)
- 17) Fujii T., Saigusa M., Kimura H., et al.: to be submitted to Fusion Engrg. Des.
- 18) Kimura H., Fujii T., Ikeda Y., et al. : in Heating in Toroidal Plasmas (Proc. 4th Int. Symp. Rome, 1984), Vol. 2, International School of Plasma Physics, Varenna (1984) 1128.
- 19) Saigusa M., Kobayashi N., Kimura H., et al. : in Application of Radio-frequency Power to Plasmas (Proc. 7th Top. Conf. Kissimmee, 1987), American Institute of Physics, New York (1987) 282.
- 20) Cohn S. B. : "Properties of Ridge Waveguide," Proc. IRE, vol. 35, pp. 783-788, Aug. (1947).
- 21) Perkins F. W. : "ICRF Couplers," Bull. Amer. Phys. Soc., vol. 26, p. 929, Sept. (1981).
- 22) Yano Y., Goto N. and Nagashima T. : "An ICRF Ridged Wave-guide Coupler," IAEA Technical Committee Meeting on Radio Frequency Heating in Large Fusion Experiments, Princeton Univ PPL, 19-22, Oct. (1981).
- 23) Konrad A. : "Linear Accelerator Cavity Field Calculation by the Finite Element Method," IEEE Trans. Nucl. Sci., vol. NS-20, pp. 802-808, Feb. (1973).
- 24) JET Team (presented by Start D. F. H.) : Proc. 13th Int. Conf. on Plasma Physics and Controlled Nuclear Fusion Research, Washington (1990), IAEA-CN-53/E-2-2-1.
- 25) Imai T., Kimura H., Kusama Y., et al. : ibid. IAEA-CN-53/E-1-3.
- 26) Hosea J. C., Beer M., Bell M. G., et al. : ibid. IAEA-CN-53/E-1-5.
- 27) Fujii T., Kimura H., Saigusa M., et al. : Nucl. Fusion 31 (1991) 137.
- 28) Hamamatsu K., Azumi M., Kishimoto Y., et al., : Nucl. Fusion 29 (1989) 147.
- 29) Fujii T., Saigusa M., Kimura H., et al., : Fusion Engrg. Des. 12 (1991) 139.
- 30) Saigusa M., Kimura H., Fujii T., et al., : Nucl. Fusion (1989) 73.
- 31) Fujii T., Kobayashi N., Moriyama S., et al., : 16th Symp. on Fusion Technology, London, (1990).